Experimental Investigation of Light-Gauge Steel Plate Shear Walls for the Seismic Retrofit of Buildings

by

Jeffrey W. Berman and Michel Bruneau
University at Buffalo, State University of New York
Department of Civil, Structural and Environmental Engineering
Ketter Hall
Buffalo, NY 14260

Technical Report MCEER-03-0001

May 2, 2003

NOTICE

Experimental Investigation of Light-Gauge Steel Plate Shear Walls for the Seismic Retrofit of Buildings

by

Jeffrey W. Berman[1] and Michel Bruneau[2]

1   Graduate Research Assistant, Department of Civil, Structural and Environmental Engineering, University at Buffalo, State University of New York
2   Professor, Department of Civil, Structural and Environmental Engineering, University at Buffalo, State University of New York

Preface

The Multidisciplinary Center for Earthquake Engineering Research (MCEER) is a national center of excellence in advanced technology applications that is dedicated to the reduction of earthquake losses nationwide. Headquartered at the University at Buffalo, State University of New York, the Center was originally established by the National Science Foundation in 1986, as the National Center for Earthquake Engineering Research (NCEER).

Comprising a consortium of researchers from numerous disciplines and institutions throughout the United States, the Center's mission is to reduce earthquake losses through research and the application of advanced technologies that improve engineering, pre-earthquake planning and post-earthquake recovery strategies. Toward this end, the Center coordinates a nationwide program of multidisciplinary team research, education and outreach activities.

MCEER's research is conducted under the sponsorship of two major federal agencies: the National Science Foundation (NSF) and the Federal Highway Administration (FHWA), and the State of New York. Significant support is derived from the Federal Emergency Management Agency (FEMA), other state governments, academic institutions, foreign governments and private industry.

MCEER's NSF-sponsored research objectives are twofold: to increase resilience by developing seismic evaluation and rehabilitation strategies for the post-disaster facilities and systems (hospitals, electrical and water lifelines, and bridges and highways) that society expects to be operational following an earthquake; and to further enhance resilience by developing improved emergency management capabilities to ensure an effective response and recovery following the earthquake (see the figure below).
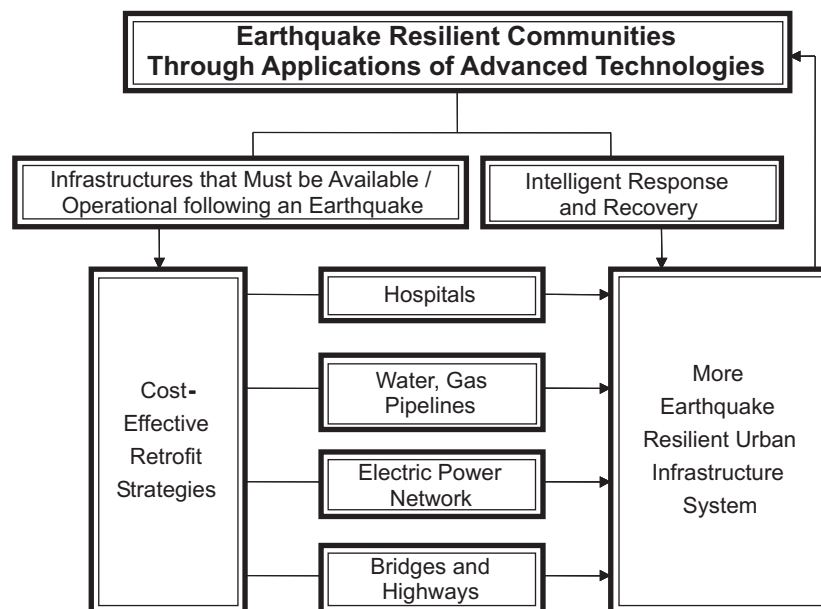
A cross-program activity focuses on the establishment of an effective experimental and analytical network to facilitate the exchange of information between researchers located in various institutions across the country. These are complemented by, and integrated with, other MCEER activities in education, outreach, technology transfer, and industry partnerships.

This research investigates the use of steel plate shear walls (SPSW) with light-gauge cold-rolled infill plates for seismic retrofit applications. These systems may overcome the limitations of similar systems with hot-rolled infill plates. The report describes the use of plastic analysis to develop a design procedure for SPSW in seismic applications based on the strip model, the design of prototype light-gauge steel plate shear wall concepts in the context of the seismic retrofit of hospitals, and the testing of these prototypes under quasi-static conditions. The hysteretic properties of the specimens and the demands from the infills on the existing framing are then assessed, and the results of testing are compared with predictions made using the strip model. The experimental results showed that the entire infill of the light-gauge SPSW participated in dissipated energy. The adequacy of the strip model in predicting the monotonic behavior of light-gauge SPSW into the nonlinear range was also found to be acceptable through comparison with the experimental results.

ABSTRACT

Steel plate shear walls (SPSW), which are allowed to buckle in shear and form a diagonal tension field, have been used as lateral load resisting systems for buildings. Research, both analytical and experimental, shows that these systems can be ductile, stiff, and have stable hysteretic energy dissipation when hot-rolled infill plates are used. However, the demands imparted on the surrounding framing in a seismic retrofit situation are substantial, and in most cases, the existing framing is likely insufficient. SPSW utilizing light-gauge cold-rolled infill plates could be a more viable option for retrofit scenarios. The work presented here experimentally investigates the seismic adequacy of such a system.

This report describes the prototype design, specimen design, experimental set-up, and experimental results of three light-gauge steel plate shear wall concepts. Additionally, a design procedure for SPSW based on the application of plastic analysis to an accepted analytical model for the representation of SPSW is proposed.

Prototype light-gauge steel plate shear walls are designed as seismic retrofits for a hospital structure in an area of high seismicity and emphasis is placed on minimizing their impact on the existing framing. Three single story test specimens are designed using these prototypes as a basis, two specimens with flat infill plates (thicknesses of 0.9 mm) and a third using a corrugated infill plate (thickness of 0.7 mm). Connection of the infill plates to the boundary frames is achieved through the use of bolts in combination with industrial strength epoxy or welds, allowing for mobility of the infills if desired. Testing of the systems is done under quasi-static conditions.

It is shown that one of the flat infill plate specimens, as well as the specimen utilizing a corrugated infill plate, achieve significant ductility and energy dissipation while minimizing the demands placed on the surrounding framing. It is also shown that the energy dissipation is evenly distributed across the entire infill. Experimental results are compared to monotonic pushover predictions from computer analysis using a simple model and good agreement is observed.

ACKNOWLEDGMENTS

TABLE OF CONTENTS

SECTION 5

EXPERIMENTAL PROGRAM AND OBSERVATIONS

SECTION 6

DISCUSSION AND COMPARISON OF RESULTS

LIST OF TABLES

LIST OF FIGURES

LIST OF FIGURES (CONTINUED)

LIST OF FIGURES (CONTINUED)

LIST OF FIGURES (CONTINUED)

LIST OF FIGURES (CONTINUED)

NOTATIONS

a	empirical factor in analytical boundary frame model
A	cross-sectional area of equivalent story brace
A_b	cross-sectional area of beam
A_c	cross-sectional area of column
A_g	gross cross-sectional area
A_{st}	cross-sectional area of strip
b	empirical factor in analytical boundary frame model
B	ratio of probable shear resistance to factored shear load
C_d	elastic displacement amplification factor
C_s	seismic coefficient
d	distance from current force to bound line
d_i	distance from upper left beam-to-column connection to zone 1 strips
d_{in}	distance from initial force of a cycle to bound line
d_j	distance from lower right beam-to-column connection to zone 2 strips
d_k	distance from lower right beam-to-column connection to zone 3 strips
Dmax	vector of maximum and minimum displacements
DRel	vector of relative displacements
F_y	yield stress
h	specimen height or hardening parameter in boundary frame model
h_i	elevation to story i
h_s	story height
h_{si}	height of story i
i	index for stories, cycles, or strips in zone 1
I	importance factor
I_c	column moment of inertia
j	index for stories or strips in zone 2
k	index for strips in zone 3
l	number of strips in zone 1
L	bay width

l_p	projected flat length of corrugation
l_w	wave length of corrugation
loc	vector containing the locations of Dmax within DRel
m	number of strips in zone 2
M_p	plastic moment capacity
M_{pb}	plastic moment capacity of beam
M_{pb1}	plastic moment capacity of first story beam
M_{pbi}	plastic moment capacity of ith story beam
M_{pbn}	plastic moment capacity of roof beam
M_{pc}	plastic moment capacity of column
M_{pc1}	plastic moment capacity of first story column
M_{pci}	plastic moment capacity of ith story column
M_{pcn}	plastic moment capacity of top story column
n	number of strips in zone 3
n_b	number strips attached to top beam
n_s	number of stories
R	seismic force modification factor
R_b	slope of bound line in boundary frame model
R_{bf}	force intercept of bound line in boundary frame model
R_{by}	vertical reaction force at point b
R_c	ratio of corrugation wave length to projected flat length
R_{ki}	initial stiffness of system for each cycle in boundary frame model
R_{kii}	initial stiffness of system in boundary frame model
R_{kp}	tangent plastic stiffness at any point in boundary frame model
R_{kt}	tangent stiffness at any point in boundary frame model
R_y	ratio of expected (mean) yield stress to the design yield stress
R_μ	ductility factor
s	strip spacing
S	section modulus
t	infill plate thickness

t_i	infill plate thickness at story I
V	base shear force
V_1	base shear force from zone 1 strips
V_2	base shear force from zone 2 strips
V_3	base shear force from zone 3 strips
V_{eu}	elastic base shear
V_i	applied lateral force at story i
V_j	applied lateral force at story j
V_{re}	probable shear resistance at the base of the wall
V_s	design base shear
V_y	yield base shear
V_u	ultimate base shear
w	strip width
α	angle of inclination of strips
β	angle used in equivalent story brace model
δ	relative displacement
δ_{max}	maximum relative displacement
δ_y	yield relative displacement
Δ	top story displacement
ΔF	incremental force in boundary frame model
Δ_i	total displacement of story i
Δ_{max}	maximum top story displacement
Δ_s	design top story displacement
Δ_y	yield top story displacement
θ	aspect ratio angle
λ	correction factor for equivalent story brace model
μ	displacement ductility ratio
μ_s	displacement ductility factor
Ω_D	design overstrength factor
Ω_M	material overstrength factor
Ω_o	total overstrength factor
Ω_S	system overstrength factor

ABBREVIATIONS

ACI	American Concrete Institute
AISC	American Institute of Steel Construction
ASTM	American Society for Testing and Materials
ATC	Applied Technology Council
CISC	Canadian Institute of Steel Construction
CSA	Canadian Standards Association
FEMA	Federal Emergency Management Agency
LRFD	Load and Resistance Factored Design
MCEER	Multidisciplinary Center for Earthquake Engineering Research
NBCC	National Building Code of Canada
SEESL	Structural Engineering and Earthquake Simulation Laboratory
SPSW	Steel Plate Shear Wall
UB	University at Buffalo
UTM	Universal Testing Machine

SECTION 1

INTRODUCTION

1.1 Statement of the Problem and Objectives

The seismic retrofit of existing buildings is a difficult task due to many factors, such as, the cost of closing the building for the duration of the retrofit work or having to heavily reinforce existing framing due to the increased demands the retrofit strategy may place on it. Light-gauge steel plate shear walls could provide engineers with an effective option for the seismic retrofit older buildings. The concept is to create a system that is strong enough to resist the necessary seismic forces and yet light enough to keep the existing structural elements from needing reinforcement. Additionally, if these systems could be installed quickly and eliminate the need to disrupt the occupants of existing structures, they would be even more desirable, especially in the context of a hospital retrofit.

Past research on steel plate shear walls has investigated the use of flat hot-rolled plates as infill panels. By allowing the infill plates to buckle in shear, develop diagonal tension field action, and then dissipate energy through the cyclic yielding of the infill in tension, researchers have shown that steel plate shear walls can be a useful seismic load resisting system. Such research has also produced useful analytical models for representing steel plate shear walls allowed to develop tension field action, and some of these have been implemented in steel design standards. However, use of steel plate shear walls with hot-rolled infill plates (5 mm minimum thickness) in a retrofit situation, in which it would be used to infill an existing bay, would likely require reinforcement of the existing beams and columns due to the large moments induced from the plate yielding, which can add significant cost.

Therefore, it would be advantageous to develop light-gauge steel plate shear wall systems that can be applied to the seismic retrofit of existing structures and limit the demands induced to the existing framing. Furthermore, an interest exists in creating systems that are easily installed, with minimum disruption to the function of an existing building, and in the context of the seismic retrofit of hospital structures, there is interest in making these systems modular to allow for the rearrangement of floor plans (that hospitals often undergo).

The research described in this report includes the design and quasi-static testing of three such light-gauge steel plate shear wall systems. Additionally, the application of plastic analysis to general steel plate shear wall design is a subject that has not yet been explored. Therefore, this study will also consider how plastic analysis can be applied to the design of steel plate shear walls. This research only focuses on walls allowed to buckle in shear and develop tension field action.

1.2   Scope of Work

Research conducted as part of this project can be divided into five steps:

- Use plastic analysis to develop a design procedure for steel plate shear walls in seismic applications based on the strip model, which was developed by others and implemented in some design standards for the representation of such walls.
- Design prototype light-gauge steel plate shear wall concepts in the context of the seismic retrofit of hospitals. Three concepts are considered as part of this project.
- Based on the prototypes, design and experimentally test under quasi-static conditions, light-gauge steel plate shear wall specimens.
- Assess the hysteretic properties of those specimens and the demands from the infills on the existing framing.
- Compare the results of testing with predictions made using the strip model.

1.3   Report Organization

Section 2 contains a brief review of past research on the post-buckling strength of steel plate shear walls, as well as a description of the current design procedure in CAN/CSA S16-01 (CSA, 2001).

Section 3 focuses on the plastic analysis of steel plate shear walls and the development of a new design procedure based on those results. It also identifies an aspect of the CAN/CSA S16-01 procedure that could lead to unconservative designs and proposes a modification to that procedure to avoid them.

Section 4 describes the design of the prototype light-gauge steel plate shear walls in the context of the retrofit of an existing hospital structure. Following this, the design of three specimens for laboratory testing is described. Details on the design of the test setup are given along with relevant material descriptions and results of sample coupon testing of the infill materials for the three specimens. Finally, the instrumentation layout is described.

Section 5 begins with a discussion of the loading protocol used for the quasi-static testing. Then complete descriptions of observations made during the testing of each specimen are given, accompanied by several photos taken during the testing.

Section 6 discusses the results of the testing in a quantitative manner and explores several key issues pertaining to behavior, including the contribution of the surrounding framing to energy the energy dissipation of the specimens, the variation of strain across the infills, the initial stiffnesses of the specimens, the ductility, and the accuracy of the strip model in predicting the monotonic behavior of the specimens.

Conclusions based on the information presented in the previous chapters are made in Section 7 and recommendations for further research are given.

SECTION 2

LITERATURE REVIEW

2.1   General

There have been significant advances in knowledge pertaining to the behavior of unstiffened steel plate shear walls in the past twenty years. In this section, some of the major research efforts that have led to this advancement in knowledge are reviewed. Emphasis will be placed on experimental investigations, while some analytical work is also reviewed. Points of primary interest are hysteretic behavior, yield capacities and displacements, ultimate capacities and displacements, boundary frame connections used, effects on the columns of boundary frames, and ultimate failure modes observed. Additionally, the requirements for the design of steel plate shear walls as they appear in the Canadian standard on Limit States Design of Steel Structures, CAN/CSA-S16-01 (CSA, 2001), are also reviewed.

2.2   Thorburn, Kulak, and Montgomery (1983)

Thorburn *et al.* (1983) investigated the postbuckling strength of steel plate shear walls.   Building from the original work on plate girder webs subjected to shear by Basler (1961) and the theory of diagonal tension field action by Wagner (1931), they were able to develop concepts for designing steel plate shear walls allowed to buckle in shear and form a diagonal tension field to resist the applied lateral loads.

Thorburn *et al.* (1983) developed two analytical models to represent unstiffened thin steel plate shear walls that resist lateral loads by the formation of a tension field. In both cases any contribution from the compressive stresses in the plate were neglected because it was assumed

5
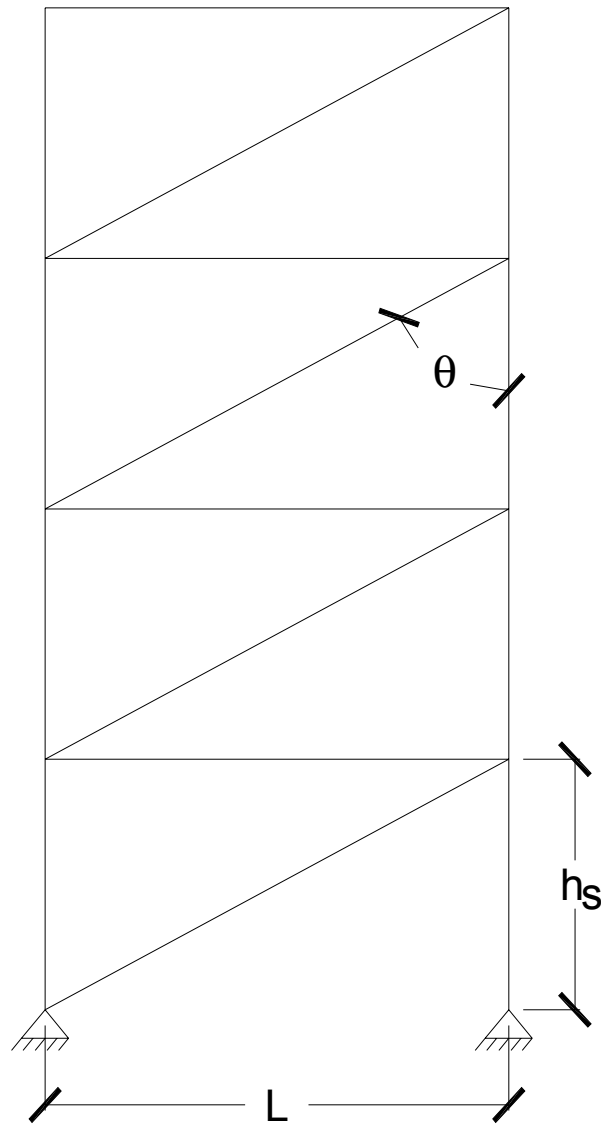
FIGURE 2-1 Equivalent Story Brace Model (Adapted from Thorburn and Kulak, 1983)

that the plate buckles at a low load and displacement level. Additionally, it was assumed that the columns were continuous over the full height of the wall and that the beams were pin-ended.

The first model, an equivalent story brace model, represents the infill plate as a single diagonal tension brace on each story (figure 2-1). Using an elastic strain energy formulation the researchers showed that for infinitely stiff boundary members the plate thickness can be found from the area of the equivalent story brace as:

$$t = \frac{2A \sin\theta \sin 2\theta}{L \sin^2 2\alpha} \tag{2-1}$$

and for flexible columns ($I_c = 0$, where I_c is the column moment of inertia):

$$t = \frac{2A \sin 4\beta}{L \tan\beta} \tag{2-2}$$

where A is the area of the of the diagonal brace, L is the bay width, $\theta = \tan^{-1}(L/h_s)$, h_s is the story height, $2\beta = \tan^{-1}(L/h_s)$, and α is the angle of inclination of the tension field. This inclination angle was found to be equal to β for the case of flexible columns, and for infinitely rigid columns it was found to be:

$$\tan^4 \alpha = \frac{1 + \dfrac{Lt}{2A_c}}{1 + \dfrac{h_s t}{A_b}} \tag{2-3}$$

where A_b and A_c are the story beam and column cross-sectional areas respectively.

The story beams were assumed to be rigid in all cases because of the opposing tension fields acting simultaneously on both sides of the beams. This balanced loading from opposing tension field action does not exist on the roof beam and bottom floor beam, and these would need to be modeled with their actual stiffnesses. The two cases were treated as bounds on the actual behavior and a plate thickness somewhere in between the results from these two cases was found to be desirable. It was recommended that the equivalent story brace model be used to determine the preliminary sizes of both the boundary members and the infill plates because of the model's simplicity.

The second model developed by Thorburn *et al.* (1983) is known as the strip model (or multi-strip model) and is shown in figure 2-2. In this model the plate is represented as a series of inclined, pin-ended, tension members that have a cross-sectional area equal to the strip spacing times the plate thickness. The angle of inclination of the strips is α, as described above, and the two cases of rigid columns and completely flexible columns are again treated separately and were assumed to provide bounds on the actual behavior.
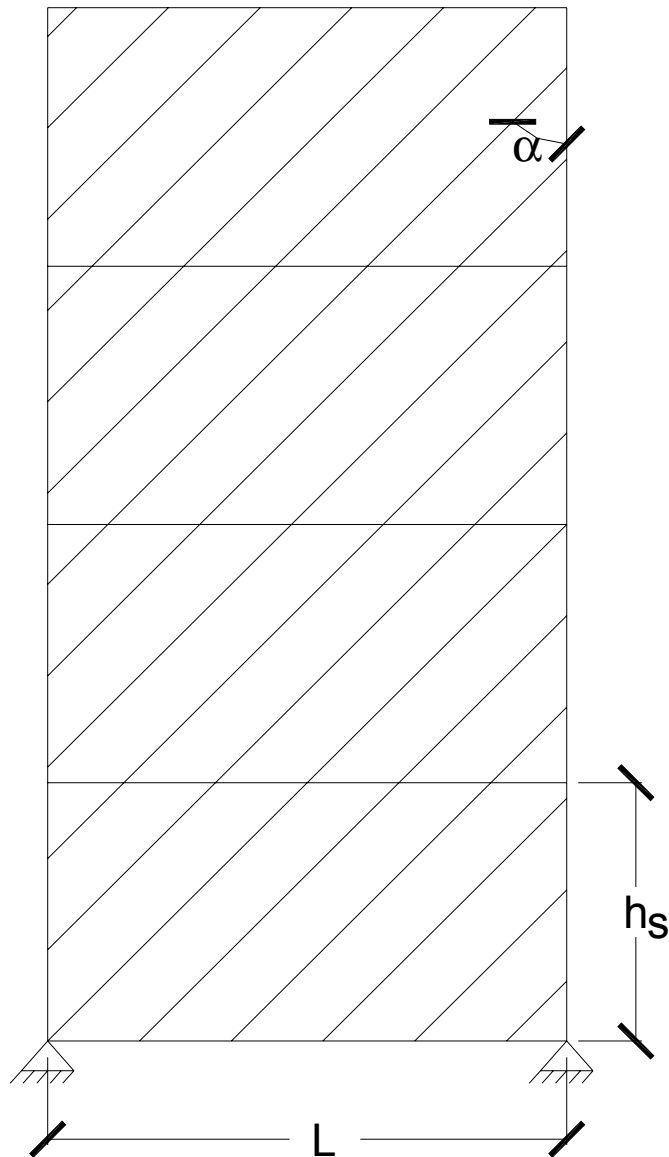
FIGURE 2-2 Strip Model (Adapted From Thorburn and Kulak, 1983)

2.3 Timler and Kulak (1983)

Timler and Kulak (1983) tested a single story, large scale, thin steel plate shear wall to verify the analytical work of Thorburn *et al.* (1983). The test specimen consisted of two panels connected such that opposing tension fields would occur as shown in figure 2-3 (i.e. two single story walls were tested at the same time). Infill plates were 5 mm thick and the bay dimensions were 3750 mm wide by 2500 mm high. Columns were W310x129 (W12x87), beams were W460x144 (W18x97) and simple beam-to-column connections were employed. The loading consisted of

three quasi-static cycles at the maximum permissible serviceability drift limit ($h_s/400$) prescribed by CSA-S16.1-M78 (CSA, 1978), followed by a final monotonic push to failure. No axial load was applied to the columns to represent gravity loading.
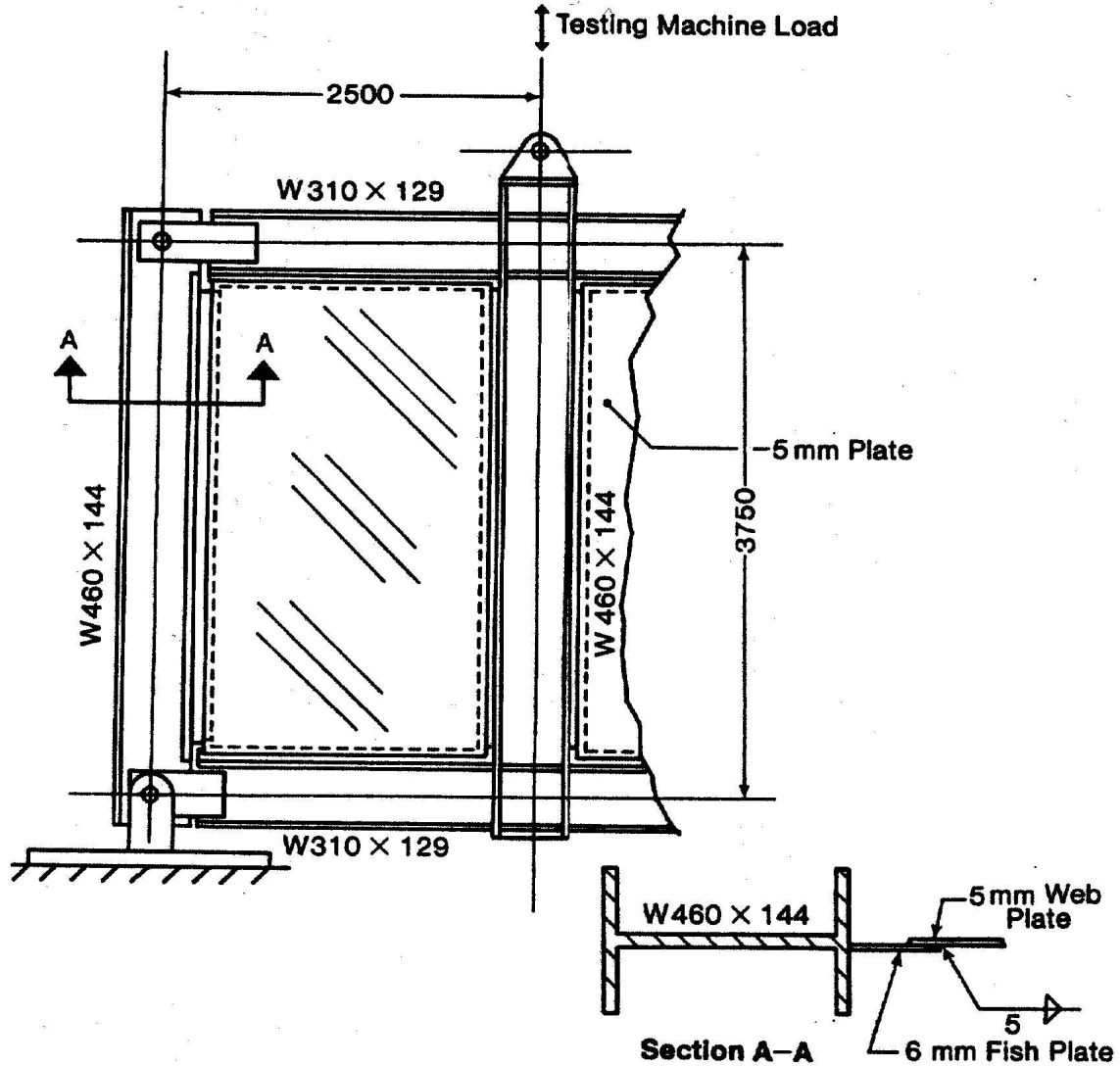
FIGURE 2-3 Schematic of Test Specimen (Timler and Kulak, 1983)

At the serviceability limit, the angle of inclination of the tension field along the centerline of the panel was found to vary from 44° to 56°. The maximum load attained was 5395 kN (1213 kips). Failure of the specimen resulted from tearing of the weld used to connect the infill plate to the fish plate and it was concluded that had this been avoided the specimen could have taken an even larger ultimate load.

9

The strip model was used to analyze the test specimen and good results were reported in regards to the model's prediction of the member and panel strains, as well as, the load-deformation curves for the experiment. In the strip model, an elastic perfectly plastic stress-strain curve was used to represent the plate material which was found from coupon tests to have a curve similar to that of cold-worked steel. The researchers concluded that the strip model would have underestimated the elastic stiffness of the experiment if hot-rolled plates had been used in the experiment.

Timler and Kulak (1983) also revised (2-3) to include the effects of column flexibility, and proposed the following equation:

$$\tan^4 \alpha = \frac{1 + \dfrac{Lt}{2A_c}}{1 + \dfrac{h_s t}{A_b} + \dfrac{h_s^4 t}{360 I_c L}} \tag{2-4}$$

where I_c is the moment of inertia of the bounding column. (2-4) and (2-1) appear in the mandatory Clause 20 of CAN/CSA-S16-01; in the previous edition of the standard, they were in Appendix M. (2-1) is recommended for preliminary proportioning of beams, columns, and infill plates while (2-4) is used for development of the detailed multi-strip model. Note that the treatment of the two cases involving rigid and flexible columns is not required by the standard which instead recommends that columns be modeled with their actual properties.

2.4   Tromposch and Kulak (1987)

Tromposch and Kulak (1987) tested a large scale steel plate shear wall (figure 2-4) similar to that tested by Timler and Kulak (1983). The major differences between the two was a change in the bay dimensions to 2750 mm in width by 2200 mm in story height, the use of bolted rather than welded beam-to-column connections, thinner plates (3 mm) made of hot-rolled steel, stiffer beams (W610x241(W24x62)), prestressing of columns to simulate the effect of gravity load, and a more comprehensive cyclic and monotonic loading regimen. Stiffer beams were used in order to simulate the effect of a tension field above and below the panel being tested so that the results could be applied to multistory steel plate shear walls.
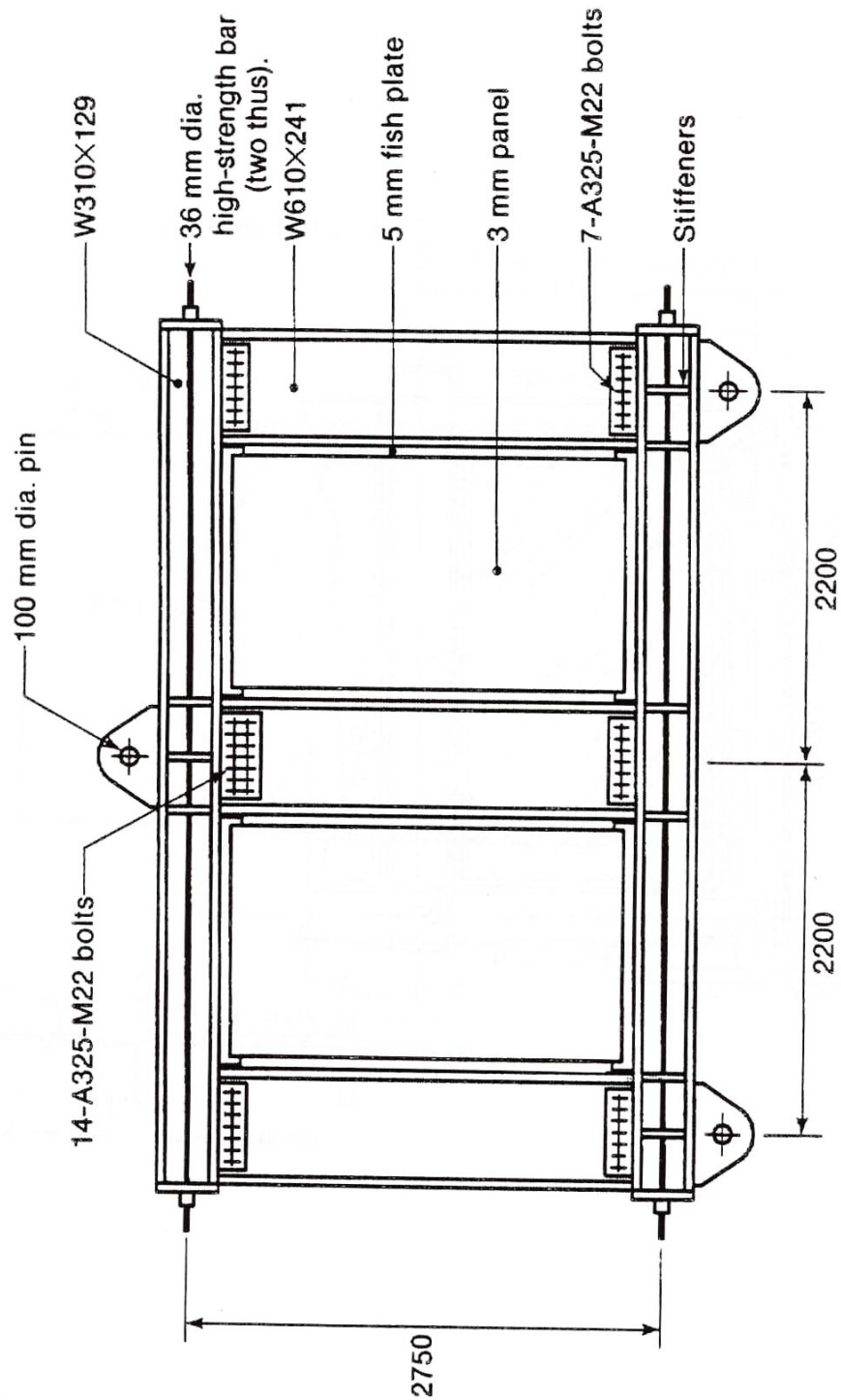
FIGURE 2-4 Schematic of Test Specimen (Tromposch and Kulak, 1987)

Twenty-eight fully reversed quasi-static cycles were applied up to a load level of 67% of the
ultimate capacity. The maximum displacement reached during this loading stage was 17 mm or

h_s/129 (0.8% drift). After that sequence, the prestressing rods were removed from the columns and loading was continued monotonically to failure. The final displacement reached was 71 mm or h_s/31 (3.2% drift). Failure of the specimen was attributed to bolt slippage at the beam column connections and tearing of the welds attaching the infill plate to the fish plate. However, ultimate failure did not occur; testing stopped because the actuator reached its maximum capacity while the test specimen could have taken more load. Hysteretic loops obtained from the experiment were pinched but stable and showed stable energy dissipation.

The multi-strip model was used to predict the test results and was found to be adequate in predicting the ultimate capacity of the wall, and in predicting the envelope of cyclic response. In order to achieve this result it was necessary to treat the frame connections as rigid at low load levels and pinned after bolt slippage had occurred. It was also found that including an estimate of the residual welding stress in the infill plate helped obtain more accurate results from the multi-strip model.

Tromposch and Kulak (1987) also revised a model for predicting the hysteretic behavior of steel plate shear walls originally proposed by Mimura and Akiyama (1977). Their modifications included neglecting the prebuckled stiffness of the infill plate and treating the stiffness of the entire assembly as the stiffness of only the boundary frame until a displacement large enough to form the tension field in the infill is applied. This implies that this analytical model of the assembly could have zero stiffness if the displacement is large enough to form a mechanism in the frame but not large enough to engage the tension field, a possible scenario in large displacement cyclic loading.

2.5   Caccese, Elgaaly, and Chen (1993)

An experimental investigation into the effects of panel slenderness ratio and type of beam-to-column connection was performed by Caccese *et al.* (1993). They tested five 1/4 scale models of three story steel plate shear walls with varying plate thicknesses and beam-to-column connection type (see figure 2-5). Plate thicknesses used were 0.76 mm, 1.9 mm and 2.66 mm with moment-resisting connections and 0.76 mm and 1.9 mm with simple shear beam-to-column connections. The wall height was 2870 mm with 838 mm stories and a 229 mm deep stiff structural member

at the top of the third story to anchor the tension field. Bays were 1245 mm wide and infill panels were continuously welded to the boundary frame.

Loading was applied at the top of the third story only. Columns were not preloaded axially and the effects of gravity load were not considered. The loading program consisted of three cycles at each of eight displacement levels incremented by 6.35 mm. The maximum displacement reached was 50.8 mm or 2% drift. After these 24 cycles were complete, the same cyclic displacement program was re-applied. If the specimen was still intact at this point, it was pushed monotonically to the displacement limit of the actuator.

This test series revealed a transition in failure modes depending on the plate thickness used. When slender plates were used, the plates yielded before any boundary members and failure of the system was governed by the formation of plastic hinges in the columns. As the plate thickness increased, the failure mode was governed by column instability. Once instability governed, further increases in the plate thicknesses were found to have only a negligible effect on the capacity of the system. Caccese *et al.* concluded that the use of slender plates will therefore result in more stable systems because they will not be governed by column buckling prior to the plate reaching a fully yielded state. Kennedy *et al.* (1994), commenting on those results, argued that the columns in a steel plate shear wall system can be designed to support the load induced by the infill panel, and that buckling prior to plate yielding can therefore be avoided.

Caccese *et al.* also reported that the difference between using simple and moment-resisting beam-to-column connections was small. This was attributed to the fact that the infill plate was fully welded all around to the frame, which in essence creates a moment-resisting connection. This point was later addressed by Kulak *et al.* (1994) who argued that the differences in the material properties, plate thicknesses, and the failure of a weld in one of the specimen prevented a direct comparison in the context of connection type. They also pointed out that Tromposch and Kulak (1987) showed analytically that greater energy dissipation could be achieved with the use of moment connections.
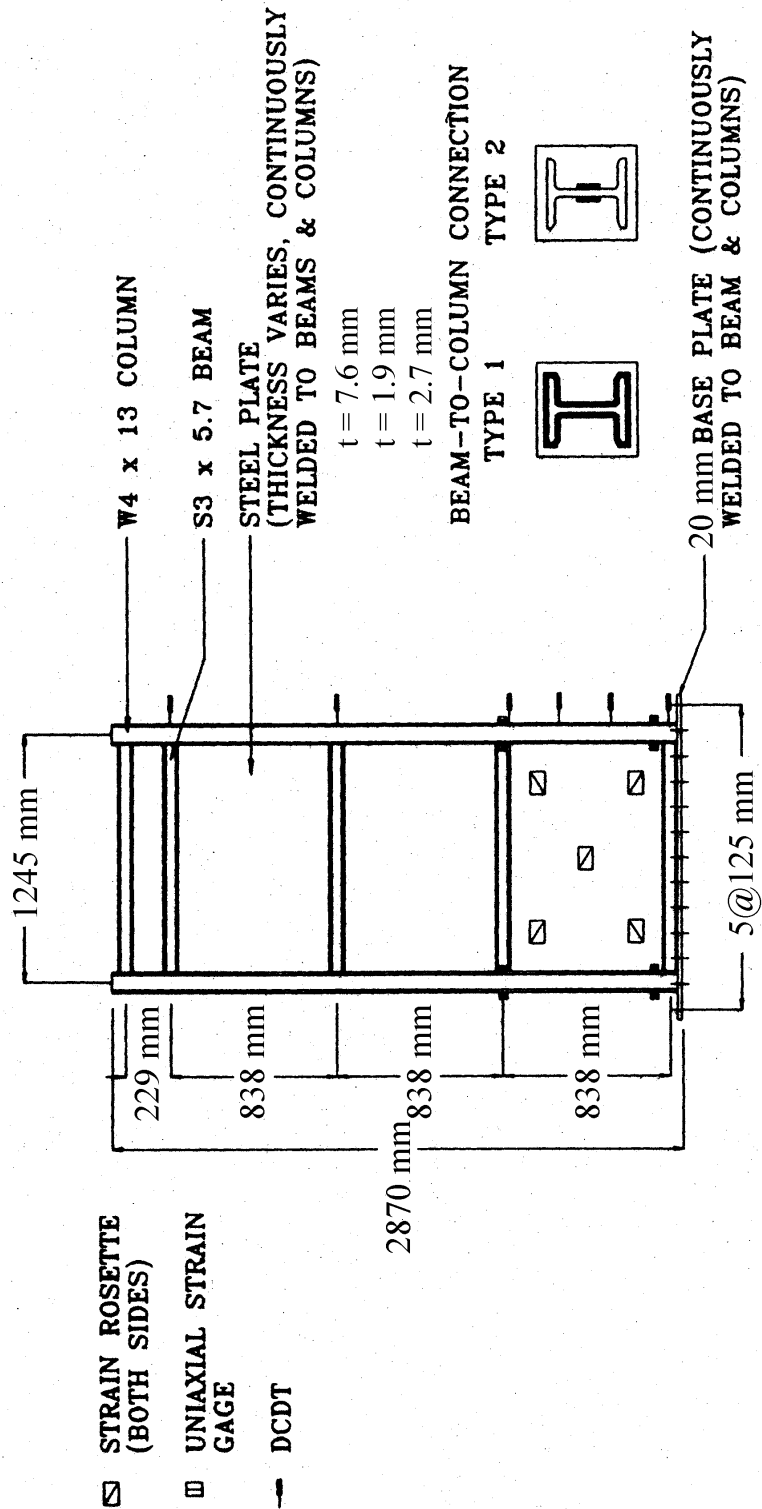
FIGURE 2-5 Schematic of Test Specimen (Adapted from Caccese *et al*., 1993)

14

2.6   Elgaaly, Caccese, and Du (1993)

Elgaaly *et al.*(1993) used finite element models, and models based on the revised multi-strip method proposed by Timler and Kulak (1983), to replicate results experimentally achieved by Caccese *et al.* (1993).

The finite element model used nonlinear material properties and geometry, a 6x6 mesh to represent the plates on each story, and six beam elements for each frame member. The 1.9 mm and 2.7 mm plate thicknesses used in the experimental work were considered in the finite element models. Moment-resisting beam-to-column connections were assumed. Lateral load was monotonically applied to failure. For both thicknesses, the failure load was defined by the loss of stability due to column yielding. It was found that the wall with thicker plates was not significantly stronger than the other one because column yielding was the governing factor for both cases. The finite element models significantly over-predicted both capacity and stiffness compared to the experimental results. These discrepancies were attributed to difficulty in modeling initial imperfections in the plates and the inability to model out of plane deformations of the frame members.

The specimen using moment-resisting beam-to-column connections and the 1.9 mm thick plate was also modeled using the multi-strip method. Twelve strips were used to represent the plate at each story. The angle of inclination of the strips was found to be 42.8° which agreed well with the results of the finite element model that predicted the principle strains in the middle of the plates to be oriented between 40° and 50° with the vertical. Using an elastic perfectly plastic stress-strain curve for the strips, the model was found to produce results in reasonable agreement with the experimental results with respect to initial stiffness, ultimate capacity, and displacement at the ultimate capacity. Using an empirically obtained trilinear stress-strain relationship for the strips, even better agreement with the experimental results was obtained. This model also proved to provide equally good results for the specimen having 0.76 mm and 2.66 mm plate thicknesses.

An analytical model for predicting the hysteretic cyclic behavior of thin steel plate shear walls was also developed. This model was based on the strip model, but incorporated strips in both directions (see figure 2-6) which is necessary to capture cyclic behavior. The hysteretic model

involved the use of an empirically derived, hysteretic, stress-strain relationship for the strips and good agreement with experimental results was reported.
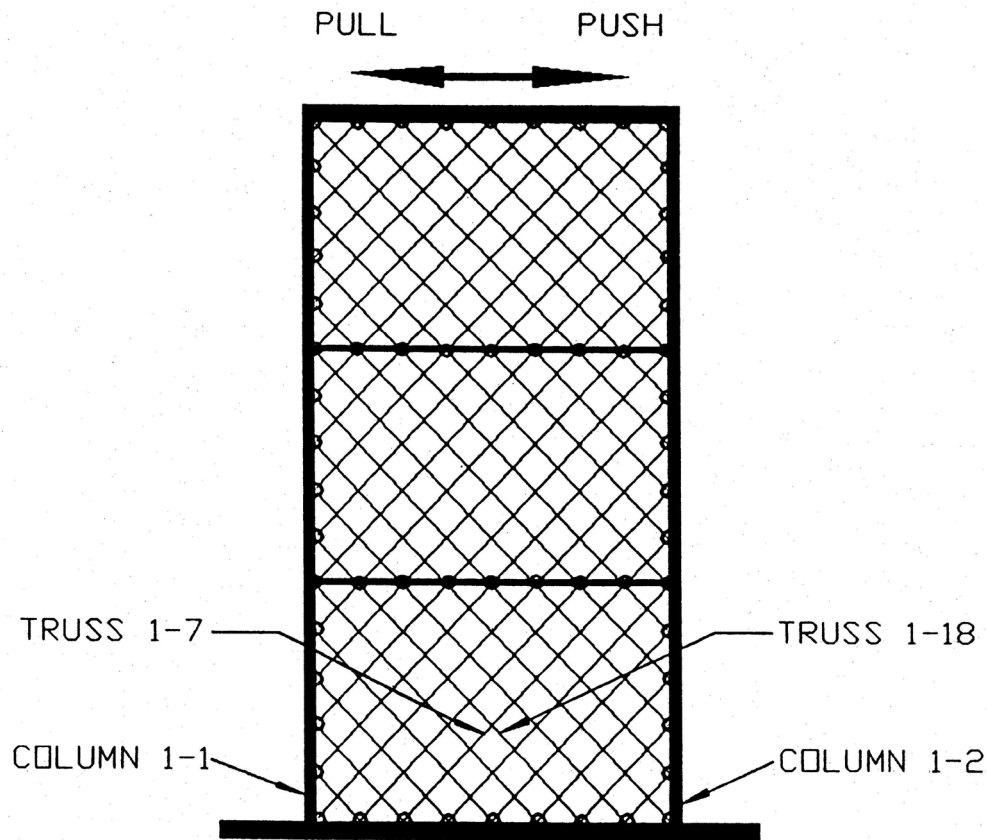
FIGURE 2-6 Cyclic Strip Model (Elgaaly *et al.*, 1993)

2.7 Xue and Lu (1994)

Xue and Lu (1994) performed an analytical study on a three bay twelve story moment-resisting frame structure which had the middle bay infilled with a steel plate shear wall. The effect beam-to-column and plate connections was the focus of this study. Four scenarios were considered: (a) moment-resisting beam-to-column connections and infill plates fully connected to the surrounding frame; (b) moment-resisting beam-to-column connections and the infill plates attached to only the beams; (c) shear beam-to-column connections and fully connected infill plates, and; (d) shear beam-to-column connections with infill plates connected only to the beams. Plate thicknesses were the same for each configuration but varied along the height. Stories 1-4, 5-8, and 9-12 respectively had 2.8 mm, 2.4 mm, and 2.2 mm thick plates. The exterior bays were 9144 mm wide, the interior (infilled) bay was 3658 mm wide, high and all stories were 3658 mm tall except the first story which was 4572 mm tall.

The finite element analysis considered beams and columns modeled using elastic beam elements and plates modeled using elasto-plastic shell elements. Initial imperfections in the infill plates were modeled using the buckling modes of the plates. Each model was subjected to push-over analysis with forces applied at each story.

It was found that the type of beam-to-column connection in the infilled bay had an insignificant effect on the *global* force-displacement behavior of the system and that connecting the infill panels to the columns provided only a modest increase in the ultimate capacity of the system. However, Xue and Lu (1994) concluded that connecting the infill plates to only the beams and using simple beam-to-column connections in the interior bay was the optimal configuration because this drastically reduced the *local* shear forces in the interior columns. This was viewed as a desirable condition which would help avoid premature column failure.

2.8 Driver, Kulak, Kennedy, and Elwi (1997)

Driver *et al.* (1997) tested a large scale multi-story steel plate shear wall to better identify the elastic stiffness of the structure, the first yield of the structure, ductility and energy absorption capacity, cyclic stability, and failure mode of the wall. Additionally, the test specimen was constructed with moment-resisting beam-to-column connections and a better understanding of the interaction between the plates and moment frame was sought.

The specimen (figure 2-7) was four stories tall, with a first story height of 1927 mm, a height of 1829 mm for the other stories, and a bay width of 3050 mm. The plate thicknesses were 4.8 mm and 3.4 mm for the first two and last two stories respectively. A relatively large and stiff beam was used at the roof level to anchor the tension field forces that would develop. A fish plate connection was used to connect the infill plates to the frame, as shown in figure 2-8. Ancillary tests involved an examination of several possible corner details (Schumacher, *et al.* 1999) which resulted in identification of a suitable detail. Residual stress and coupon tests were also performed. The coupon testing showed that the mean yield stress was 341.2 MPa for the 4.8 mm plates, 257.2 MPa and 261.5 MPa for the third and forth floor plates respectively.
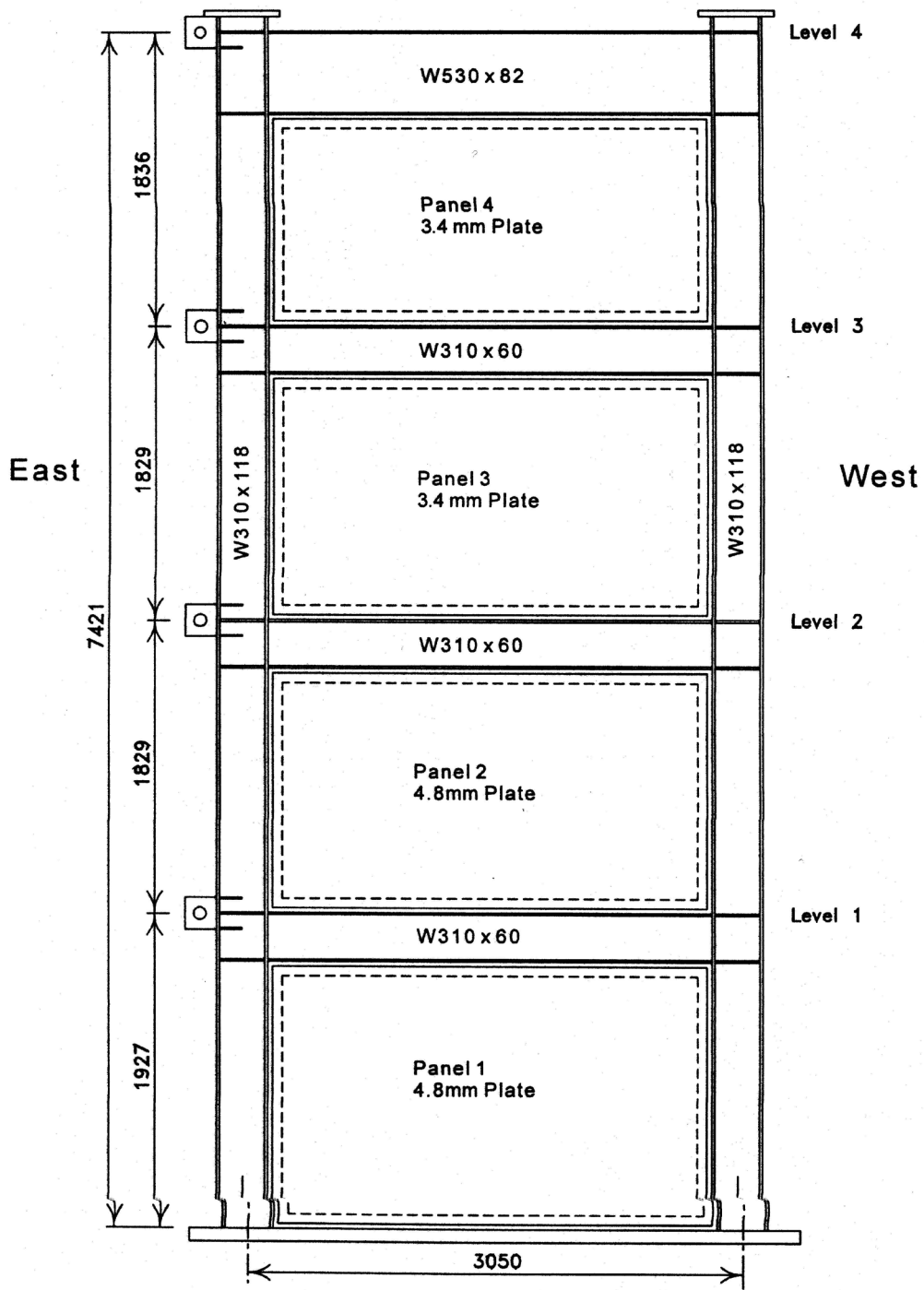
FIGURE 2-7 Schematic of Test Specimen (Driver *et al*. 1997)
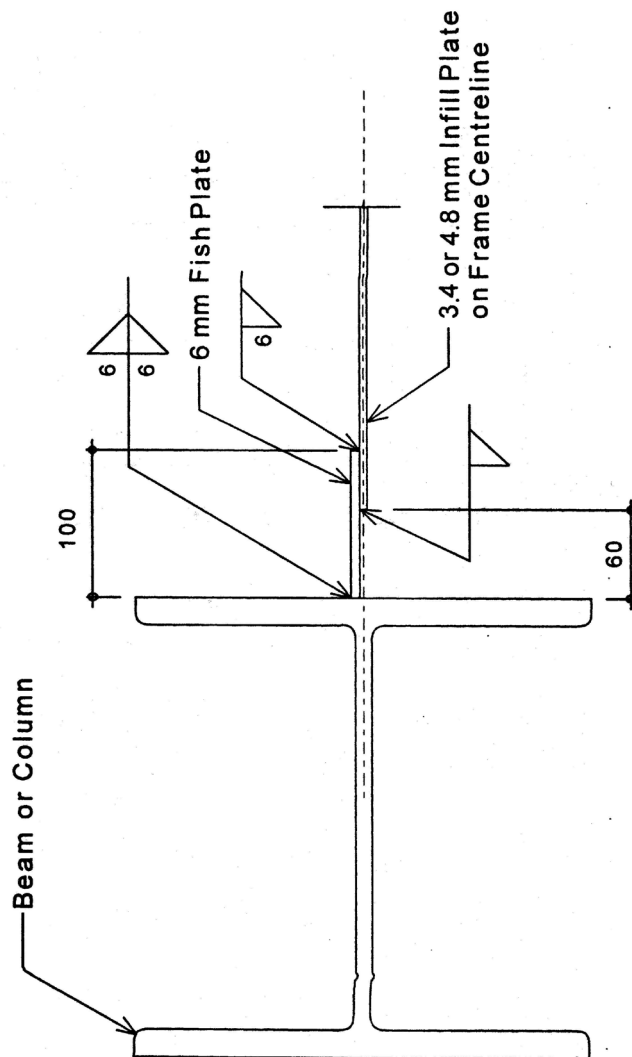
FIGURE 2-8 Fish Plate Connection Detail (Driver *et*
al. **1997)**

Cyclic quasi-static loading was applied for 35 cycles of increasing lateral displacement.
Actuators were mounted at each story to provide a distributed force over the height of the
structure. Gravity loading was also applied. The yield displacement and corresponding base
shear of the specimen were respectively found to be 8.5 mm and 2400 kN based on observation
of the experimental load versus deformation curve. At three times the yield displacement,
tearing of a first story plate weld occurred and yielding of the beam-column panel zone at the top
of the first story was observed. At this point the base shear was 3000 kN. Local buckling of the
column flange below the first story was observed at four times the yield displacement. Several
tears in the first story plate and severe local buckling of the same column was observed at six

19

times the yield displacement. At this point the structure was still holding 95% of the ultimate strength reached. Failure occurred at nine times the yield displacement when the full penetration weld at the base of a column fractured. Even at this point the structure was holding 85% of the ultimate strength reached. Observation of the specimen following the test revealed minimal whitewash flaking in the beam-column connections, leading the researchers to conclude that most of the energy dissipation was done through the yielding of the plates. Additionally, it was found by investigating the hysteresis loops for each story, that the first story plate absorbed the majority of the damage. It was concluded that the steel plate shear wall tested, with moment-resisting connections, exhibited excellent ductility and stable behavior.

The specimen was then modeled analytically considering both finite element and strip model approaches. The finite element simulation predicted the ultimate strength and initial stiffness well for all stories. However, at displacements larger than the yield displacement the simulation overestimated the stiffness of the steel plate shear wall. It was concluded that this discrepancy was do to the inability to include second order geometric effects. The strip model also gave good overall agreement with experimental results, with the exception of underestimating the initial stiffness. At loads of 55% to 65% of the ultimate strength and above, the stiffness of the strip model became equal to that of the experiment.

Also included in this investigation was a revision of the hysteretic model proposed by Tromposch and Kulak (1987). The model was revised by explicitly separating the contributions from the moment-resisting frame and infill panel. The two components were assigned empirically derived bilinear hysteretic behavior, which when combined, resulted in a trilinear behavior of the system and good agreement with experimental results.

2.9   Rezai (1999)

Dynamic shake table testing of a thin steel plate shear wall was performed by Rezai (1999). This study focused on the evaluation of Appendix M (specifications for steel plate shear walls) of what was then the latest version of Canada's national standard on Limit States Design of Steel Structures, CAN/CSA-S16.1-94 (CSA, 1994).
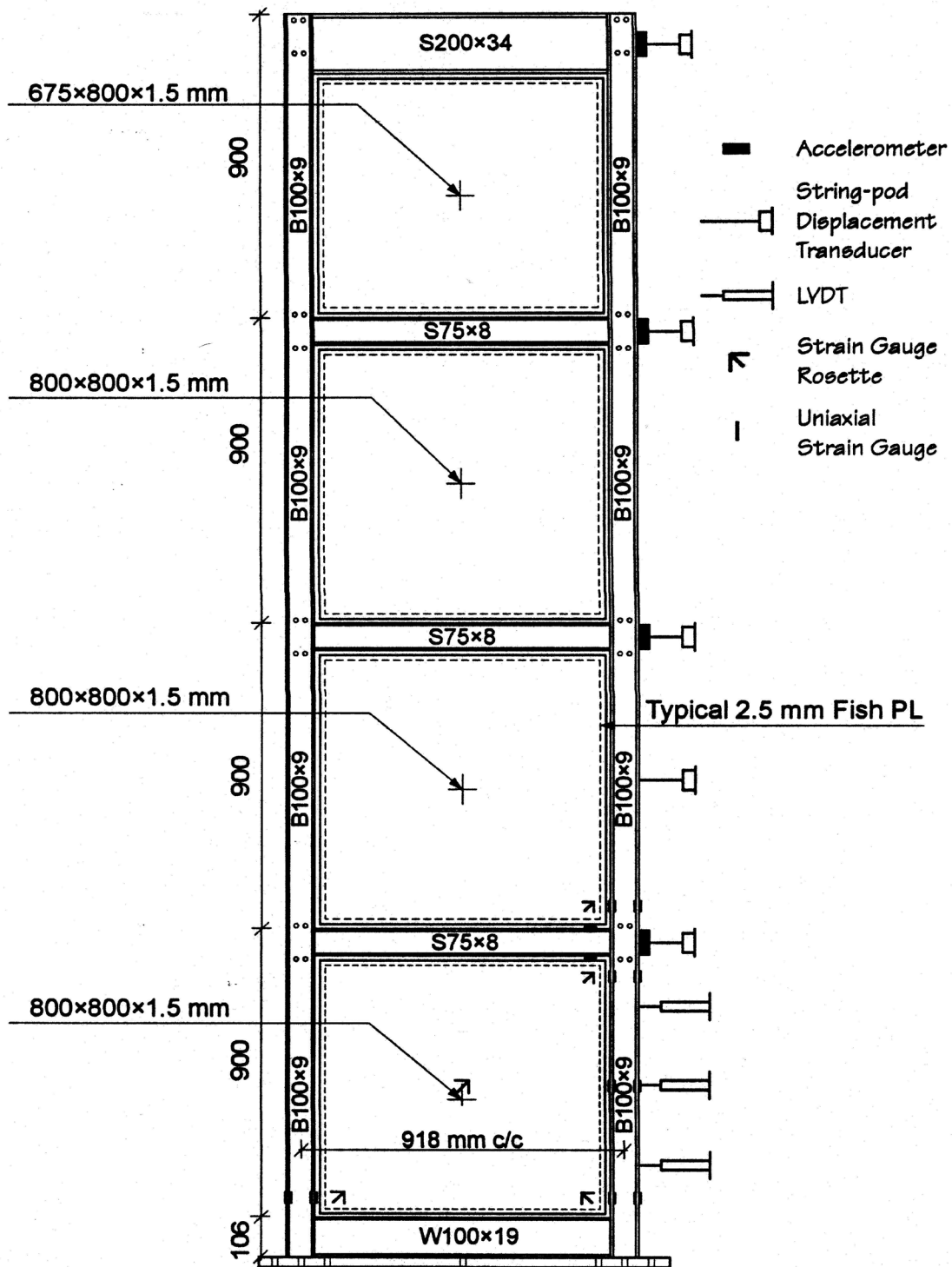
FIGURE 2-9 Schematic of Test Specimen (Rezai, 1999)

The shake table test specimen was one bay wide and four stories high, with a bay width of 918 mm and a story height of 900 mm. Plates were 1.5 mm thick and were welded to a 2.5 mm thick fish plate which in turn was welded to the members of the boundary frame. Figure 2-9 shows the

test specimen along with the instrumentation layout. An elaborate lateral bracing scheme was constructed to prevent out-of-plane failure of the frame at the floor levels. Gravity loading and mass for the dynamic shaking was provided by stacked steel plates at the various floor levels.

Four different ground motion records, scaled to several different peak ground acceleration levels, were used to excite the system. A total of 33 different motions were applied. The basic motions were the Joshua Tree and Tarzana Hill records from the 1992 Landers Earthquake, the 1992 Petrolia Earthquake, and a synthetic motion developed by Bell Communications Research. Additionally, four sine wave motions were also applied. The maximum target peak ground acceleration applied (2.678g) was from the Tarzana Hill record scaled at 150%. Impact and ambient vibration tests were also performed.

Due to limitations in the shake table capability, the plates remained mostly elastic for all ground motions applied. Some limited energy dissipation was observed in the first two stories. Some yielding was reported to have developed in a first story column and it's base plate. Shear deformations (decreasing interstory drifts with increasing height) were significant in the first stories, whereas, flexural deformations (increasing interstory drifts with increasing height) were reported to dominate the behavior of the upper stories.

Finite element and strip models of the test specimen of Lubell *et al.* (2000), which are reviewed in the following section, were generated. In both cases the models over predicted the initial stiffness. The strip model was able to adequately predict the first yield and ultimate strengths when compared with the experimental results of Lubell et al. (2000). However, it was found that the influence of overturning moment on the base shear versus roof displacement behavior is significant in the accuracy of the strip model. For tall slender walls, the strip model less accurately predicts the wall stiffness because it does not capture the flexural behavior of the upper stories. For shorter and wider walls, such as the Driver *et al.* (1997) test, the strip model was reported to give more satisfactory results. It was also found that modeling individual stories instead of the entire wall (as suggested at that time in Appendix M of CAN/CSA-S16.1-94) does not accurately represent the wall because it neglects the effects of global overturning moment on the base shear versus roof displacement behavior.

An alternative strip model was proposed in which the strips are reorganized to capture the variation in the inclination of the tension field across the plate. Additionally, an effective width concept was employed so that incomplete tension field action could be accounted for. This effective width depends on the stiffness of the boundary members. The proposed model was able to better represent the initial stiffness of the wall but did not accurately capture its yield and ultimate strengths.

2.10   Lubell, Prion, Ventura, and Rezai (2000)

Lubell *et al.* (2000) tested one four story and two single story steel plate shear walls. All specimens had aspect ratios of 1 to 1 with bay widths and story heights equal to 900 mm. All infill panels used 1.5 mm thick plates with a yield stress of 320 Mpa and the boundary frames used moment connections. The loading was applied as cyclic, quasi-static, following the ATC-24 protocol (ATC, 1992).

The first single story specimen was pushed to 7 times the yield displacement of the structure. This test was terminated because of the failure of a lateral brace due to excessive out of plane deflection of the top of the specimen. As a result, the top beam of the second test was stiffened to prevent out of plane displacement of the frame. The ultimate strength of the first single story specimen was found to be 200 kN with a yield strength of 180 kN and yield displacement of 9 mm. In the second test the yield strength was found to be 190 kN at a displacement of 3 mm with an ultimate strength of 260 kN at four times the yield displacement. Failure of the second specimen occurred when a column fractured after significant plastic hinging at a load of 190 kN and displacement of six times the yield displacement. The significant increase in the ultimate strength and stiffness of the second test was attributed to the stiffened upper beam. Anchorage of the tension field by use of a substantially stiff top beam was found to be of paramount importance in the design of steel plate shear walls and is necessary to achieve optimal performance.

The four-story steel plate shear wall specimen was subjected to equal lateral loads applied at each floor level. Gravity loads were applied using steel plates stacked at each story. This specimen was found to yield at a base shear of 150 kN and a first floor displacement of 9 mm. Failure

from global instability due to column yielding occurred at 1.5 times the yield displacement. It was observed from the hysteresis loops of the individual stories that the first story absorbed most of the inelastic action and damage. This trend was consistent with what Driver *et al.* (1997) and Rezai (1999) found in their multistory steel plate shear wall experiments. In all experiments by Lubell *et al.* (2000), significant pull-in of the columns was observed. It was reported that all walls ended up in an "hour-glass" shape after significant lateral cyclic displacements were applied. This lead to the conclusion that a capacity design of the bounding columns in a steel plate shear wall is necessary to ensure that the infill panels yield prior to column hinging and to minimize pull-in of the columns.

Strip models of the specimen were also developed to evaluate the accuracy of the modeling technique. It was found that the strip model overpredicted the elastic stiffness of the first single story test and the four story test, but predicted well the yield and ultimate strengths as well as the post-yield stiffness. When a stiffer upper beam was present, as in the second single story test, the strip model was found to give better results for the elastic stiffness. It was concluded that the strip model can accurately represent panels that are dominated by shear inelastic behavior. When flexural inelastic behavior governs, it was recommended that other more advanced modeling techniques be employed.

2.11 Mo and Perng (2000)

Mo and Perng (2000) experimentally tested four reinforced concrete frames infilled with corrugated steel plates to assess their adequacy as a lateral load resisting system. The single story test frames were 1125 mm wide by 900 mm high. Columns and beams were 150 mm by 150 mm and were detailed according to the special seismic requirements of ACI 1995 (ACI, 1995). The columns and beams had volumetric ratios of steel equal to 2.3% and 1.26% respectively. Four infill plate thicknesses were tested (0.3 mm, 0.4 mm, 0.5 mm, and 1.0 mm), and all were reported to have a yield stress of 495.12 MPa (71.8 ksi). All plates had a standard corrugation pattern similar to that of type B steel decks found in the United States and were connected to the frame using bolted connections. The plates were situated so that the longitudinal axis of the corrugations was horizontal, but the explanation for this design decision was not provided.

Loading was cyclic, quasi-static, with a total of 48 scheduled cycles over 24 increasing displacement steps. No gravity load was applied to the structure. The hysteresis loops for all the specimens were significantly pinched but showed good ductility for three of the four tests. In the 0.3 mm test, the plate failed around the connection to the concrete frame. It was concluded that the thickness was not sufficient to avoid tearing and bearing failure at this connection. The 0.4 mm and 0.5 mm tests performed well and developed yield base shears of 80.2 kN and 95.2 kN respectively. In the test of the 0.4 mm plate, the reported ductility factor was 3.89 and the failure mode was plate yielding and buckling prior to frame hinging. The test of the 0.5 mm plate yielded a ductility ratio of 2.89 and also achieved a ductile failure mode. In the case of the 1.0 mm plate, a brittle mode of failure was observed as the frame failed prior to plate yielding or buckling.

The results of these experiments were compared with those for conventional reinforced concrete moment frames and shear walls. It was observed that the frames infilled with corrugated steel plates had a lower ultimate strength but greater ductility and energy dissipation than reinforced concrete shear walls, and greater ultimate strength, ductility and energy dissipation than the moment frames. The researchers concluded that this type of infill wall is feasible because of good ductility and energy dissipation, that there is a limiting plate thickness to ensure ductile failure (plate thicknesses larger than this in the same frame lead to brittle collapses), and that there is also a minimum plate thickness needed to avoid local failure around plate connections.

2.12   CAN/CSA-S16-01 (2001)

Canada's standard on Limit States Design of Steel Structures, CAN/CSA-S16-01 (CSA, 2001), now includes mandatory clauses for the design of steel plate shear walls. Clause 20 gives design and detailing requirements for walls subjected to general loading and Clause 27.8 gives special seismic requirements. In regards to seismic design the Canadian standard considers two categories of steel plate shear walls; Type LD (limited ductility plate walls) and Type D (ductile plate walls). The major difference between the two is that the ductile plate walls include moment-resisting beam-to-column connections in the boundary frame whereas limited ductility walls do not.

The design procedure for steel plate shear walls according to CAN/CSA-S16-01 begins with preliminary proportioning using the equivalent story brace model (figure 2-1). Using simple statics, the required brace forces can be calculated from the design lateral loads. A required brace area (for an assumed yield stress) can then calculated for the required brace force. (2-1) is then used to calculate a required plate thickness from the required story brace area. The standard then requires the development of a strip model to represent the wall (figure 2-2). (2-4) is used to calculate the angle of inclination of the strips, but an average angle for the entire wall may used. To avoid excessive pull-in of the columns, CAN/CSA-S16-01 requires that the column moment of inertia to be greater than $0.00307th_s{}^4/L$, where t is the plate thickness, h_s is the story height, and L is the bay width (all in mm). Once the detailed model has been developed and the columns meet the flexibility criteria, the steel plate shear wall is deemed satisfactory to resist wind loads or other non-seismic lateral loads after checking appropriate drift limits.

For seismic design, further requirements are specified. Clause 27.8 requires that a capacity design of the columns be conducted for Type D walls. This is specified indirectly by the use of a factor B, defined as the ratio of probable shear resistance, V_{re}, at the base of the wall over the calculated factored design base shear. The probable shear resistance at the base of the wall is given by:

$$V_{re} = 0.5R_y F_y tL \sin 2\alpha \tag{2-5}$$

where R_y is the ratio of the expected (mean) steel yield stress to the design yield stress (specified as 1.1 for A572 Gr. 50 steel), F_y is the design yield stress of the plate, L is the bay width, and α is given by (2-4). The design axial forces and local moments in the columns are then amplified by this factor. More specifically, the column axial forces determined from the factored design overturning moment at the base of the wall are amplified by B and kept constant for a height of either two stories or L (the bay width), whichever is greater. The axial forces then are assumed to linearly decrease to B times the axial forces found from the actual factored overturning moment at one story below the top of the wall. The maximum value of B (which is meant to insure a ductile failure mode) can be limited to the value of the ductility factor R_μ assigned by CAN/CSA-S16-01. Drift, including amplification for inelastic action, must also be checked according to the applicable building code. For Type LD plate walls, there are no special seismic requirements.

SECTION 3

PLASTIC ANALYSIS AND DESIGN OF STEEL PLATE SHEAR WALLS

3.1   General

At the time of this writing, there are no U.S. specifications or codes addressing the design of steel plate shear walls. The 2001 Canadian standard, CAN/CSA-S16-01 (CSA, 2001), now incorporates mandatory clauses on the design of steel plate shear walls, as described in Section 2. One of the models recommended to represent steel plate shear walls, which was originally developed by Thorburn et al. (1983) and named the strip model, is generally recognized for providing reliable assessments of their ultimate strength (see figure 3-1). In this section, using this strip model as a basis, the use of plastic analysis as an alternative for the design of steel plate shear walls is investigated. Fundamental plastic collapse mechanisms are described for single story and multistory SPSW with either simple or rigid beam-to-column connections. The impact that the design procedure currently in place in the CAN/CSA-S16-01 standard has on the expected versus actual ultimate strengths of SPSWs designed per this procedure is also investigated.

3.2   Plastic Analysis of Steel Plate Shear Walls - Single Story Frames

In this section, plastic analysis of the strip model is used to develop equations for the ultimate capacity of different types of single-story steel plate shear walls. In cases where general equations depend on actual member sizes and strengths, procedures are presented to determine the necessary equations. In later sections the results of these analyses are used to develop a simple, consistent method for determining the preliminary plate sizes for steel plate shear walls.

27
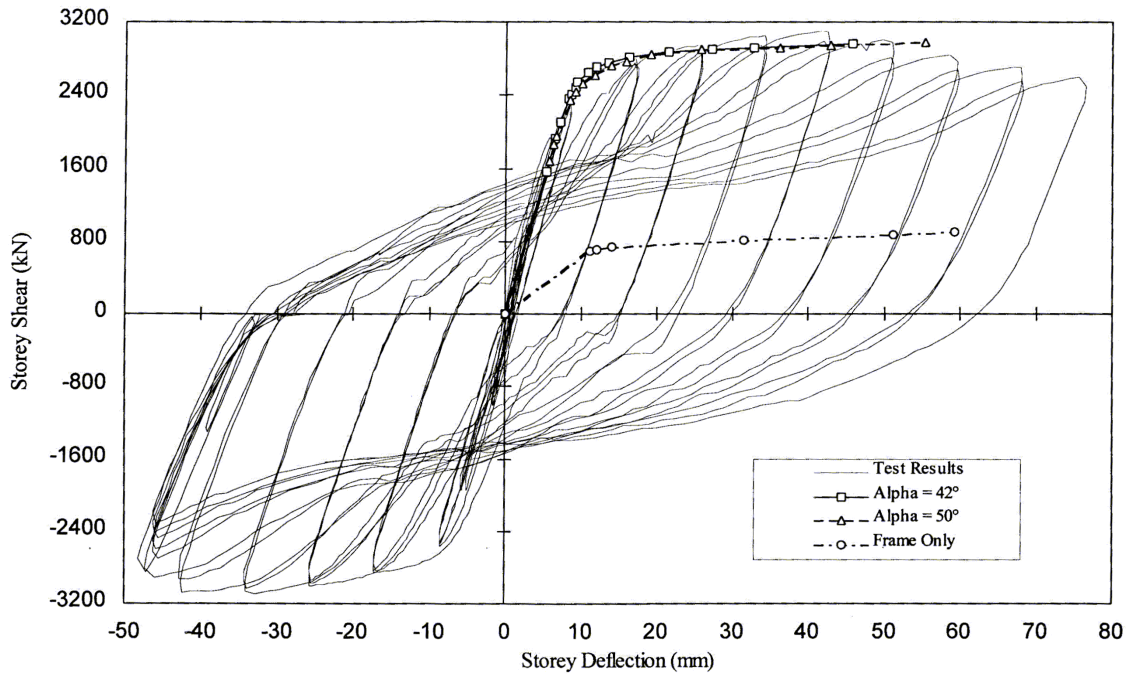
FIGURE 3-1 Experimental Results Compared With Strip Model (Adapted From Driver *et al.*, 1997)

3.2.1 Equilibrium Method - Simple Beam-to-Column Connections

First the ultimate strength of a single story steel plate shear wall having simple beam-to-column connections is found using the equilibrium method of plastic analysis. Consider figure 3-2, which shows a single story SPSW in a frame with pin-ended beams. The model is divided into three zones. Zones 1 and 3 contain strips which run from a column to a beam while zone 2 contains any strips that connect from the top beam to the bottom beam. Note that the strip spacing in the direction perpendicular to the strip is s, with the first and last (upper left and lower right) strips located at $s/2$ from the closest beam-to-column connections. The distance d_i from the beam-to-column connection to each strip is measured (again, perpendicularly to the strip) from the upper-left beam-to-column connection in zones 1 and 2, and in zone 3 from the lower right connection.

From figures 3-3a and 3-3b the applied story shear for zone 1 strips can be found in terms of the strip force F_{st}, the distance d_i, and the story height h_s, in two steps. First, summation of moments about point C (bottom of the left column in figure 3-3a) gives, $V_1 h_s = R_{by}L$ (where L is the bay width and R_{by} is the vertical support reaction at B). Then looking at the free body diagram of the

28

beam alone (figure 3-3b) and taking moments about point D, one obtains $R_{by}L = F_{st}d_i$. Therefore, the story shear due to the forces in zone 1 strips can be written as:

$$V_1 = \sum_{i=1}^{l} \frac{F_{st} d_i}{h_s}$$

(3-1)

where l is the number of strips in zone 1.
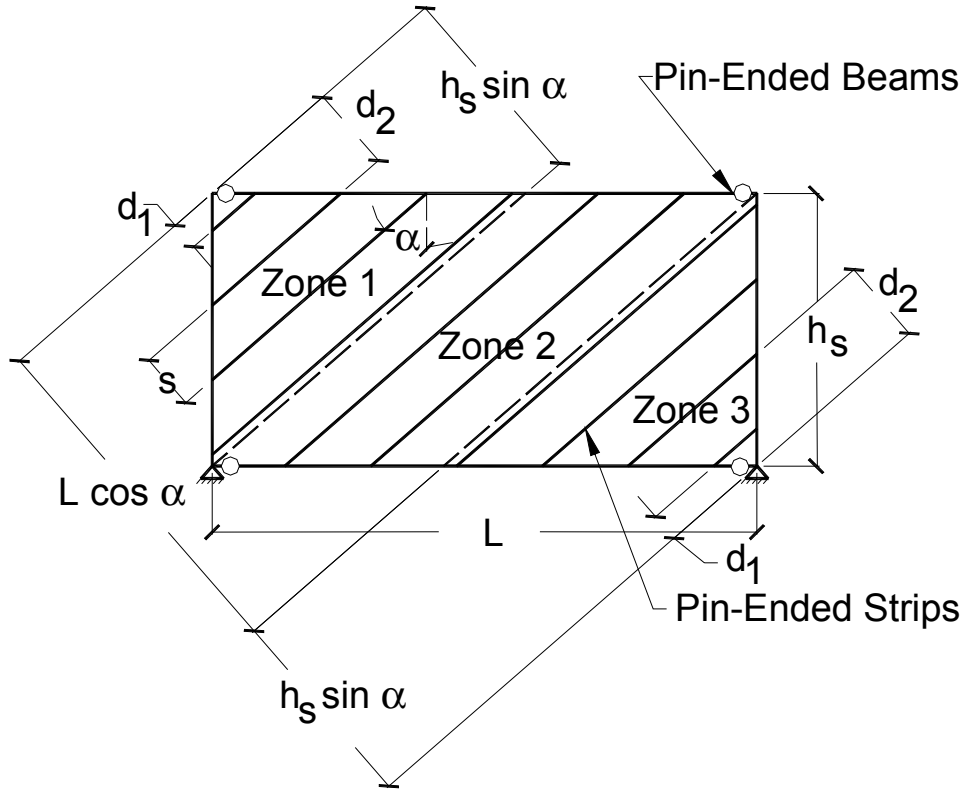
FIGURE 3-2 Single Story Strip Model

For zone 2, by taking moments about point C again (figure 3-4a), one obtains $V_2 h_s = R_{by}L + F_{st}(\sin \alpha)h_s - F_{st}d_j$. From the free body diagram of the beam (figure 3-4b), taking moments about point D, one finds $R_{by}L = F_{st}d_j$. The story shear due to the forces in zone 2 strips is therefore:

$$V_2 = \sum_{j=1}^{m} F_{st} \sin\alpha$$

(3-2)

where m is the number of strips in zone 2.
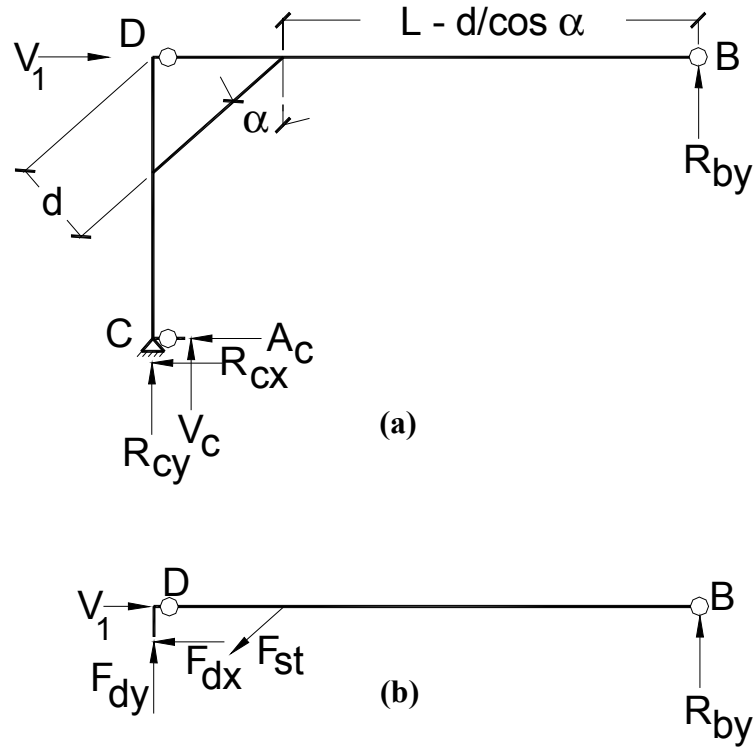
FIGURE 3-3 Zone 1 Free Body Diagrams
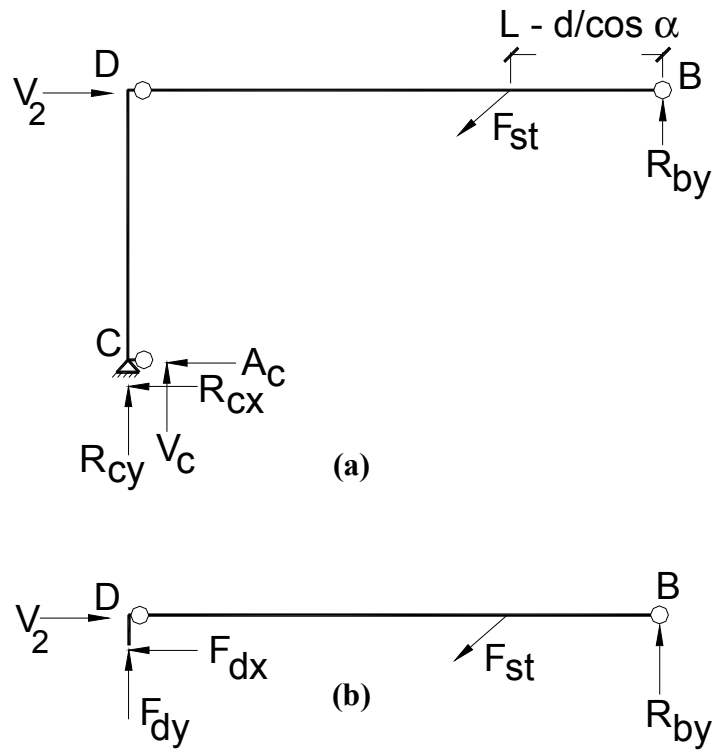
FIGURE 3-4 Zone 2 Free Body Diagrams

Finally, taking moments about point A in figure 3-5 one finds that the contribution to the story shear from zone 3 strips can be written as:

$$V_3 = \sum_{k=1}^{n} \frac{d_k F_{st}}{h_s}$$ (3-3)

where n is the number of strips in zone 3.
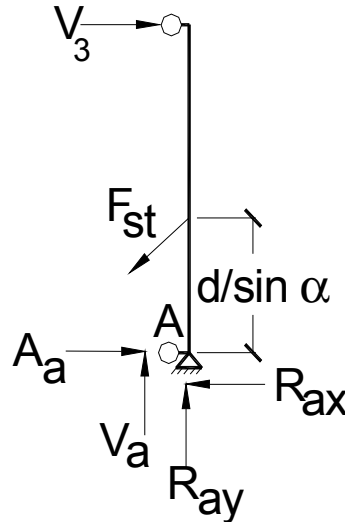
FIGURE 3-5 Zone 3 Free Body

Diagram

Now if it is assumed that there are n strips in each of zones 1 and 3 (due to equal strip spacing) the contributions from each zone can be combined to give:

$$V = \sum_{i=1}^{l} \frac{d_i F_{st}}{h_s} + \sum_{j=1}^{m} F_{st} \sin\alpha + \sum_{i=1}^{n} \frac{d_i F_{st}}{h_s}$$ (3-4)

From the geometry in figure 3-2 it can be shown that:

$$l = n = \frac{h_s \sin\alpha}{s} \qquad and \qquad m = \frac{L\cos\alpha - h_s \sin\alpha}{s}$$ (3-5)

Keeping in mind that the upper left and lower right strips are $s/2$ from the closest beam-to-column connections, the summation over d_i can be written as:

$$\sum_{i=1}^{n} d_i = \frac{n^2 s}{2}$$ (3-6)

31

Substituting (3-5) and (3-6) into (3-4), recognizing the fact that the strip force (F_{st}) is equal to the strip area (st) times the plate yield stress in tension (F_y) and using the trigonometric identity $[(1/2)\sin 2\alpha = \cos \alpha \sin \alpha]$ the story shear strength can be expressed as:

$$V = \frac{1}{2} F_y t L \sin 2\alpha \qquad (3\text{-}7)$$

Note that this equation is identical to the one used to calculate the probable shear resistance of a SPSW in the CAN/CSA-S16-01 procedure (2-5), without the material factor R_y.

3.2.2   Kinematic Method - Simple Beam-to-Column Connections

The same result can be obtained more directly using the kinematic method of plastic analysis. Consider the same frame with inclined strips shown in figure 3-2. When the shear force V displaces the top beam by a value Δ sufficient to yield all the strips, the external work done is equal to $V\Delta$ (see figure 3-6). If the beams and columns are assumed to remain elastic, their contribution to the internal work may be neglected when compared to the internal work done by the strips, hence, the internal work is $(n_b A_{st} F_y \sin \alpha)\Delta$, where n_b is the number of strips anchored to the top beam. This result can be obtained by the product of the yield force times the yield displacement, summed for all strips, but for simplicity it can also be found using the horizontal and vertical components of these values. Note that the horizontal components of the yield forces of the strips on the columns cancel (the forces on the left column do negative internal work and the forces on the right column do positive internal work) and the vertical components of all the yield forces do no internal work because there is no vertical deflection. Therefore, the only internal work done is by the horizontal components of the strip yield forces anchored to the top beam. Equating the external and internal work gives:

$$V = n_b F_{st} \sin\alpha \qquad (3\text{-}8)$$

From the geometry shown in figure 3-2, $n_b = (L\cos \alpha)/s$ and the strip force F_{st} is again $F_y ts$. Substituting these into (3-8) and knowing $(1/2)\sin 2\alpha = \cos \alpha \sin \alpha$, the resulting base shear relationship is again:

$$V = \frac{1}{2} F_y t L \sin 2\alpha \qquad (3\text{-}9)$$
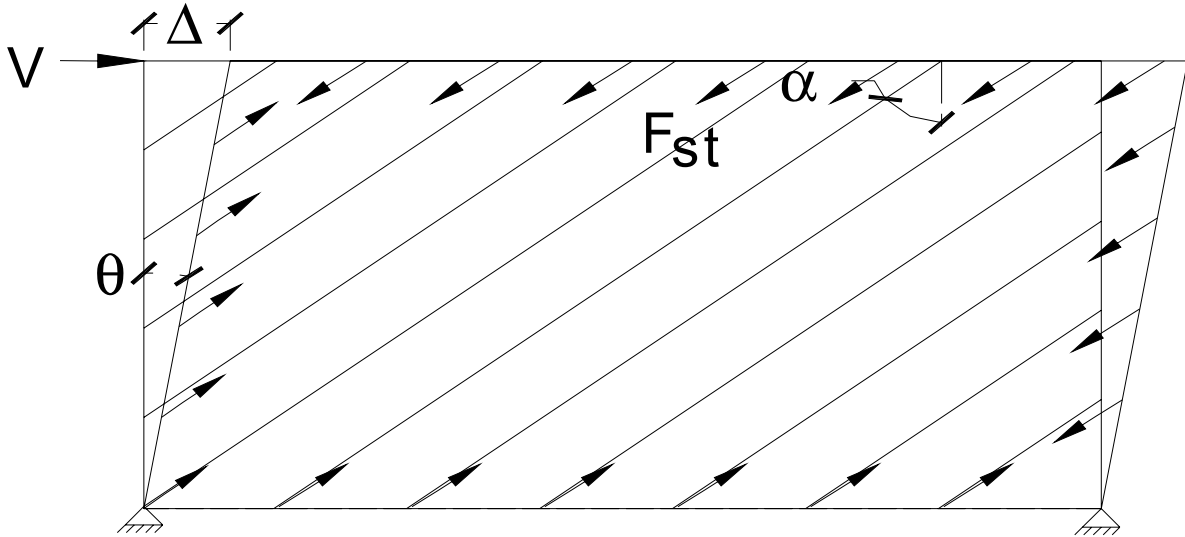
FIGURE 3-6 Single Story Kinematic Collapse Mechanism

3.2.3 Kinematic Method - Rigid Beam-to-Column Connections

In single story steel plate shear walls having rigid beam-to-column connections (as opposed to simple connections), plastic hinges also need to form in the boundary frame to produce a collapse mechanism. The corresponding additional internal work is $4M_p\theta$, where $\theta = \Delta/h_s$, is the story displacement over the story height, and M_p is the smaller of the plastic moment capacity of the beams M_{pb}, or columns M_{pc} (for most single-story frames that are wider than tall, if the beams have sufficient strength and stiffness to anchor the tension field, plastic hinges will typically form at the top and bottom of the columns and not in the beams). The ultimate strength of a single-story steel plate shear wall in a moment frame with plastic hinges in the columns becomes:

$$V = \frac{1}{2}F_y tL\sin 2\alpha + \frac{4M_{pc}}{h_s} \qquad (3\text{-}10)$$

In a design process, failure to account for the additional strength provided by the beams or columns results in larger plate thicknesses than necessary, this would translate into lower ductility demands in the walls and frame members, and could therefore be considered to be a conservative approach. However, to insure this ductile failure mechanism occurs, the columns and beams must be selected using capacity design principles.

3.3 Plastic Analysis of Steel Plate Shear Walls - Multistory Frames

For multistory SPSWs with pin-ended beams, plastic analysis can also be used to estimate the ultimate capacity. The purpose here is not to present closed-form solutions for all possible failure mechanisms, but to identify some key plastic mechanisms that should be considered in estimating the ultimate capacity of a steel plate shear wall. These could be used to define a desirable failure mode in a capacity design perspective, or to prevent an undesirable failure mode, as well as complement traditional design approaches.

In soft-story plastic mechanisms (figure 3-7a), the plastic hinges that would form in the columns at the mechanism level could be included in the plastic analysis. Calculating and equating the internal and external work, the following general expression could be used for soft-story i in which all flexural hinges develop in columns:

$$\sum_{j=i}^{n_s} V_j = \frac{1}{2} F_y t_i L \sin 2\alpha + \frac{4 M_{pci}}{h_{si}}$$

(3-11)

where V_j are the applied lateral forces above the soft-story i, t_i is the plate thickness at the soft-story, M_{pci} is the plastic moment capacity of the columns at the soft-story, h_{si} is the height of the soft-story, and n_s is the total number of stories. Note that only the applied lateral forces above the soft-story do external work and they all move the same distance (Δ). The internal work is done only by the strips on the soft-story itself and by column hinges forming at the top and bottom of the soft-story. Using the above equation, the possibility of a soft-story mechanism should be checked at every story in which there is a significant change in plate thickness or column size. Additionally, the soft-story mechanism is independent of the beam connection type (simple or rigid) because hinges must form in the columns, not the beams.
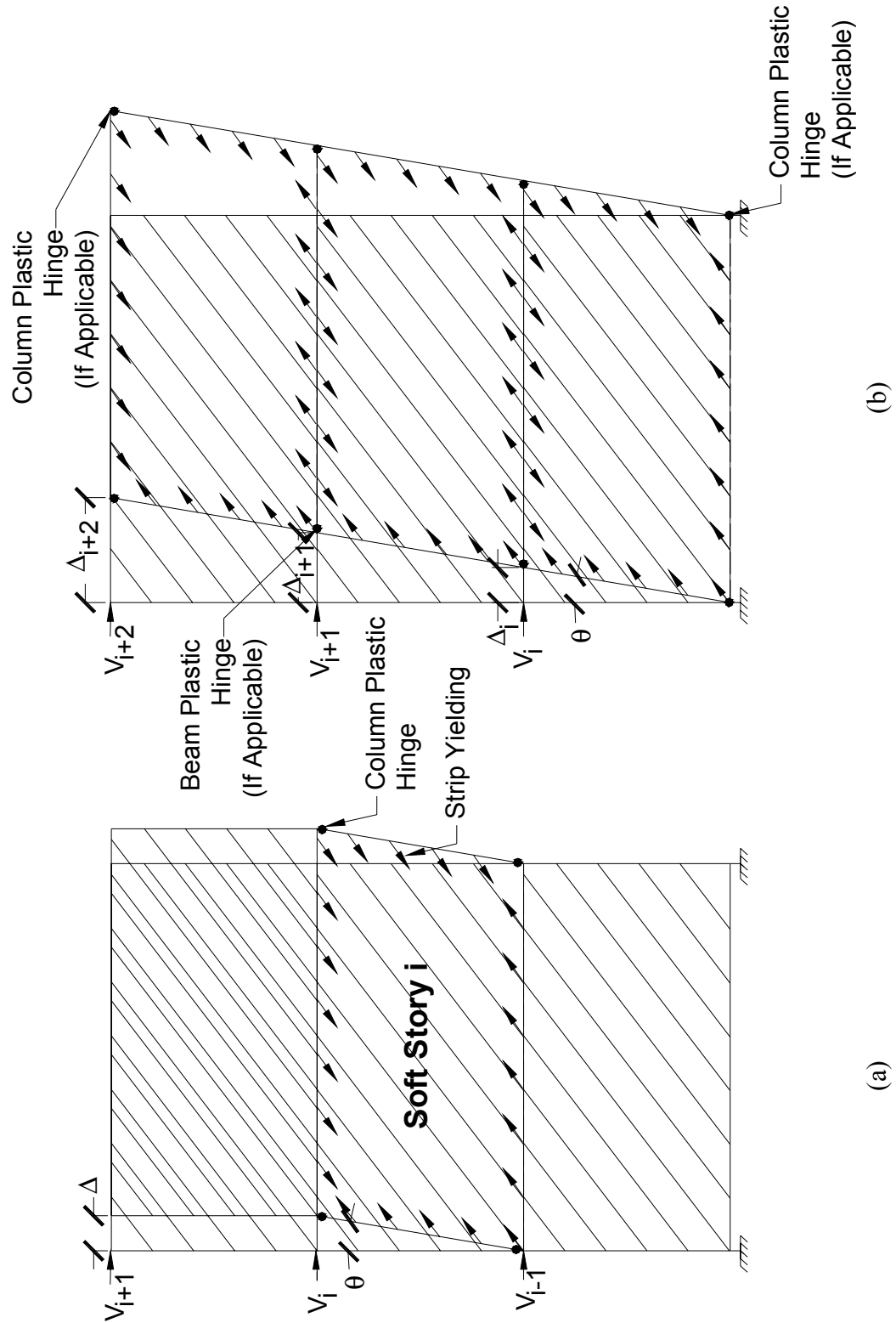
FIGURE 3-7 Examples of Collapse Mechanisms for Multistory SPSW

35

A second (and more desirable) possible collapse mechanism involves uniform yielding of the plates over every story (figure 3-7b). For this mechanism, each applied lateral force, V_i, moves a distance $\Delta_i = \theta h_i$, and does external work equal to $V_i \theta h_i$, where h_i is the elevation of the ith story. The internal work is done by the strips of each story yielding. It is important to note that the strip forces acting on the bottom of a story beam do positive internal work and the strip forces acting on top of the same beam do negative internal work. Therefore, the internal work at any story i is equal to the work done by strip yield forces along the bottom of the story beam minus the work done by strip yield forces on the top of the same beam. This indicates that in order for every plate at every story to contribute to the internal work, the plate thicknesses would have to vary at each story in direct proportion to the demands from the applied lateral forces. Even with this in mind, this mechanism provides insight into the capacity and failure mechanism of the wall. The general equation for the ultimate strength of a multistory SPSW with simple beam-to-column connections and this plastic mechanism (equating the internal and external work) is:

$$\sum_{i=1}^{n_s} V_i h_i = \sum_{i=1}^{n_s} \frac{1}{2} F_y (t_i - t_{i+1}) L h_i \sin 2\alpha \tag{3-12}$$

where h_i is the ith story elevation, n_s is the total number of stories, and t_i is the thickness of the plate on the ith story.

The ultimate strength of SPSW having rigid beam-to-column connections capable of developing the beam's plastic moment, can also be calculated following the same kinematic approach. The resulting general equation for the uniform yielding mechanism can be written as:

$$\sum_{i=1}^{n_s} V_i h_i = 2 M_{pc1} + 2 M_{pcn} + \sum_{i=1}^{n_s-1} M_{pbi} + \sum_{i=1}^{n_s} \frac{1}{2} F_y L h_i (t_i - t_{i+1}) \sin 2\alpha \tag{3-13}$$

where M_{pc1} is the first story column plastic moment, M_{pcn} is the top story column plastic moment, M_{pbi} is the plastic moment of the ith story beam, and the rest of the terms were previously defined. Note that it is assumed that column hinges will form instead of beam hinges at the roof and base levels. Sizable beams are usually required at these two locations to anchor the tension field forces from the infill plates and hence plastic hinges typically develop in columns there. However, this may not be the case for certain wall aspect ratios, and the engineer is cautioned to use judgement, as M_{pc1} and M_{pcn} may have to be replaced by M_{pb1} and M_{pbn} in some instances, where M_{pb1} and M_{pbn} are the plastic moment capacities of the base and roof beams respectively.

36

Furthermore, note that hinges were assumed to develop in beams at all other levels, which is usually the case as small beams are required there in well proportioned SPSW.

After examining the results of several different pushover analyses for three story SPSW with various plate thicknesses, it has been observed that the actual failure mechanism is typically somewhere between a soft-story mechanism and uniform yielding of the plates on all stories (especially considering practical designs in which the infill plates may be of only one or two thicknesses). Finding the actual failure mechanism is difficult by hand, therefore, a computerized pushover analysis should be used. However, the mechanisms described above will provide a rough estimate of the ultimate capacity. They will also provide some insight as to whether a soft story is likely to develop (by comparing the ultimate capacity found from the soft story mechanism with that of the uniform yielding mechanism).

3.4   Impact of Design Procedure on the Ultimate Strength of SPSW

3.4.1   CAN/CSA-S16-01 Approach

The procedure given for preliminary sizing of plates in CAN/CSA-S16-01 is simple but results in designs that may not be consistent with the demands implicit in the seismic force modification factor *R*. This inconsistency is introduced by the transition from the equivalent story brace model (used for preliminary proportioning and to select the amount of steel in the infill plates) to the multi-strip model (used for final analysis) which may change the ultimate capacity and shape of the pushover curve for the structure being designed.

In the equivalent story brace model, the ultimate capacity of the wall is only a function of the brace area, yield stress, and the bay geometry (aspect ratio). The story shear can be used to size the equivalent brace for each story by using simple statics (recall figure 2-1). Then (2-1) can be employed to relate the brace area to the plate thickness which, along with the strip spacing, gives the strip area for the detailed strip model. However, these two models will not produce the same ultimate capacity unless the aspect ratio of the bay is 1:1. To demonstrate this consider a single story SPSW (with simple beam-to-column connections) as shown in figure 3-2. Let the aspect ratio of the bay be equal to the bay width over the story height. Using the same design base shear, beam sizes, and column sizes, the area of the equivalent story braces were found for

several aspect ratios. From these, the plate thicknesses were found as described above and the detailed strip models were developed using (2-4) to find the angle of inclination for the strips.

Pushover analyses of all resulting SPSW were conducted and the resulting ultimate strengths of the various walls, designed to resist the same applied lateral loads, were compared. Figure 3-8 shows a plot of the base shear (normalized by dividing out the design base shear used to find the area of the equivalent story brace) versus percent story drift for several SPSW of different aspect ratios, obtained from pushover analyses of the strip models and equivalent story brace models. The resulting ultimate capacity of the strip model is below the capacity of the equivalent story brace model for all aspect ratios, except 1:1 for which it is the same. The difference between the capacity of the strip model and equivalent story brace model increases as the aspect ratio further deviates from 1.0. Figure 3-9 shows how the difference between the strip model capacity and the equivalent story brace model capacity changes with the aspect ratio of the bay. At an aspect ratio of 2:1 (or 1:2 since the results are symmetric in that sense) the strip model is only able to carry 80% of the base shear for which it should have been designed.
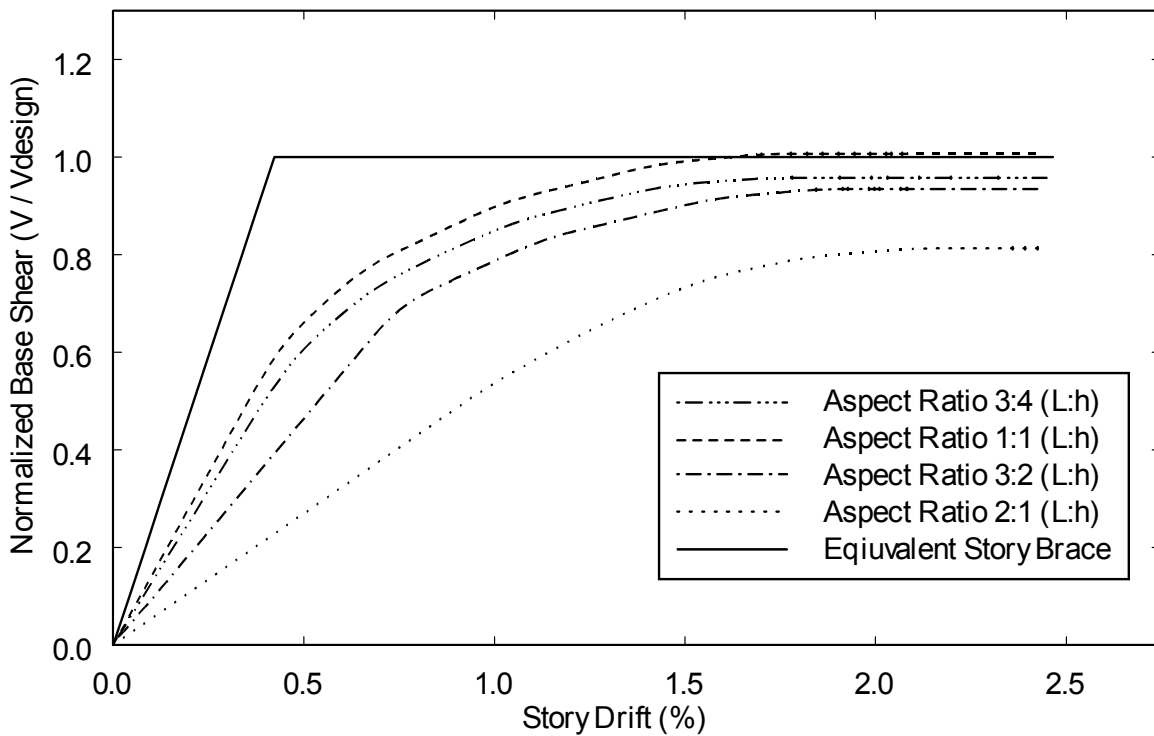
FIGURE 3-8 Pushover Curve for Different Aspect Ratios

38
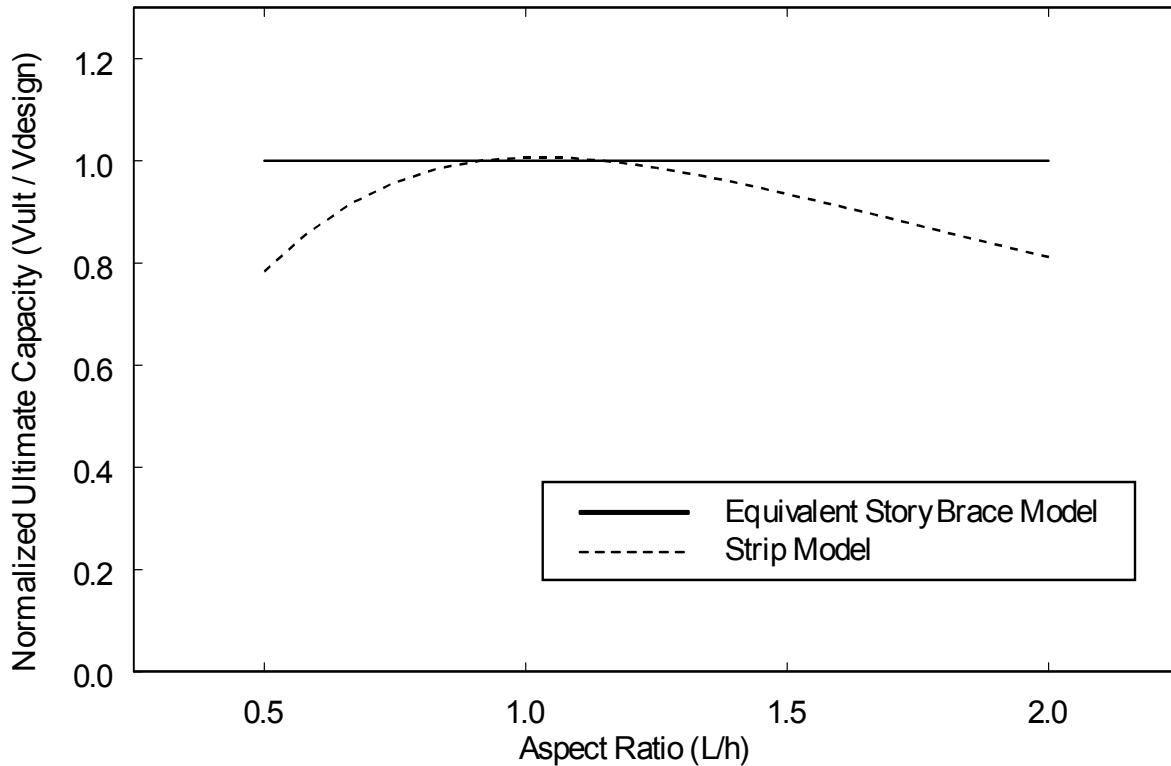
FIGURE 3-9 Variation of Ultimate Capacity With Aspect Ratio

3.4.2 Plastic Analysis

Using the results of the plastic analyses described previously, the infill plates of steel plate shear walls can be sized to consistently achieve the desired ultimate strength. The procedure is simple, even for a multistory SPSW, and neglecting the contribution of plastic hinges in beams and columns will always give a conservative design in the case of rigid beam-to-column connections. The proposed procedure requires the designer to:

(a)   Calculate the design base shear, and distribute it along the height of the building as described by the applicable building code;

(b)   Use the following equation to calculate the minimum plate thicknesses required for each story:

$$t = \frac{2 V_s \Omega_s}{F_y L \sin 2\alpha} \tag{3-14}$$

where, Ω_s is the system overstrength described below and V_s is the design story shear found using the equivalent lateral force method;

(c)   Develop the strip model for computer (elastic) analysis using (2-4) to calculate the angle of inclination of the strips;

39

(d)   Design beams and columns according to capacity design principles (to insure the utmost ductility) or other rational methods using plate thicknesses specified (in case those exceed the minimum required for practical reasons);

(e)   Check story drifts against allowable values from the applicable building code;

Note that (3-14) is identical to (3-9) but modified to account for the proper relationship between the equivalent lateral force procedure and R, the seismic force modification factor. Figure 3-10 is the generic pushover curve used to define R, where R_μ is the ductility factor, V_y is (for practical purposes) the fully yielded base shear, Ω_o is the overstrength factor, V_s is the design base shear, V_{eu} is the ultimate elastic base shear, Δ_{max} is the displacement at the ultimate elastic base shear, Δ_s is the displacement at the design base shear, Δ_y is the displacement at the yield base shear, μ_s is the displacement ductility factor, and C_d is the elastic displacement amplification factor. Note the distinction between V_y (the yield base shear) and V_s (the design base shear). Because (3-9) was obtained from plastic analysis of the strip model, it gives the maximum strength achieved at the peak of the pushover curve, which is V_y. Therefore, to account for this and to use the calculated design base shear, V_s, from the equivalent lateral force procedure with (3-9) to size the infill plates of a steel plate shear wall, V_s must be amplified by the overstrength factor. In this particular case the majority of the overstrength factor comes from the system overstrength factor as described below.
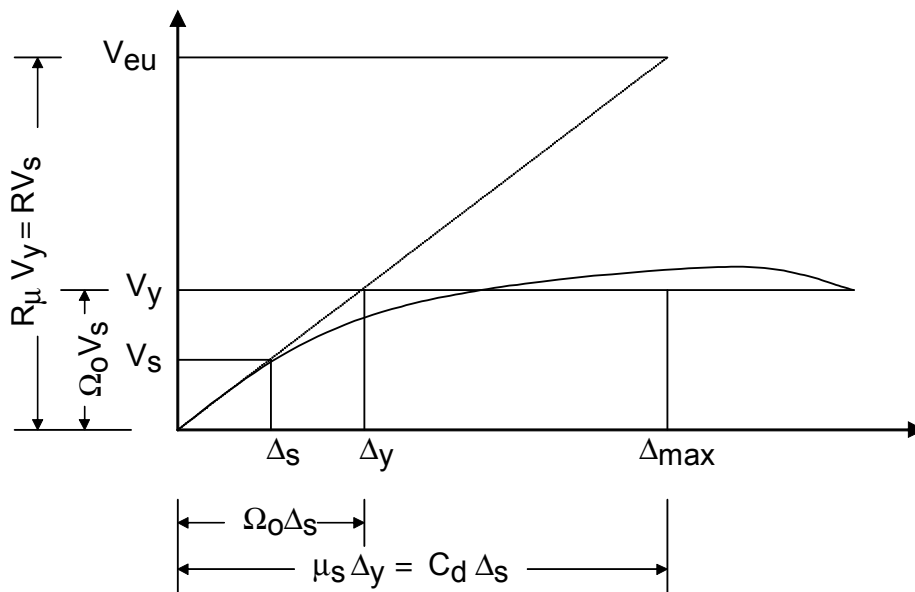
FIGURE 3-10 Generic Pushover Curve

40

Using the concepts presented in FEMA 369 (FEMA 2001), the R factor can be expressed as:

$$R = R_\mu \Omega_o = R_\mu \Omega_D \Omega_M \Omega_S \qquad (3\text{-}15)$$

where Ω_D is the design overstrength factor, Ω_M is the material overstrength factor, and Ω_S is the system overstrength factor. Although the quantification of Ω_D, Ω_M, Ω_S, are to be determined by panels of experts in code committees, the following observations are submitted for consideration. According to FEMA 369 these overstrength factors may be thought of as follows:

- Ω_D is to account for overstrength resulting from the design procedure. This would occur in drift controlled designs and designs in which architectural considerations may result in overstrength. For most low to medium rise SPSW, this is unlikely to be an issue and Ω_D could be considered as low as 1.0.

- Ω_M accounts for overstrength due to strength reduction factors used in load and resistance factor design, strain hardening, and the ratio of mean to specified yield stress. In this particular case R_y already accounts for the ratio of mean to specified yield stress in the capacity design approach and there is no strength reduction factor involved in the sizing of the infill plates. Furthermore, simple calculations would show that strain hardening would begin to develop at drifts of approximately $0.02h$, the typical drift limit, assuming a strain of 0.01 before strain hardening. Therefore, Ω_M may be taken as low as 1.0 as well.

- Ω_S accounts for the difference between the ultimate lateral load and the load at first significant yielding. Based on pushover results, the system overstrength, Ω_S, appears to vary between 1.1 and 1.5 depending on aspect ratio.

Using these definitions, it appears that only the system overstrength factor needs to be used to amplify the design base shear (or reduce the plastic capacity) in order to use (3-9) for the design of infill plates for steel plate shear walls. Therefore, (3-14) is recommended, with values for the system overstrength factor taken between 1.1 and 1.5, the actual system overstrength factor can be obtained from a pushover analysis, or conservatively used as 1.5.

Incidentally, on the basis of the work presented above, the CAN/CSA-S16-01 procedure should be modified to eliminate the possibility of designs having less-than-expected ultimate strength. For this purpose, (2-1) could be rewritten as:

$$t = \frac{2A\lambda \sin\theta \sin 2\theta}{L \sin^2 2\alpha} \qquad (3\text{-}16)$$

where λ is a correction factor obtained by calibrating the equivalent story brace model to the plastic analysis results presented in this section. Setting (3-16) equal to (3-14) and solving for λ gives:

$$\lambda = \frac{\Omega_s \sin 2\alpha}{\sin 2\theta} \qquad (3\text{-}17)$$

3.5 Summary

The CAN/CSA-S16-01 procedure for the analysis and design of steel plate shear walls was reviewed in Section 2 and instances where this procedure can lead to unconservative designs with lower than expected ultimate capacity have been identified above. Plastic collapse mechanisms for single and multistory SPSW with simple and rigid beam-to-column connections have been investigated and simple equations that capture the ultimate strength of SPSW have been developed. Using the results of these plastic analyses a new procedure for the sizing of the infill plates has been proposed. The proposed procedure allows the engineer to control the ultimate failure mechanism of the SPSW, and directly accounts for structural overstrength. The proposed procedure also eliminates the possibly unconservative designs that could result from the CAN/CSA-S16-01 procedure.

SECTION 4

EXPERIMENTAL DESIGN AND SETUP

4.1 General

This section describes the design, setup, and instrumentation of three light-gauge steel plate shear wall (SPSW) specimens for quasi-static testing. Two specimens, F1 and F2, were designed with light gauge flat plate infills and the third specimen, C1, was designed to with a corrugated infill plate (cold-formed steel deck). All specimens were designed in the perspective of a seismic retrofit and to meet three major goals, namely, mobility, low impact on existing framing, and a substantial increase in energy dissipation capability compared to that of the existing framing. Additionally, the retrofits were designed provide an increase in the stiffness and ductility of the structural system. The goal of mobility is not typical of seismic retrofit applications so a brief explanation follows.

As described in section 4.2, the test specimens have been derived from prototype light-gauge steel plate shear wall designs for the seismic retrofit of a particular hospital structure. Since hospital owners are frequently rearranging their floor plans by relocating partition walls, it was conceived that special infill panels designed for seismic retrofit could be an attractive solution if they could serve as partition walls as well as be moveable (with engineering guidance) to allow hospital floor plans to be reconfigured as needed. As described in Section 4.2, this is achieved using bolted connections for the infills to the existing framing.

Following discussion of the specimen design, materials used in the fabrication of the specimen are discussed and coupon test results are shown. Next, the complete experimental setup is described. Also presented in this section is a description of the design and setup of the foundation beam and clevises upon which the specimen is mounted, the lateral bracing provided,

the actuator used, and the method of bolt tensioning used to insure slip-critical connections. Lastly, a complete description of the instrumentation used on the three specimens is given.

4.2   Design of Test Specimens

The selection of the test specimens was done such that representative frame aspect ratios and plate thicknesses for light-gauge infills were obtained. The MCEER Demonstration Hospital (Yang and Whittaker, 2002) was used for this purpose. For the selected 4-story frames described below, seismic loads were calculated and the infill plates for prototype seismic retrofit designs were sized to resist the corresponding demand. Limitations of the equipment available for quasi-static testing in the Structural Engineering and Earthquake Simulation Laboratory (SEESL) at the University at Buffalo were also considered. As a result of these considerations the overall size of the specimens (bay width and story height) was designed so that the infill thicknesses would remain as in the prototype seismically retrofitted hospital. Additionally, only single story specimens were designed and tested, each specimen representing the first story of the MCEER Demonstration Hospital.

It was determined from the onset that at least two specimens would be constructed. The first would use a thin flat infill plate and the second a thin corrugated infill plate of the type commonly used in metal roof deck. Following the unsuccessful testing of the specimen with a flat infill plate, as discussed in Section 5, a third specimen utilizing a similar infill with a different connection to the surrounding framing members was also designed, constructed and tested. The design of the two flat infill specimens, F1 and F2, was identical except for the detail of the connection of the infill to the framing members.

4.2.1   Description of the MCEER Demonstration Hospital

The MCEER Demonstration Hospital is a four-story steel framed building with plan dimensions of 83.5 meters in the east-west direction and 17.2 meters in the north-south direction. The floor plan is shown in figure 4-1. The first story has a height of 4.1 meters and the others are 3.8 meters high. Gravity framing consists of 140 mm thick reinforced concrete floor slabs on metal deck that rest on steel floor beams and girders which carry the gravity loads to columns. In the north-south direction (the direction of primary interest) there are four moment-resisting 3-bay

frames that act as the primary lateral load resisting system (located on frame lines B, H, J, and N).   The remaining frames (termed gravity frames) in the north-south direction utilize web-angle connections that are assumed to have no resistance to lateral loading. Yang and Whittaker (2002) describe several sets of steel section sizes meant to represent hospitals constructed in different time periods and locations, therefore, satisfying different building code requirements. The design representing a typical hospital constructed on the west coast in the 1960's (WC60) was used in this study.
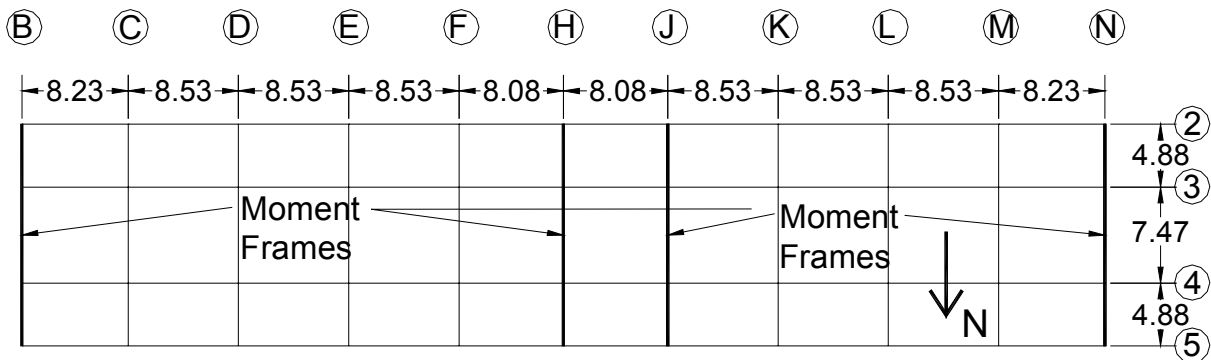
FIGURE 4-1 Floor Plan of MCEER Demonstration Hospital (Dimensions in meters)

(Yang and Whittaker, 2002)

The prototype on which basis the test specimens would be designed was considered to be a seismic retrofit for the hospital framing in the north-south direction. To achieve the goal of minimizing the forces applied to the existing framing of the prototype by the yielding infill plates (to avoid also having to strengthen the columns) it was decided that every line of gravity framing in the north-south direction would be retrofitted. The middle bay (between framing lines 3 and 4) was chosen as the location for the retrofit on each frame line.

4.2.2   Design Loads for MCEER Demonstration Hospital

The equivalent lateral force procedure of FEMA 302 (FEMA, 1997) was used to calculate a design base shear. Tributary gravity loads for one bay of north-south framing were determined. These and a portion of the design live load were used as the active seismic weight for a single gravity frame line. For the purpose of this report it was assumed that the hospital is located in Northridge, Ca. on a class D soil. Because SPSW do not appear in FEMA 302, an *R* factor from the Canadian Standard, CAN/CSA-S16-01 (CSA, 2001) was used. For limited ductility SPSW

(i.e. SPSW in frames with simple beam-to-column connections) CSA prescribes an R of 3.33 which was used for calculation of the base shear. An importance factor, I, of 1.5 was used because this is considered a critical facility. The resulting seismic coefficient, C_s, was determined to be 0.58 and the corresponding base shear tributary to one of the gravity frames was approximately 1420 kN. Note that the calculation of base shear applied to one of the gravity frames neglected the stiffness of the existing moment frames (they were assumed to have a small stiffness relative to the infilled gravity frames) as well as the effect of torsional response in plan, but still provides a reasonable basis to develop plate sizes.

4.2.3   Plate Thicknesses

For the design base shear calculated as described above, plate thicknesses for both the flat and corrugated plate scenarios were found using the procedure described in Section 3. Minimum required plate thicknesses at the first floor level were found to be 22 Gauge (0.75 mm or 0.0295 in) for the corrugated infill plate of specimen C1, and 20 Gauge (1.0 mm or 0.0396 in.) for the flat infill plates of specimens F1 and F2. A yield stress of 380 MPa (55 ksi) was assumed in both cases. For specimen C1, using a corrugation profile equal to that of Type B steel deck with the corrugations orientated at 45 degrees from the horizontal, the required plate thickness can be calculated using a modified version of (3-9), namely,

$$t = \frac{2V}{R_c F_y L \sin 2\alpha} \tag{4-1}$$

where R_c is the ratio of one wavelength of corrugation (l_w) to the projected flat length of one corrugation (l_p). This is shown schematically in figure 4-2.

Strip models of the infill plates with the surrounding members of the hospital gravity framing were made using SAP2000 (CSI, 1997) to evaluate the adequacy of the existing structural elements. It was determined from pushover analyses of the strip models that some minor column upgrades would be needed as well as stiffening of the beams at the roof and foundation levels to anchor the tension field developing in the plates. However, because the required increase in column moment of inertia was small (and could be achieved with the addition of cover plates), it was concluded that the proposed light-gauge steel infill plates could be an acceptable retrofit strategy for the demonstration hospital.
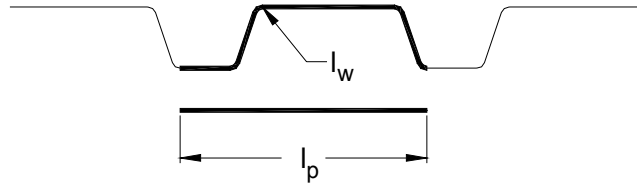
FIGURE 4-2

l_p and l_w for Corrugated Infill Plates

4.2.4 Overall Specimen Size

As stated in Section 4.2, the infill plate thicknesses for the specimens were selected to be identical to those for the prototype retrofits for the MCEER Demonstration Hospital. This was done to maintain practical plate gauge thicknesses. However, the maximum force available for quasi-static testing using a single actuator in the SEESL is 1110 kN (250 kips). Therefore, the bay width had to be scaled down from the prototype, as this is the only other parameter (aside from yield stress and plate thickness) that determines the ultimate strength of steel plate shear walls in single story frames with simple beam-to-column connections (see (3-9)). However, the aspect ratio of the prototype hospital retrofit of 2:1 (L:h) was maintained for the specimens. Following consideration of the above constraints, the bay width of the specimens was designed to be 3660 mm (12 ft.), or approximately ½ the width of the middle bay of the north-south framing of the hospital. From this, a story height of 1830 mm (6 ft.) was determined from the 2:1 aspect ratio.

These dimensions, along with the same plate thicknesses determined above, led to ultimate strengths of approximately 710 kN (160 kips) and 645 kN (145 kips) for the corrugated and flat walls, respectively (using a yield stress 380 MPa (55 ksi) for each). This was determined to be adequate because the boundary frame was likely going to use web-angle beam-to-column connections which are partial moment connections and will add to the base shear. Resulting slenderness ratios (L/t) were 4880 for specimen C1 and 3636 for specimen F1 and F2.

It is worthwhile to comment on the consequences of scaling the specimen height and width without scaling the infill thickness. First, the slenderness ratio of the test specimens were approximately ½ of what they would be in the prototypes. However, the buckling strengths of these light-gauge SPSW are negligible and since the slenderness ratio in the prototypes are twice

47

that of the test specimens, their buckling capacity would also be negligible. Furthermore, there have been several experimental studies involving specimens with slenderness ratios of 300 to 1000, so a study involving a much larger slenderness ratio fills a void in the knowledge base of SPSW behavior.

The second effect of scaling the bay width of the test specimens is that the ultimate strengths of the prototype SPSW would be about twice what will be found experimentally (see (4-1)). Lastly, the forces on the boundary frame members from the tension field action of the infills would be applied over a distance twice as large in the prototypes than in the test specimens, resulting in correspondingly larger design forces and moments. However, since the beams and columns are designed to remain elastic (see Section 4.2.5), scaling the experimentally determined forces and moments to what they would be in the prototype is should be straightforward and not of concern.
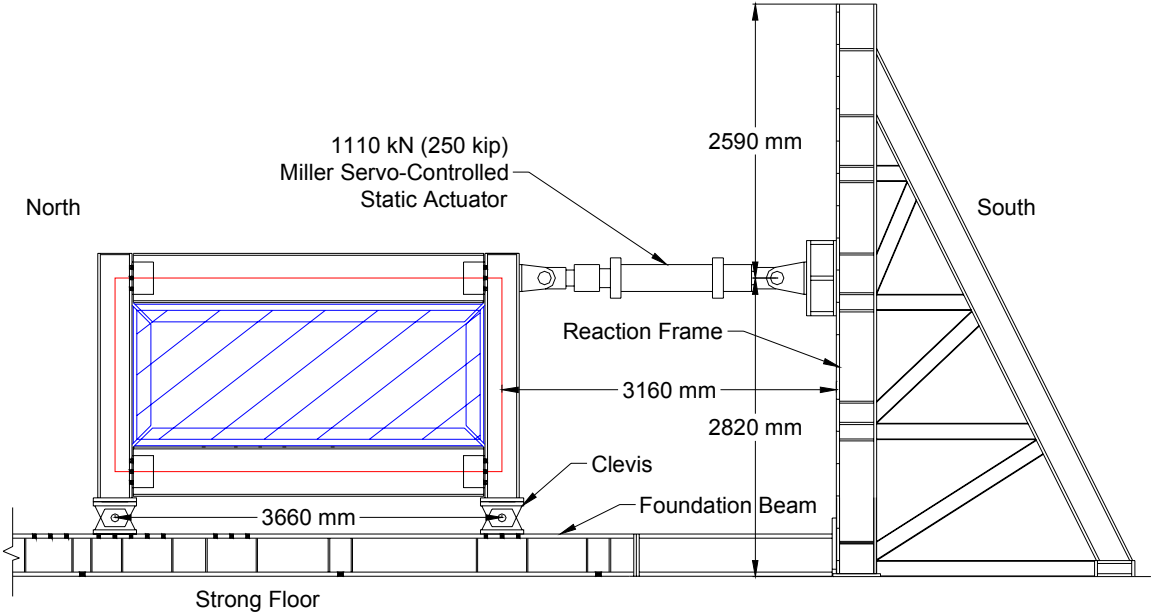
FIGURE 4-3 Test Setup

4.2.5 Design of Boundary Frames

Figure 4-3, a schematic of the entire setup, is now presented to aid in the description of the design of the boundary frames and test setup. After establishing the centerline dimensions of the frame, the design of the framing members around the plates was done so that they would remain elastic under the maximum possible loading. This was done to insure the safety of the test and so that the same boundary frame could be reused in future experiments.

To account for the possibility of obtaining infill materials with larger yield stresses than the 380 MPa (55 ksi) initially assumed, and to account for any possible strain hardening, the boundary frame was designed as if the infill could develop the full capacity of the horizontal actuator, i.e. 1110 kN (250 kips). SAP2000 pushover analyses of strip models of the test specimens (using plate yield stresses selected to return the maximum actuator force as the base shear) were used to
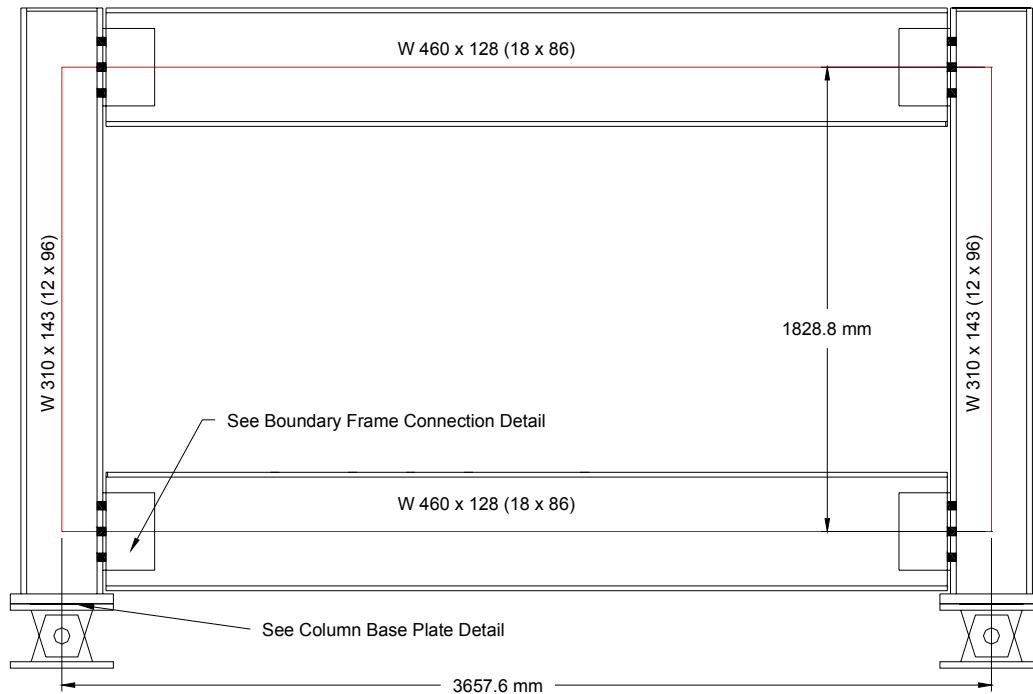
FIGURE 4-4 Boundary Frame Detail

determine the maximum moments, shear forces, and axial forces in the boundary frame members. The beams and columns were then designed to remain elastic under these actions with safety factor 2.0. These design actions and some practical considerations (i.e. eliminating the need for stiffeners) resulted in the selection of W310x143 (W12x96) columns and W460x128 (W18x86) beams. Figure 4-4 shows the boundary frame, overall dimensions, and section sizes.

4.2.6 Design of Beam-to-Column Connections

To maintain similarity to the gravity frames in the demonstration hospital, a web-angle beam-to-column connection was designed. Standard procedures for the design of web-angle connections found in the AISC LRFD manual (AISC, 1998) were employed (although inelastic behavior of the angles was impossible to prevent at the large drifts needed to fail the specimens). The bolts
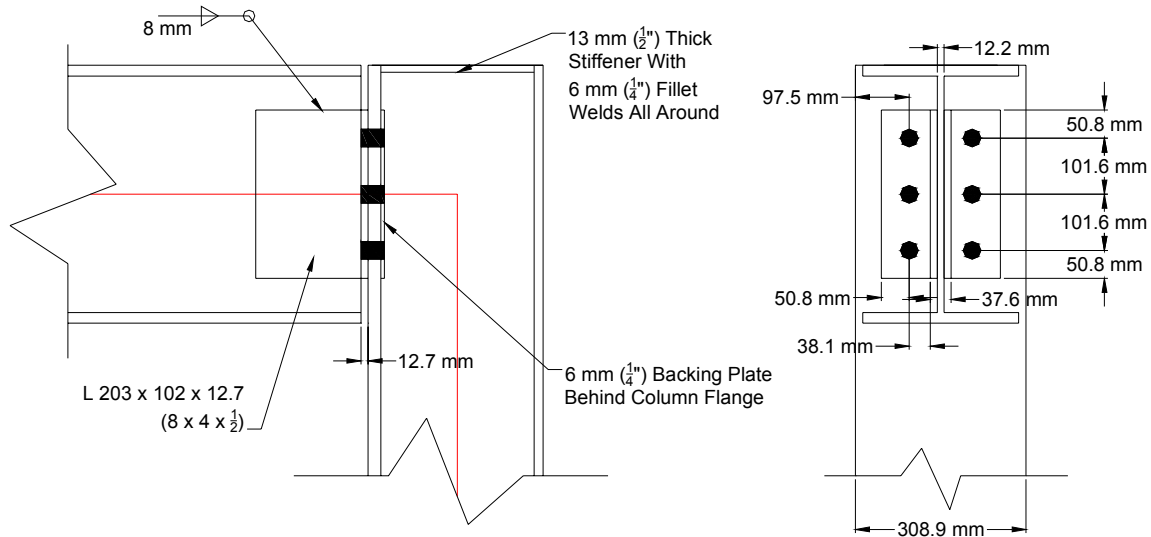
FIGURE 4-5 Beam-to-Column Connection Detail

to the column flange were designed to be slip-critical under the maximum actuator load with a safety factor of 2.0. A detail of the web-angle connection is shown in figure 4-5.

4.2.7   Design of Column Base Plates

The column base plates were designed to remain elastic for the maximum actuator load that could be applied to the specimens with a safety factor of 2.0. Prying action of the plates under the uplift forces due to the overturning moment in combination with the horizontal shear forces dominated the design. The resulting design made use of 25 mm (1") thick base plates with 5 mm (3/16") fillet welds around the column perimeter and six 38 mm (1-1/2") diameter A490 bolts to connect the base plates to the clevises. The bolts were designed as slip-critical under the maximum actuator load. Figure 4-6 shows the detailed column base plate.

4.2.8   Design of Infill Plate-to-Boundary Frame Connections

The design of the infill plate-to-boundary frame connection presented some unique challenges due to the thin plates selected. Such plates made a bolted connection through the infill material impossible because net section fracture governed over the gross section yielding of the plates. In order to dissipate energy, the plates must yield and the plate connection to the boundary frame

50

40 mm ($1\frac{9}{16}$") Holes
(for 38 mm ($1\frac{1}{2}$") A490 bolts)

114.3 mm

146.1 mm   146.1 mm

88.9 mm

41.8 mm

W 310 x 143
(12 x 96)

457.2 mm

74.7 mm

25 mm (1") Thick Plate

203.2 mm

5 mm (3/16") Fillet Weld All Around

57.2 mm   57.2 mm

88.9 mm

406.4 mm
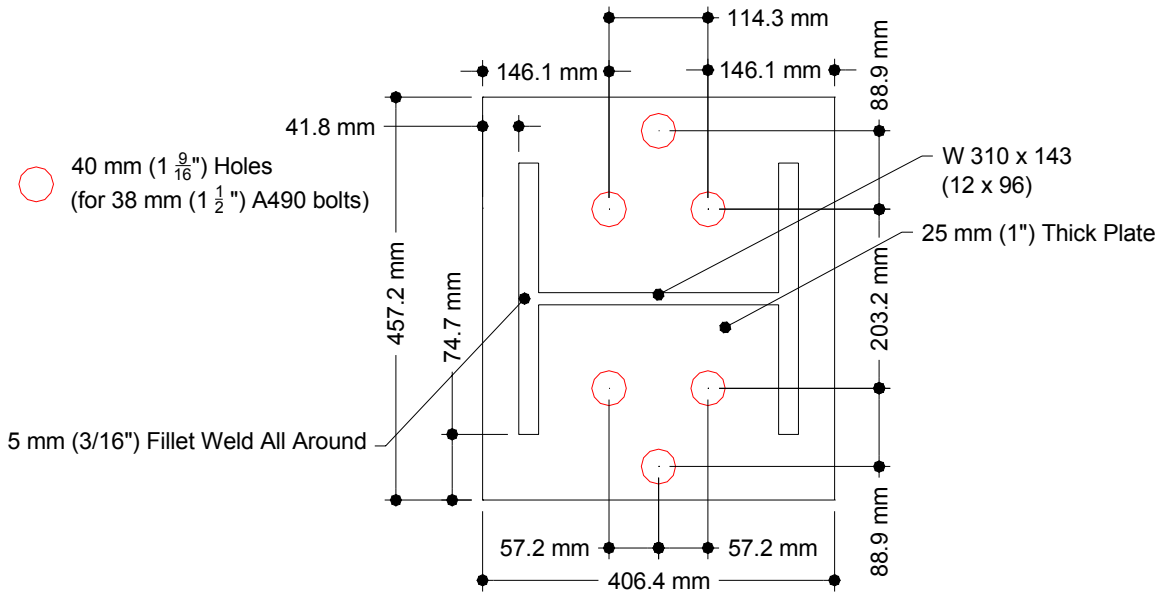
FIGURE 4-6 Column Base Plate Detail

20 Ga. Plate
t = 0.9 mm (0.0358")

20 Ga. Plate
t = 1.0 mm (0.0385")

108 mm ($4\frac{1}{4}$") Min Epoxy
Depth and Plate Overlap

WT 180 x 39.5
(7 x 26.5)

5 mm

WT 180 x 39.5
(7 x 26.5)
Plate Overlapped
50 mm (2")

29 mm ($1\text{-}\frac{1}{8}$") Dia.
A490 Bolts @
305 mm (12")
o.c. Into Page
(TYP)

152.4 mm

29 mm ($1\text{-}\frac{1}{8}$") Dia.
A490 Bolts @
305 mm (12")
o.c. Into Page
(TYP)

152.4 mm

W 460 x 128 (18 x 86)
Beam or
W 310 x 143 (12 x 96)
Column

W 460 x 128 (18 x 86)
Beam or
W 310 x 143 (12 x 96)
Column
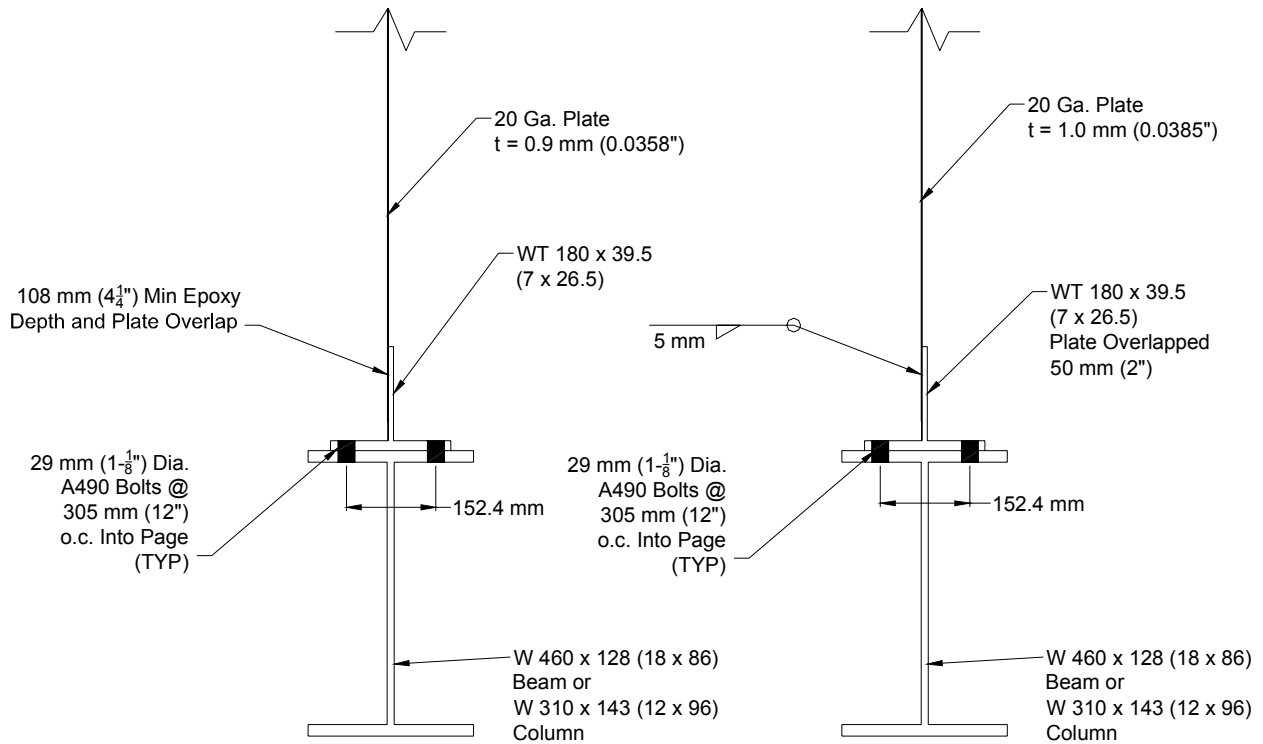
FIGURE 4-7 Flat Infill Plate Connection Details

must avoid net section fracture. Special approaches had to be taken for the connections as shown in the following sections.

4.2.8.1 Flat Infill Plate Specimens (F1 and F2)

For the flat plate specimens, two different infill plate-to-boundary frame connections were employed, resulting in specimens F1 and F2. The first approach (used in specimen F1) relied on an industrial strength epoxy, Hysol 9460, manufactured by the Dexter Corporation and distributed by Wolcott Park, Incorporated. Selection of the epoxy is discussed in Section 4.2.8.3 and the connection detail is shown in figure 4-7a. The second connection (used in specimen F2) was a welded connection and is shown in figure 4-7b.

Each of the flat plate specimens used a WT180x39.5 (WT7x26.5) bolted to the frames, as the intermediate piece between the plate and the boundary frame needed to achieve the goal of movability. The flanges of the WTs were bolted to the flanges of the columns and beams using 29 mm (1-1/8") A490 bolts at 305 mm (12") on center. Bolts were designed to be slip-critical under the maximum actuator load with a safety factor of 2.0. Flat infill plates were then attached to the web of the WTs using either epoxy or welding as mentioned above. The intent of the design was that the WT and plate assembly could be constructed in the shop and bolted on site to the surrounding frame and possibly also moved to a different location at a later time if desired (of course special precautions would have to be taken to insure the stability of the assembly while moving it). An overall schematic of specimens F1 and F2 is shown in figure 4-8.

From ancillary testing of various mock-up connections, it was established that a minimum overlap of 108 mm (4 1/4") of the infill plate over the web of the WTs was necessary for the epoxy to develop the yield strength of the infill plate of specimen F1.   The weld used to connect the plate to the WTs in specimen F2 was a 6 mm (1/4") fillet weld done using a MIG welder. To ensure that a high quality weld was obtained, the frame was laid down on four steel saw-horses so that a down-hand welding position (as shown schematically in figure 4-9) could be achieved. In a field setting a down-hand welding position may not be possible, but using welders certified in over-hand positions coupled with proper inspection would ensure a quality weld . Due to the thickness of the plate material, the strength of the weld itself was not a concern.

WT 180 x 39.5 (7 x 26.5) 29 mm (1-1/8") Dia.
Bolts 305 mm (12" o.c.) Both Sides (TYP)

Epoxy Plate to WT (Specimen F1)
5 mm (3/16") Fillet Weld Plate to WT (Specimen F2)

20 Gauge Flat Plate
t = 0.9 mm (0.0358") Spec. F1
t = 1.0 mm (0.0385") Spec. F2

W 460 x 128 (18 x 86)

W 310 x 143 (12 x 96)

W 310 x 143 (12 x 96)

1828.8 mm

108 mm (4.25") Spec F1
51 mm (2") Spec F2

W 460 x 128 (18 x 86)

3657.6 mm
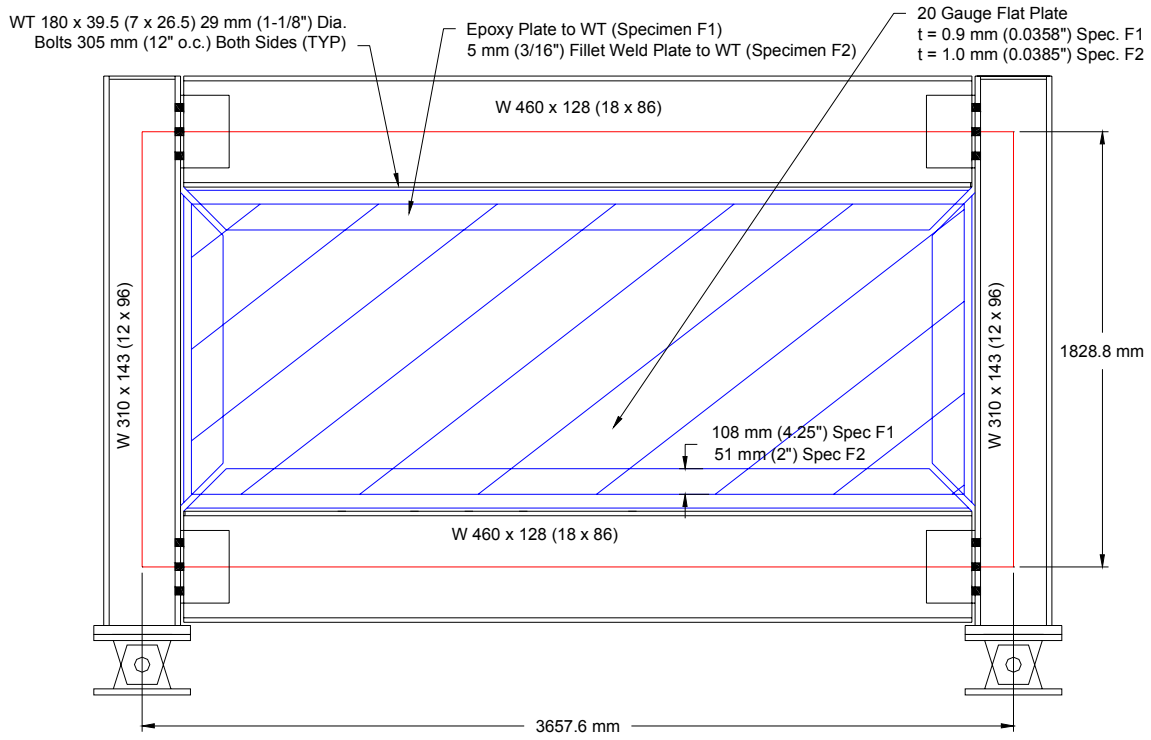
FIGURE 4-8 Schematics of Specimen F1 and F2

Down Hand
Weld Postition

Beam
or
Column

Infill
Plate

Intermediate
WT
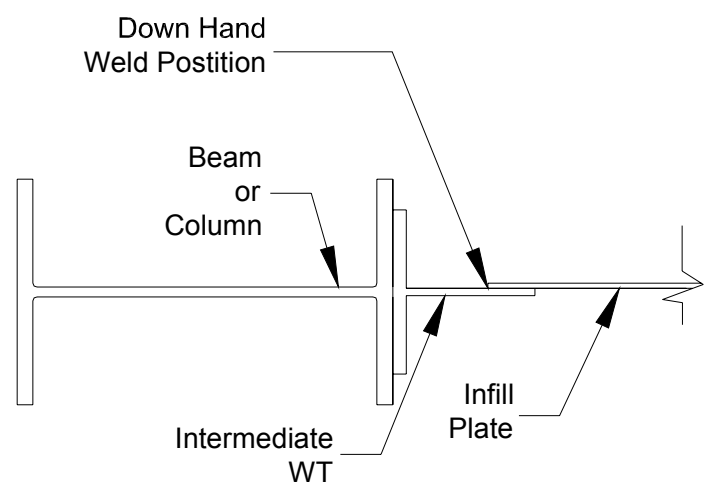
FIGURE 4-9 Welding Procedure for Specimen F2

53

4.2.8.2 Corrugated Infill Plate Specimen (C1)

Connecting the corrugated infill plate to the boundary frame was found to be more difficult than the flat plates. Figure 4-10 shows the corrugation profile of the chosen infill material, which was Type B steel deck produced by United Steel Deck, Inc. To further complicate the connection, the plate was to be installed with the corrugations oriented at 45° with the horizontal (as shown in figure 4-11, which is an overall schematic of specimen C1). This was done to orient the corrugations parallel to the tension field, assumed to form at 45°, and to delay the onset of buckling when the corrugations are in compression (as this was thought to be a possible advantage of this type of infill). Several options for the connection were considered; some were tested in ancillary tests on the universal testing machine (UTM) and some were ruled out as they were deemed to be too complicated or expensive to fabricate. A brief description of some of the connections considered follows, along with the reasoning for using or not using them.

First a WT connection similar to that used in the flat plate specimens was considered. However, because the corrugated plate would only be connected over a small portion of the corrugation's wavelength (connecting only to one face of the plate), the failure mode of net section fracture was shown to be unavoidable for both welded and epoxied options.
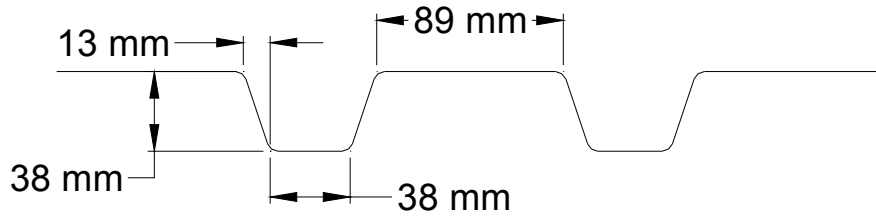
FIGURE 4-10 Corrugation Profile for Type B Steel Deck
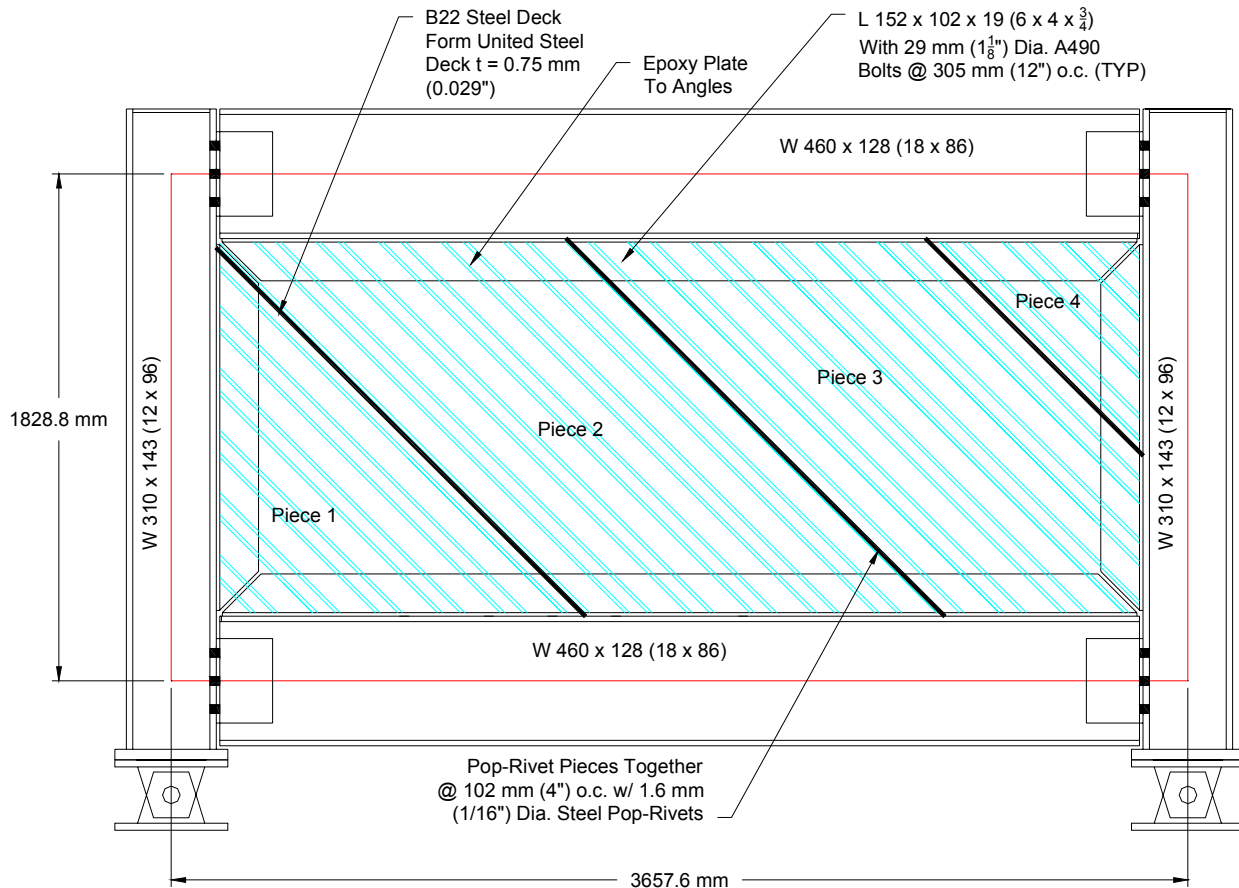
FIGURE 4-11 Schematic of Specimen C1

Next, a connection using a 13 mm (1/2") thick plate cut to follow the shape of the corrugated plate was considered and is shown in figures 4-12 and 4-13. The corrugated plate was to be cut for about 50 mm (2") along each of the cold formed bend lines that give it the corrugated shape. This would create tabs, as shown in figure 4-12, that could be bent and sat flat on the beam or column flange. The 13 mm (1/2") plate could be mounted on top of the tabs and bolted down with high strength bolts (figure 4-13). Friction between the tabs of the corrugated plate and the beam or column flange, and between the tabs and the 13 mm (1/2") plate would hold the

corrugated plate in place. A small mock-up of this connection was tested on the UTM but failed due to crack propagation from the locations where the corrugated plate had been cut.
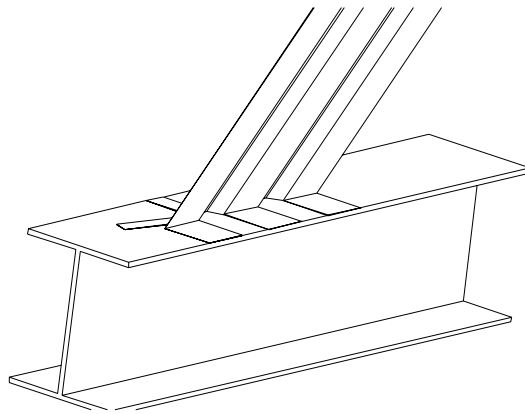
FIGURE 4-12 Specimen C1 - Tabs

Cut From Infill and Sat Flat On Beam

The third option considered consisted of mounting the corrugated plate inside a channel of the same depth as the depth of the corrugation (as shown in figure 4-14). The corrugated plate could be epoxied or welded to the inside of the channel's flanges and the channel could be bolted to the beams and columns, satisfying the movability requirement. This connection option was ruled out because standard channels have tapered flanges which would prevent the corrugated plate from being adequately positioned between them. However, this concept led to the connection that was ultimately chosen.
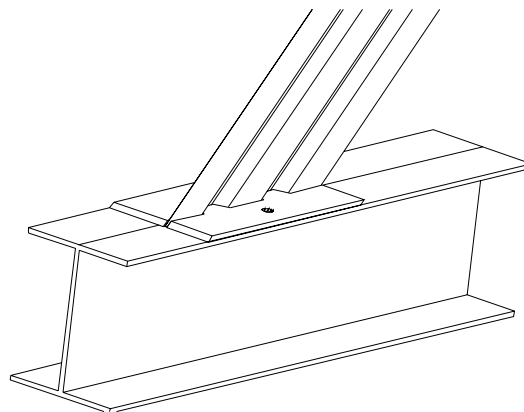
FIGURE 4-13 Plate Cut to

Corrugation Profile, Placed Over

Tabs and Bolted
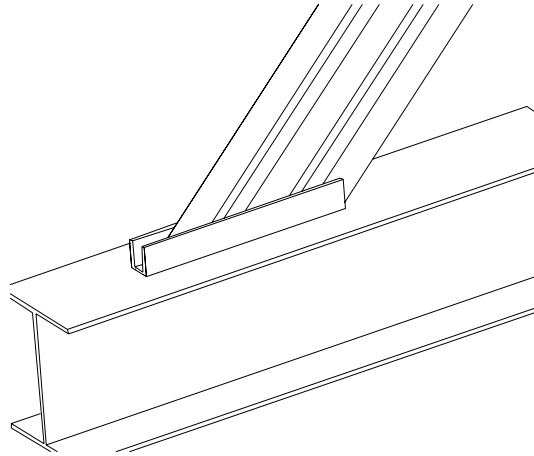
FIGURE 4-14 Corrugated Infill

Placed Between Flanges of Channel

Finally, a connection in which the corrugated plate would be "sandwiched" between two angles that would be bolted to the boundary frame was considered. The final detail of this connection is shown in figure 4-15. Epoxy was determined to be the best way to connect the plate to the angles. A total of 64 (10 on each column and 22 on each beam) 29 mm (1-1/8") diameter A490 bolts at 305 mm (12") on center, designed to be slip-critical under the maximum actuator load with a safety factor of 2.0, were chosen to connect the angles to the boundary frame. Ancillary tests were performed on the UTM using one wavelength of corrugation and Hysol 9460 epoxy. The test showed that this connection was able to yield the corrugated plate prior to any type of connection failure and was therefore retained for the design of specimen C1.
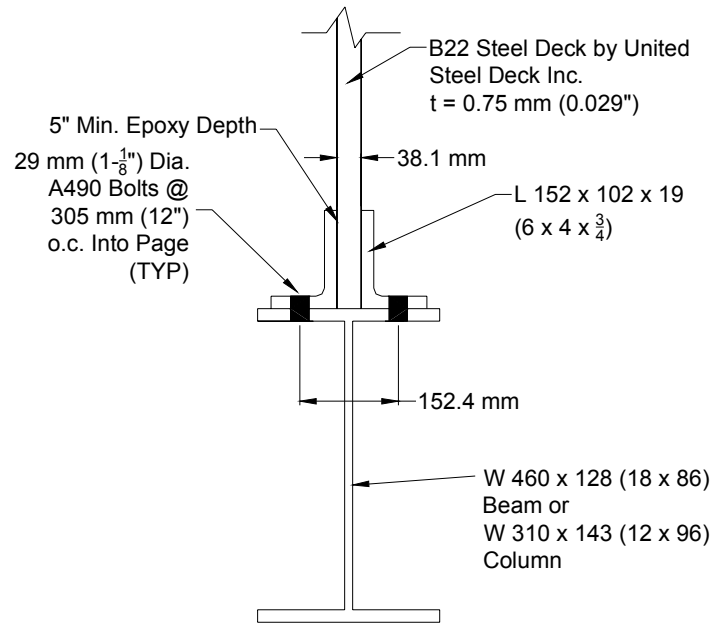
FIGURE 4-15

Infill Connection Schematic for Specimen C1

4.2.8.3 Epoxy Selection

Several different epoxies were considered and tested in the UTM. The setup for these ancillary tests involved attaching a piece of the infill plate material (see Section 4.4.1) to a piece of thicker ASTM A572 Gr. 50 steel with the particular epoxy being tested. The necessary surface area of epoxy was calculated from the epoxy manufacturer's published lap shear strength, with a factor of safety of 2. Surface preparation consisted of sanding both surfaces and then cleaning them with rubbing alcohol. A particular epoxy was deemed to have adequate strength if the plate material yielded prior to the epoxy failing in shear. Hysol 9460, manufactured by the Dexter Corporation and distributed by Wolcott Park Inc., was chosen because it was found to have adequate shear strength and for the following practical reasons:

- Working time of the epoxy was over 30 minutes, which was deemed necessary for the anticipated assembly time.
- Consistency was that of a thick paste, which made for easy application in any position.
- The mix ratio was 1:1 (it is a two-part epoxy), which kept fabrication simple.
- Minimal surface preparation was adequate, which helped simplify assembly.

4.2.9 Special Considerations for Specimen C1

Due to the maximum available steel deck width of 910 mm (3 feet), it was necessary to fabricate the infill plate for specimen C1 in four separate pieces. Three of the four pieces were the maximum 915 mm wide, but of variable lengths due to the 45 degree orientation of the plate, whereas the forth piece was sized to fill the remaining portion of the boundary frame. The four separate plate pieces are shown in figure 4-11. Following the installation of the pieces in the boundary frame and after allowing the epoxy connection to cure, the separate pieces were fastened together using 1.6 mm (1/16") diameter steel pop-rivets, installed with a pop-rivet gun, at a spacing of 4 inches on-center. An example of the riveted connections of separate pieces of infill is shown in figure 4-16.
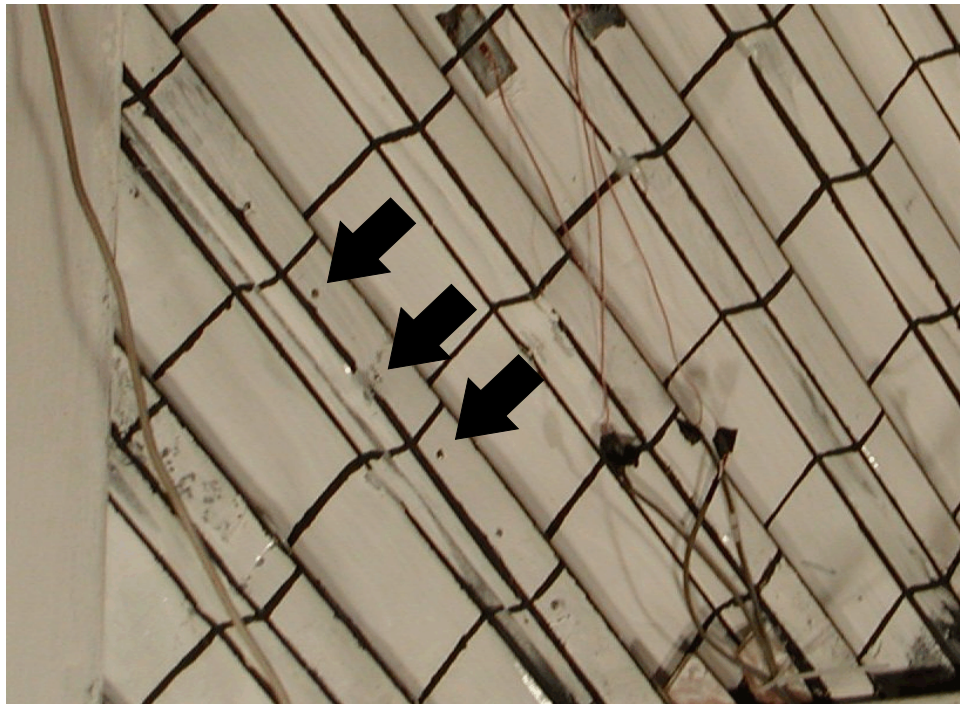
FIGURE 4-16 Photo of Pop-Rivet Connection for Specimen C1

4.3   Design of the Foundation Beam and Clevises

Anticipated support reactions from the three light-gauge steel plate shear wall specimen were found to be too large to be supported by the existing reinforced concrete foundation beam used for quasi-static testing in the SEESL. Additionally, the existing mountings on the foundation beam were not at the proper locations for the desired specimen dimensions and could not be easily moved. This warranted the design of a new foundation beam made from a steel wide flange section, with the added benefit that it could more easily accommodate different specimen dimensions in the future. It was also found that the available steel clevises in the SEESL were inadequate to support the anticipated loads, so new clevises were also designed.

4.3.1   Design Loads

The new foundation beam and clevises were meant to become permanent parts of the available equipment in the SEESL. In anticipation of future possible loading scenarios, after consultation with other researchers who had conducted quasi-static testing in the SEESL, it was found that the support reactions of the light-gauge SPSW specimens were the largest anticipated. For further conservatism it was deemed appropriate to design the foundation beam and clevises for 2.0 times the maximum support reactions for these specimens assuming the loading actuator was developing its full capacity. This meant that each clevis would be designed for a horizontal force of ±1110 kN (250 kips) acting simultaneously to a vertical force of ±1110 kN (250 kips). The foundation beam would then be designed for these loads at the two mounting locations for the light-gauge SPSW specimens.

4.3.2   Foundation Beam Configuration

The foundation beam was secured to the 460 mm (18") thick reinforced concrete strong floor of the SEESL using 8 prestressed, 29 mm (1-1/8") diameter Diwi-Dag bars. The resulting friction between the floor and beam in the maximum uplift condition was deemed insufficient to resist horizontal sliding. Therefore, the foundation beam was also connected to the bottom of the column of the existing reaction frame (on which the actuator is mounted) to create a closed, self-reacting frame (see figure 4-3).

Design loads described above dictated the use of a W360x314 (W14x211) section to provide sufficient flexural strength and stiffness. Additionally, 13 mm (1/2") stiffeners were used at the loading points and strong floor tie-down locations. The beam was designed in two pieces, 1892 mm (74.5"), and 7991 mm (314-5/8") long, each with butt-welded end-plates so that they could be bolted together. All specimen mounting and strong floor tie-down locations are on the longer segment, while the shorter section serves as the link to the column of the reaction frame. The splice between the two beam sections and the connection to the reaction frame were designed for 2.5 times the maximum actuator force. Figures 4-17 and 4-18 show the entire foundation beam with all loading points, strong floor tie-down points, and the bottom of the reaction frame column. Details for the connection to the reaction frame and for the splice in the foundation beam are shown in figures 4-19 and4-20 respectively.

4.3.3   Clevises

Following the assessment that the existing clevises in the SEESL would be insufficient for the anticipated loads, a new design was undertaken. The loads reported above were used and the resulting clevis design is shown in figure 4-21.
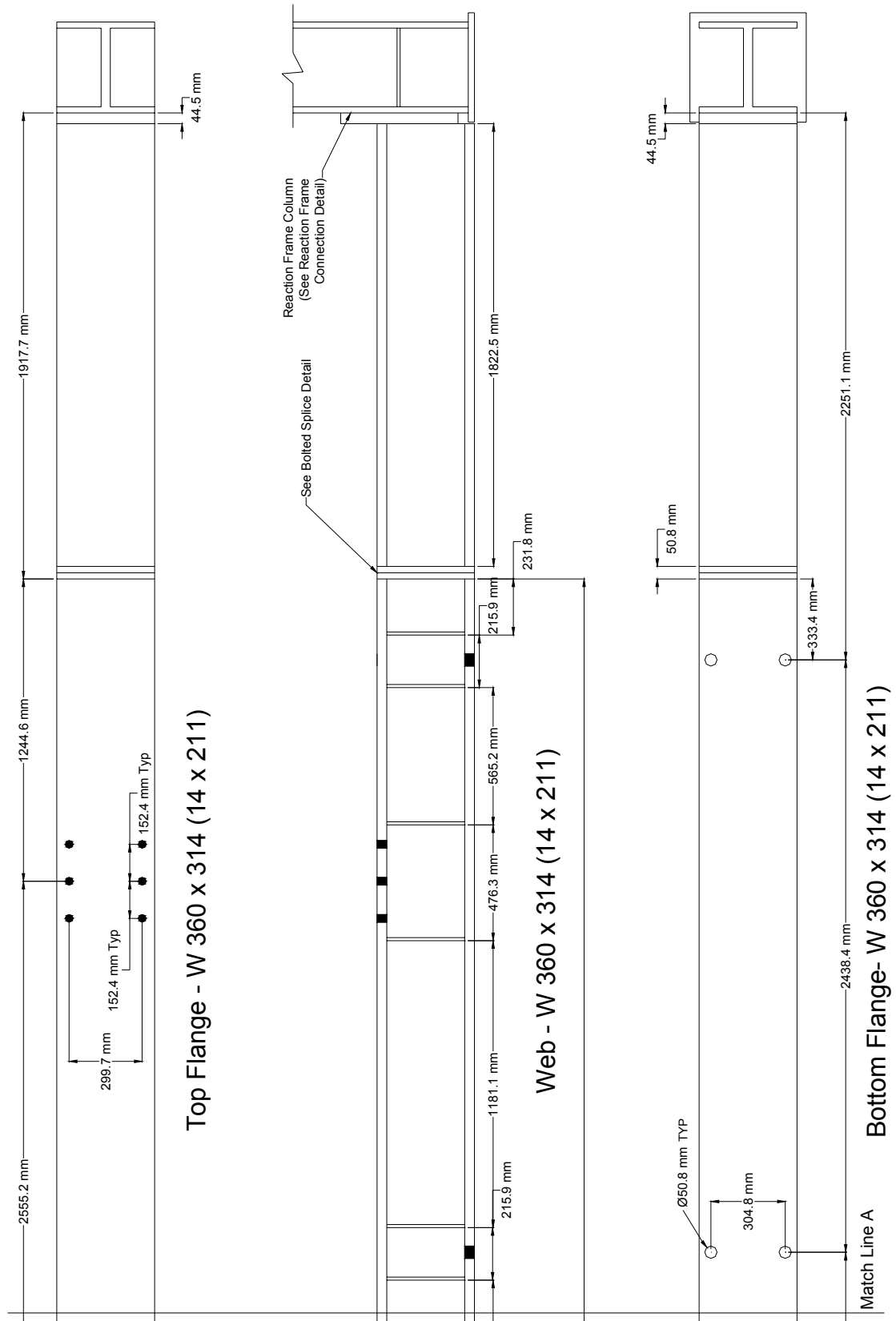
FIGURE 4-17 South Section of Foundation Beam
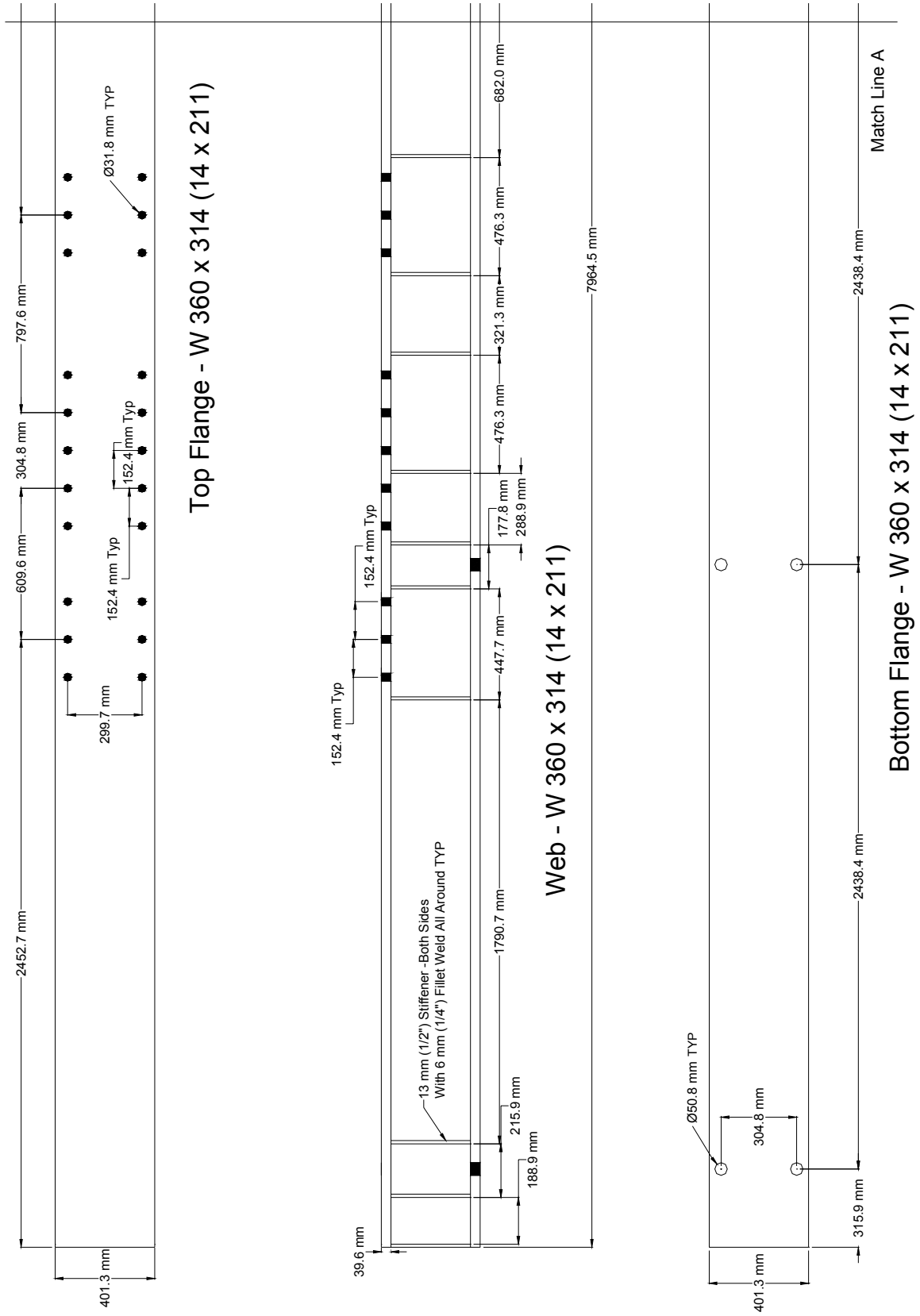
FIGURE 4-18 North Section of Foundation Beam

63
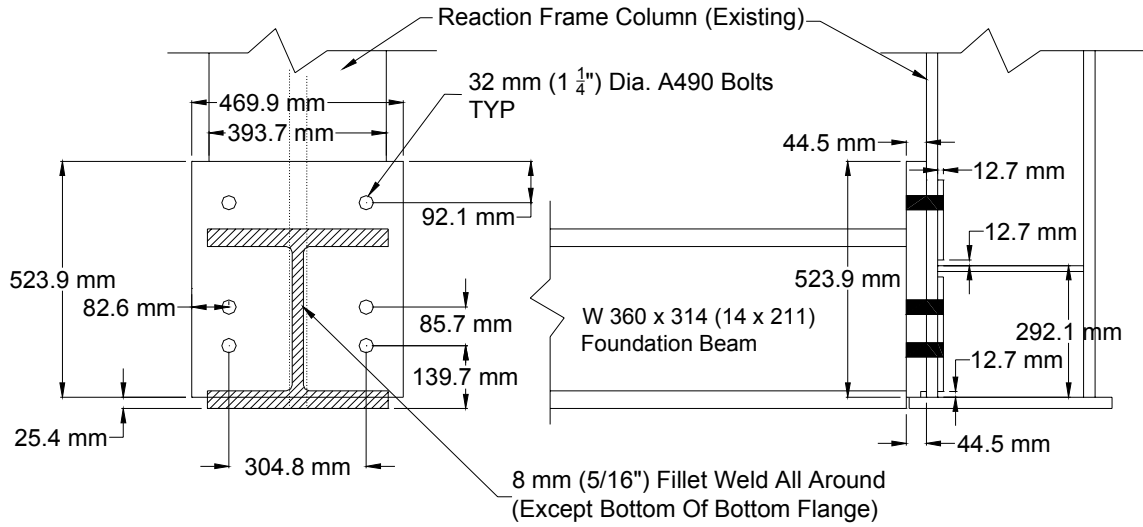
FIGURE 4-19 Schematic of Foundation Beam to Reaction Frame
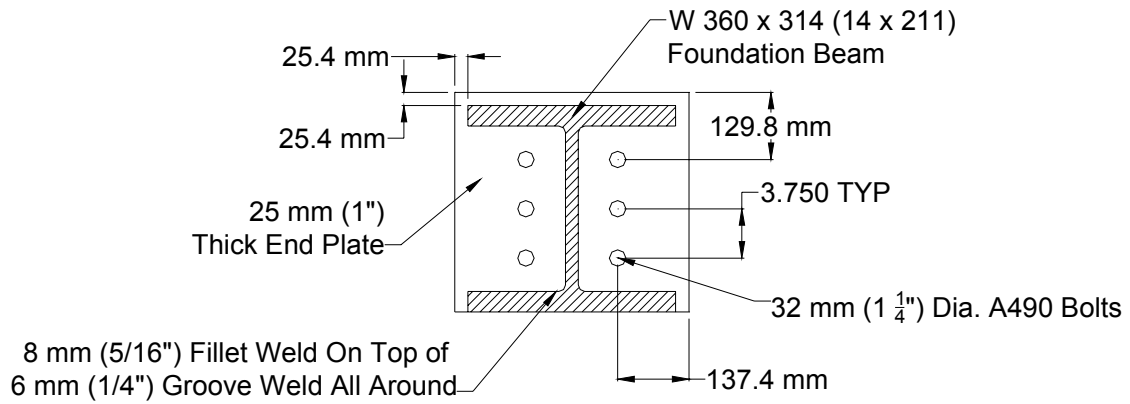
FIGURE 4-20 Foundation Beam Splice Schematic
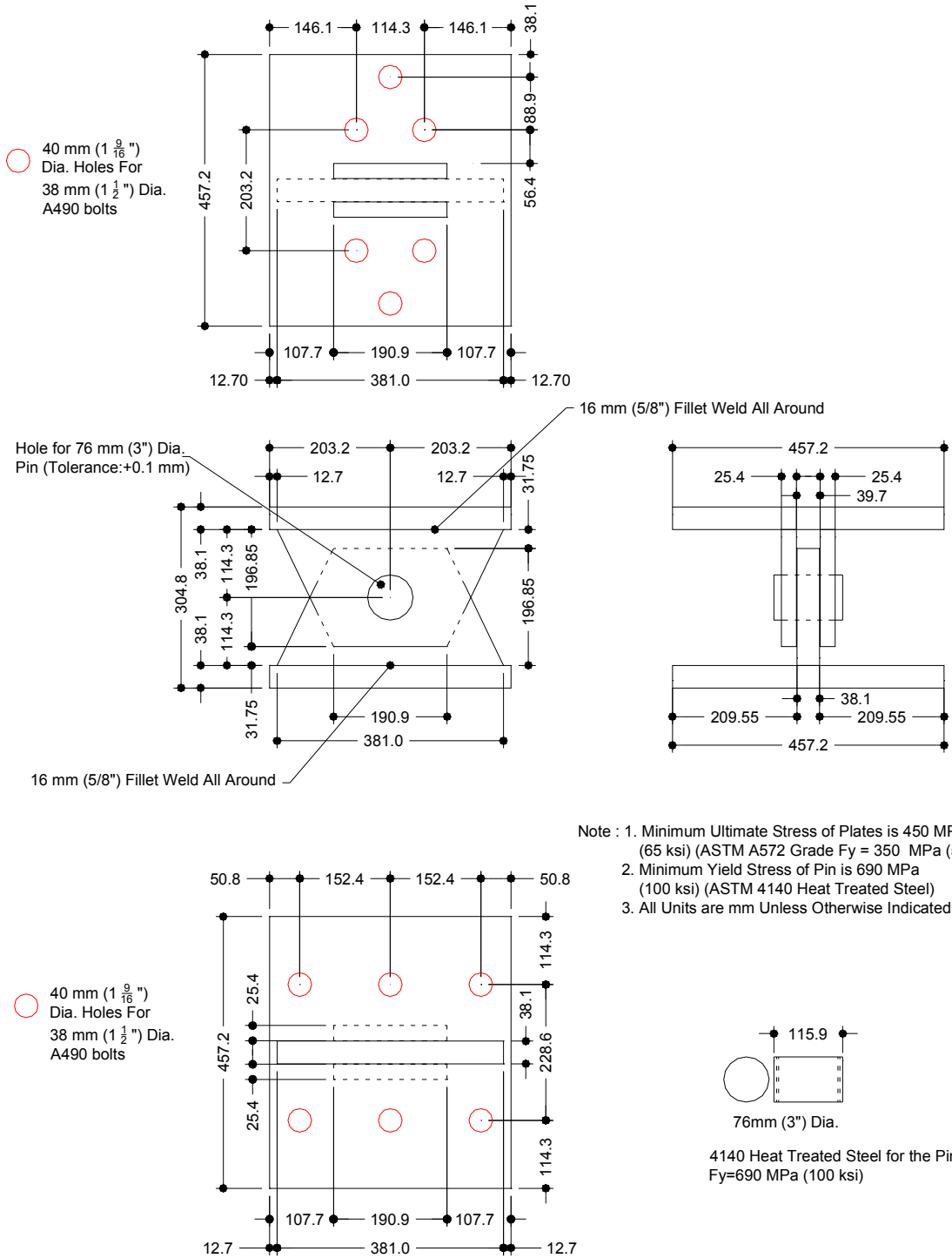
FIGURE 4-21 Clevis Schematic

Note : 1. Minimum Ultimate Stress of Plates is 450 MPa
(65 ksi) (ASTM A572 Grade Fy = 350 MPa (50 ksi))
2. Minimum Yield Stress of Pin is 690 MPa
(100 ksi) (ASTM 4140 Heat Treated Steel)
3. All Units are mm Unless Otherwise Indicated

4.4   Materials

4.4.1   Steel

Steel for the boundary frame members, beam-to-column connections, column base plates, and infill connections to the boundary frame was specified to be ASTM A572 Gr. 50. Due to the need to re-use the boundary frames for additional testing, coupon tests of the frame material were not performed. However, as discussed in Section 5, bare frame tests were carried out to characterize the behavior of the boundary frame alone.

The steel used as the infill for specimens F1 and F2 were specified to be the same with the exception that the plate for specimen F1 was galvanized. Both were ASTM A1008 (formerly A366) which is a cold-rolled, carbon, commercial steel sheet with no mandatory mechanical properties. ASTM states that typical mechanical properties are yield strengths between 20 and 40 ksi and elongations at fracture of 20% in 50 mm (ASTM, 1997) . This steel was selected because of the difficulty in finding any structural quality steel at the desired thicknesses. Several coupon tests were performed on both the infills for specimens F1 and F2 and mean results are shown in figures 4-22 and 4-23. The measured thicknesses of the plates were 0.91 mm (0.0358") and 0.98 mm (0.0385") for specimens F1 and F2, respectively.

Specimen C1 used Type B steel deck produced by United Steel Deck, Inc. as the infill material. This material conformed to ASTM A653 Grade 33 (ASTM, 1998), which is a galvanized material with a minimum yield stress of 230MPa (33 ksi) and a minimum elongation at fracture of 20% in 50 mm (2"). The measured thickness of the material was 0.75 mm (0.029") and mean coupon test results are shown in figure 4-24.
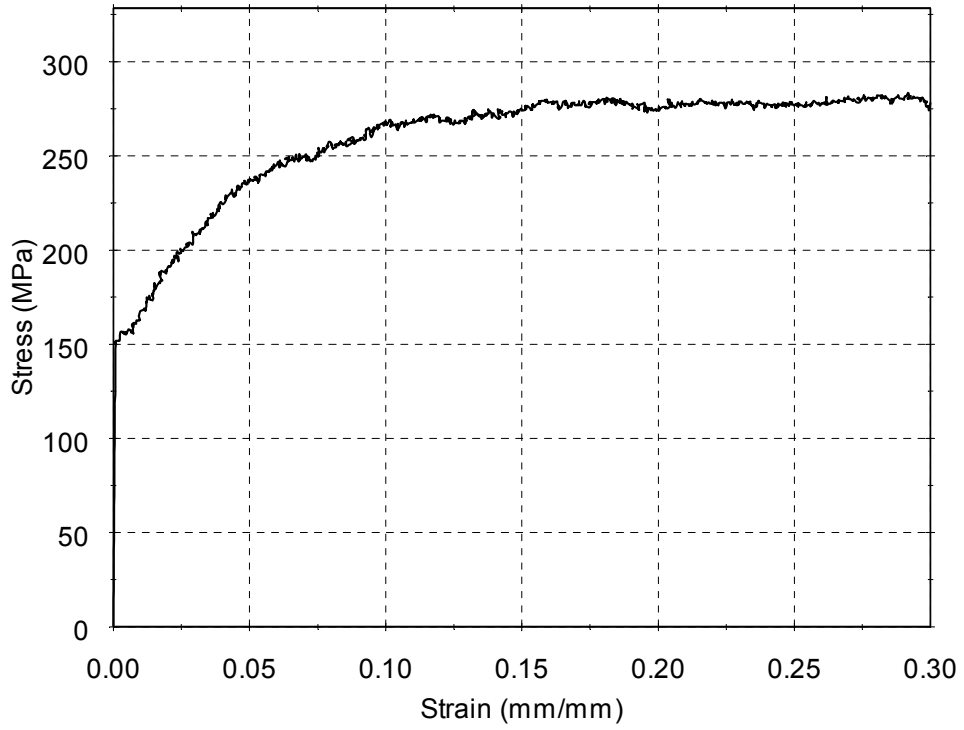
FIGURE 4-22 Stress-Strain Curve for Specimen F1
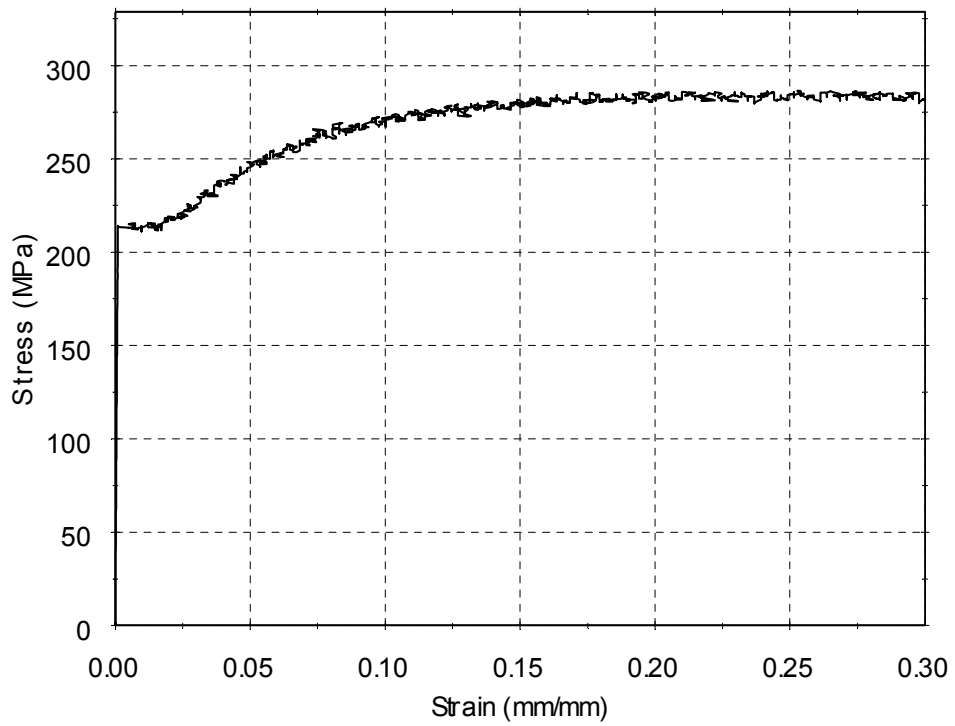
FIGURE 4-23 Stress-Strain Curve for Specimen F2
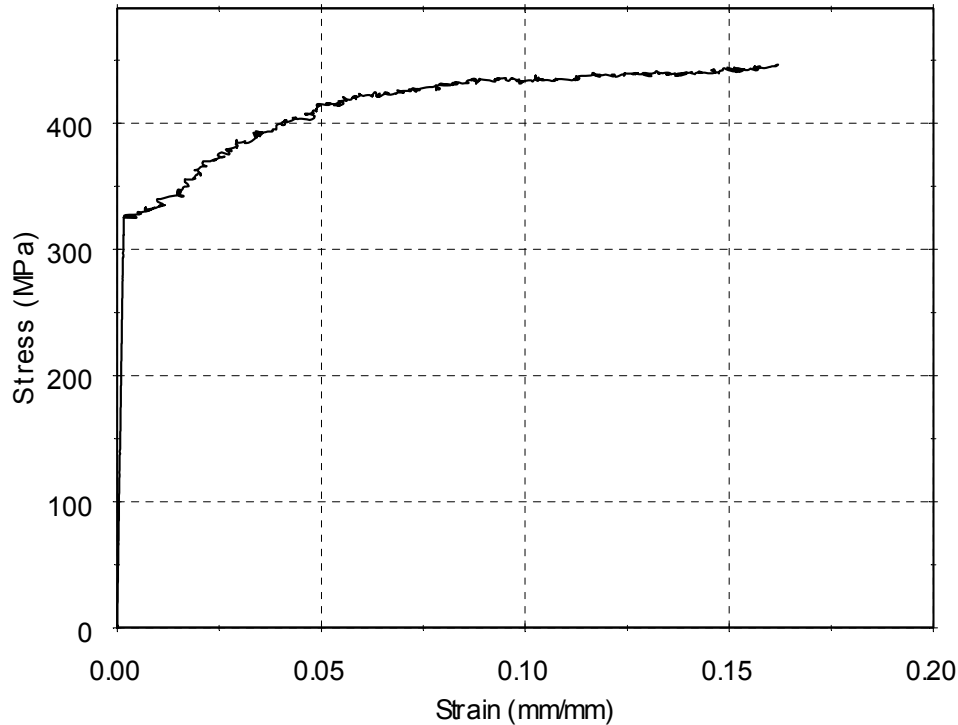
FIGURE 4-24 Stress-Strain Curve for Specimen C1

4.4.2 Epoxy

Epoxies in general are sensitive to the surface preparation of the materials being bonded, the environment in which it is applied, and the environment in which it is loaded. Through numerous ancillary tests, the lap shear strength of the Hysol 9460 was determined to be between 1 and 2 ksi and the elastic and shear moduli were taken as specified by the manufacturer. As stated in Section 4.2.8.3 this particular epoxy was chosen for several reasons, but most importantly it could develop the yield strength of the infill plate materials using a reasonable surface area of overlap.

All bonding surfaces were prepared by grinding off any mill scale, then sanding with a coarse pad to roughen the surfaces, and cleaning thoroughly with rubbing alcohol. Epoxy application for specimen F1 was done in about 15 minutes. Only the WTs that were bolted to the boundary frame received epoxy, which was spread on using plastic trowels (the consequences of applying the epoxy to only the WTs is discussed in Section 5). After spreading the epoxy, the plate was put in place and lead bricks were used to apply pressure for 8 days. Note that the frame was laid down horizontally for this purpose which did not necessarily simulate field conditions. However,

the authors feel that in a field application there are a number of creative ways in which a contractor could apply pressure to the epoxy in an upright position, including, using air bags, large magnets, or drilling holes through the intermediate connection pieces and infill in the connection region and inserting fasteners.

Each face of the infill plate of specimen C1 was epoxied separately (i.e. in two separate stages). In this case, both the infill plate and the angles, which were bolted to the boundary frame, were coated with epoxy. After one face of the plate was bonded to the angles on that side, wooden wedges were hammered between the plate and the angles which had not just received epoxy. This was done to insure that a uniform pressure was applied to the bonded surfaces. Application of the epoxy to the other face of the infill was done similarly after epoxy on the first face was allowed to cure for 8 days.

4.5   Test Setup

Figures 4-25, 4-26, and 4-27, respectively, show specimens F1, C1, and F2 prior to testing. Some detail of the test setup can be seen in these figures.

4.5.1   Mounting of Specimen

Testing was performed in the SEESL at the University at Buffalo. The foundation beam was connected to the large quasi-static reaction frame and strong floor as described in Section 4.3.2. Each specimen was mounted on the clevises which were themselves mounted on the foundation beam. Six 38 mm (1-1/2") diameter A490 bolts were used to attach each column base plate to the corresponding clevis, and then to attach each clevis to the foundation beam. All bolts (the bolts on the specimen themselves as well as bolts used to connect the two sections of the foundation beam together and the foundation beam to the reaction frame) were tightened to their specified internal tension using the "turn-of-the-nut" method described in the AISC LRFD manual (AISC, 1998). To achieve the torque required to reach the specified nut rotations, a HYTORC Blitz 4-A hydraulic torque wrench was used.
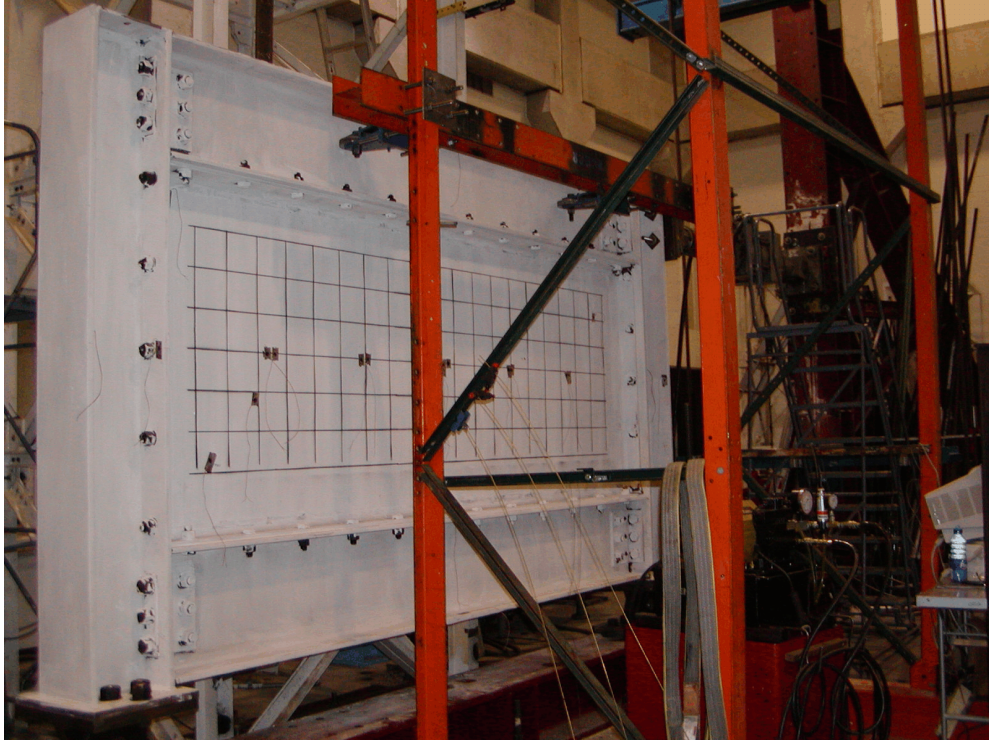
FIGURE 4-25 Specimen F1 Prior to Testing

FIGURE 4-26 Specimen C1 Prior to Testing
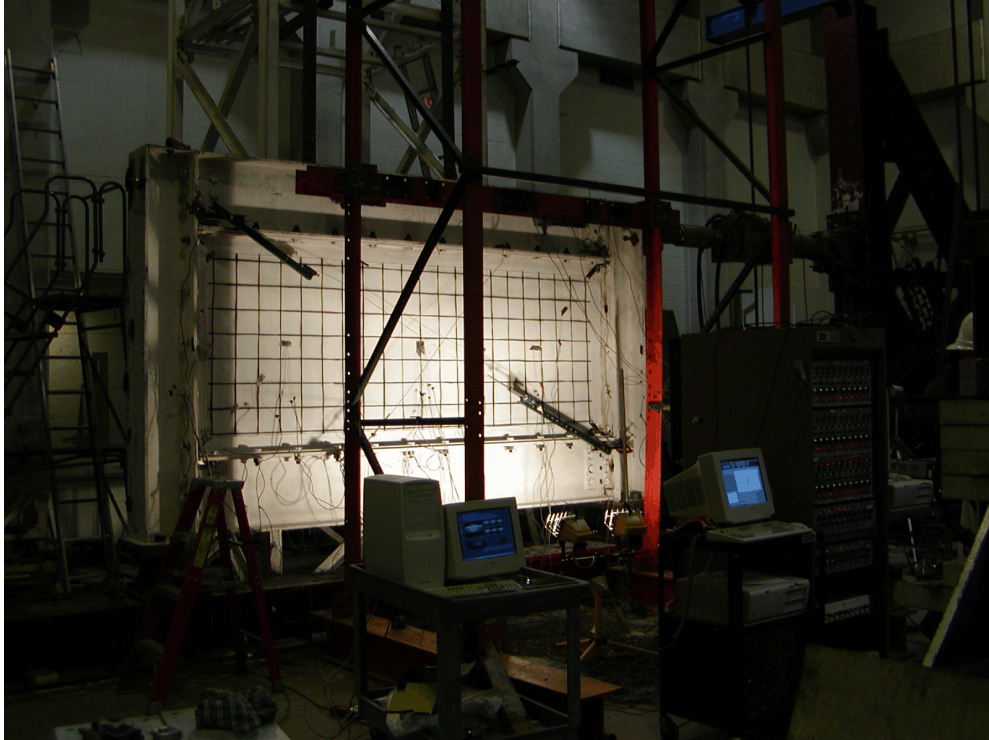
FIGURE 4-27 Specimen F2 Prior to Testing

4.5.2   Actuator Mounting

The Miller servo-controlled static rated actuator with a load capacity of 1110 kN (250 kip) and an available stroke of 200 mm (8") was mounted to the reaction frame using four 25 mm (1") diameter high strength threaded rods. Four similar rods were used to connect the actuator to the test specimen. The actuator is equipped with swivels at each end and end-plates with threaded holes to accept the rods. The reaction frame, actuator, specimen, clevises, and foundation beam were shown previously in figure 4-3.

4.5.3   Lateral Bracing

Lateral bracing was provided to the specimen through the use of large rollers (figure 4-28) cantilevering from frames mounted on the east and west side of the specimen and set to roll along the upper third of the web of the specimen's top beam. A gap of approximately 3 mm (1/8") was left between the beam web and each roller so that the roller would only be engaged if the out-of-plane deflection closed that gap. The frames supporting the rollers on each side of the specimen

71
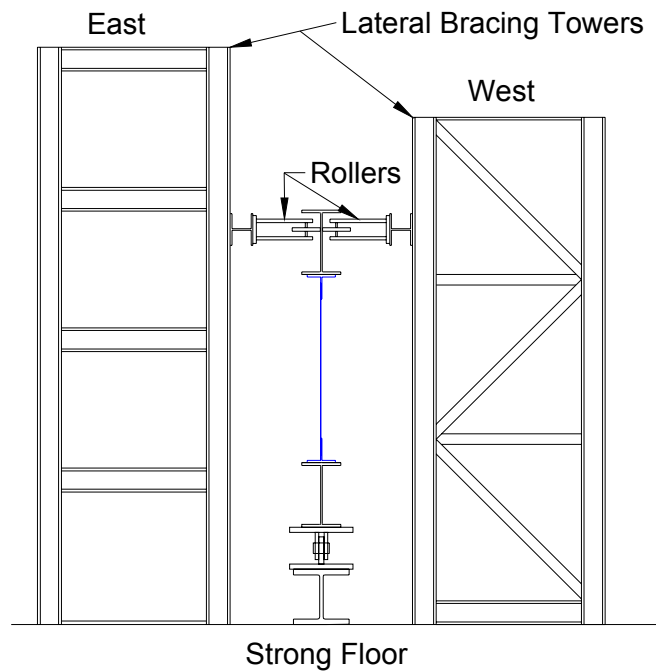
FIGURE 4-28 Lateral Bracing

were secured to the strong floor using high strength threaded rods. Large out-of-plane forces were not expected but lateral bracing was provided for safety reasons.

4.6 Instrumentation

4.6.1 Strain Gauges

All specimens were instrumented with CEA-06-125UW-120 strain gauges manufactured by Vishay Measurements Group Incorporated. The strain gauge layout for specimens F1 and F2 were identical and are shown in figures 4-29 and 4-30 for the west and east faces of the tested walls, respectively. Four gauges were placed at the midpoint of each beam and column of the boundary frame to monitor the moments and axial forces there.

Gauges on the flat infill plates were primarily oriented at 45° from the horizontal (the anticipated orientation of the tension field), except at the center of the infill on each face where one horizontal and one vertical gauge were also added. There were five major clusters of gauges at mid-height on each face of the flat infill plates. The first cluster was at the centerline, the second and third were 560 mm (22") to the north and south of the centerline and the fourth and fifth

72

clusters were 560 mm (22") further north and south from them. This was done so that any variation in the magnitude of the tension field strains across the infill plate could be recorded. Gauges PW1 on the west face (figure 4-29) and PE1 on the east face (figure 4-30) were placed at 305 mm (12") (measured at 45° from horizontal) from the corner of the infill plate. Gauges PW2 and PE2 were placed 305 mm (12") (measured at 45° from horizontal) from PW1 and PE1 respectively. The purpose of these four gauges was to identify any variation in the magnitude of the tension field strains along a path 45° from horizontal. Specimens F1 and F2 each had 47 strain gauges in total.

Specimen C1 had a different strain gauge layout than specimens F1 and F2 because tension field action was only expected in the direction parallel to the corrugations. However, the strain gauges on the beams and columns of the boundary frame were in the same locations as for specimens F1 and F2. The strain gauge layout for specimen C1 is shown in figures 4-31 and 4-32 for the west and east faces of the wall respectively. There were five major clusters of gauges at mid-height on each face (for the same reason five clusters were used on specimens F1 and F2) with the same general spacing as on specimens F1 and F2. In the center cluster of gauges on each face of the infill there were gauges placed on each section of the corrugation to determine if the strain was uniform across an entire wavelength of corrugation. In the other clusters, the gauges were on the 38 mm (1-1/2") crest and 89 mm (3-1/2") trough of the corrugations (these are the parts of the corrugation which were epoxied to the boundary frame). There was a total of 47 strain gauges on specimen C1.

4.6.2 Temposonics

The layout of the Temposonic Magnetic Strictive Transducers (Temposonics) was the same for all three specimen and is shown in both figures 4-29 and 4-31. T1W was used as the control for the displacement during testing and T1E served as a backup in case T1W was not functioning properly. The most important measurement was determined to be the horizontal displacement of the frame, so TP1 was added to provide an additional instrument from which the horizontal displacement could be found. TP2 and TP3 were installed at 45° from the horizontal to measure the elongation of the infill plates in the direction of the tension field. T2, T3 and T4 were placed at the quarter points of the north column to measure any pull-in of that column by the yielding

infill plates. T6 was used to measure any movement of the north clevis with respect to the foundation beam.

4.6.3 Potentiometers

Six Displacement Potentiometers (DP) were placed in strategic locations to measure the vertical and horizontal displacement of the foundation beam under the south clevis, and to measure the opening and closing of the web-angle connections. The latter was achieved by placing a DP horizontally on top of the beam flange at each beam-to-column connection. The DP layout was the same for all specimens.
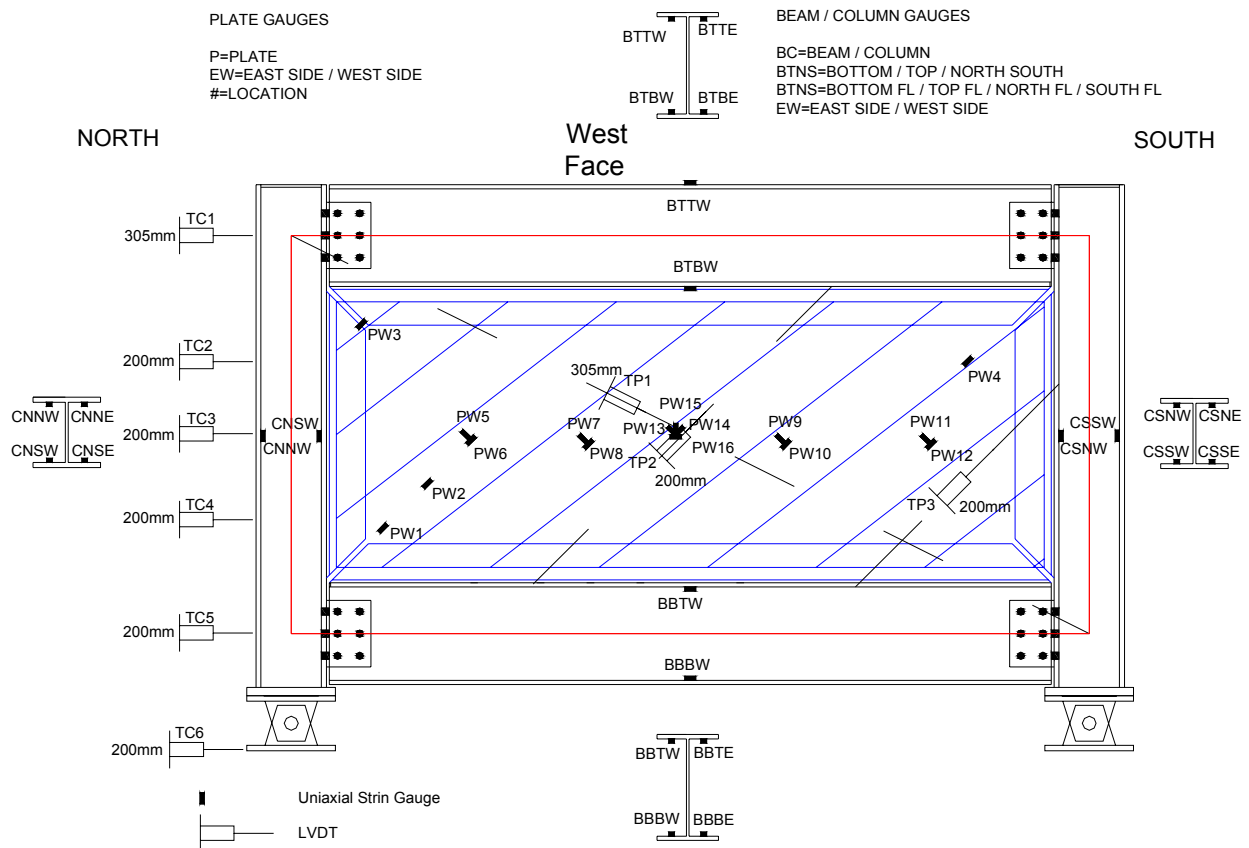
FIGURE 4-29 West Face Instrumentation for Specimen F1 and F2
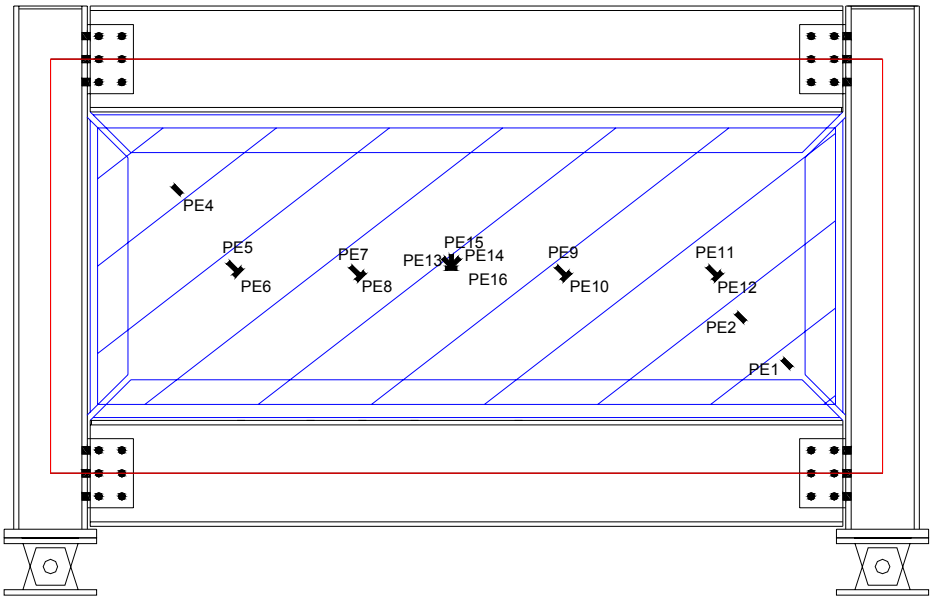
FIGURE 4-30 East Face Instrumentation for Specimen F1 and F2
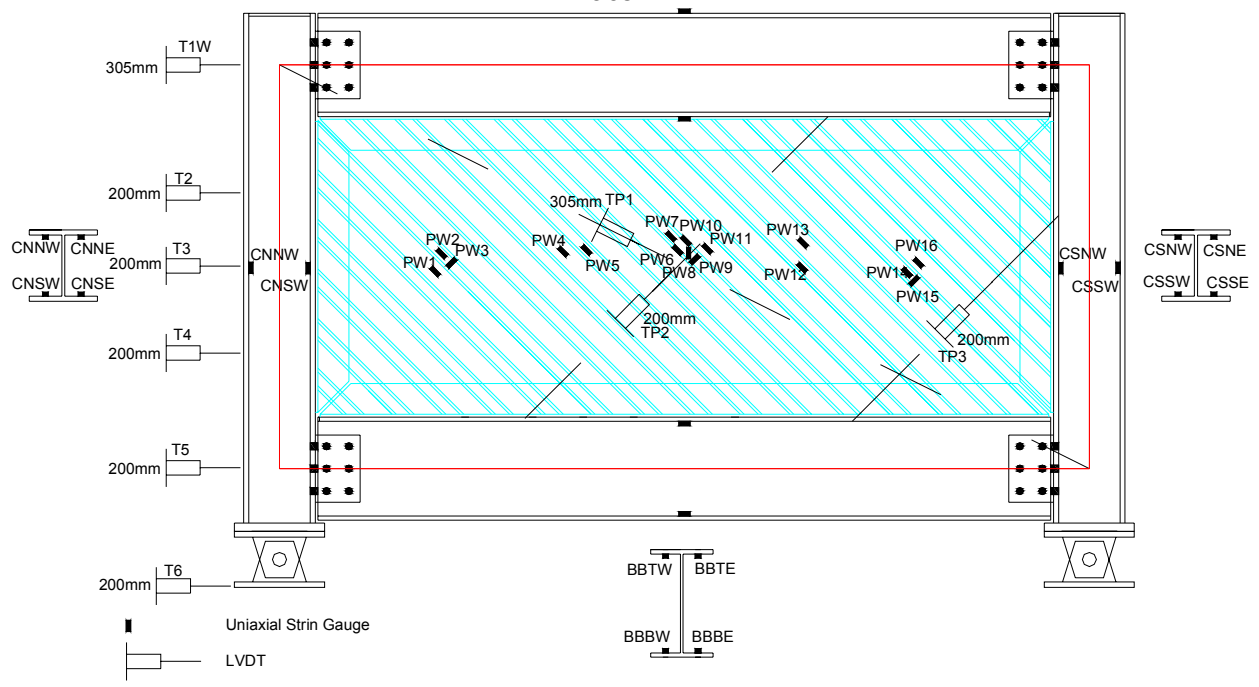
FIGURE 4-31 West Face Instrumentation for Specimen C1
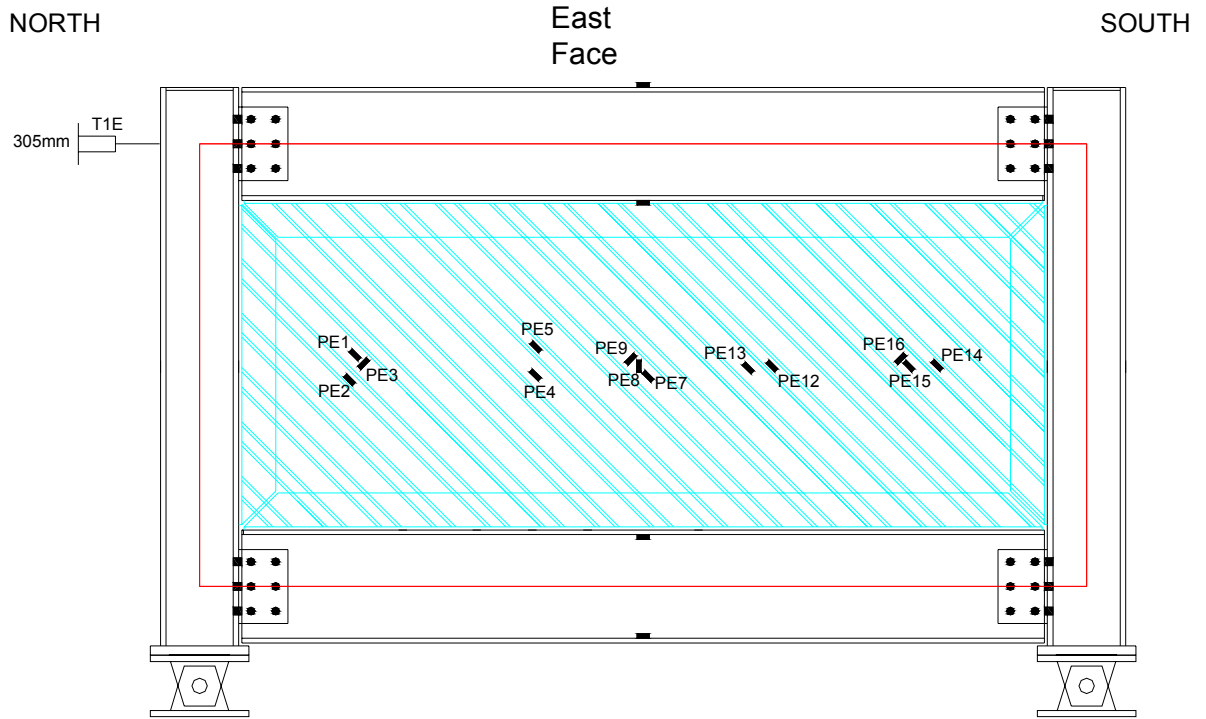
FIGURE 4-32 East Face Instrumentation for Specimen C1

SECTION 5

EXPERIMENTAL PROGRAM AND OBSERVATIONS

5.1   General

This section describes the loading programs and experimental observations for the three light-gauge steel plate shear wall specimens discussed in Section 4. Methods used to estimate the yield base shears and displacements prior to testing are discussed, along with the loading protocol used, and the recorded cyclic displacement histories. Following this discussion, the testing of each specimen is described in detail, and observations made during testing regarding the behavior of each specimen are given. Finally, the testing of the two boundary frames without infills is described.

5.2   Loading Program

Loading of the three light-gauge steel plate shear wall specimens consisted of quasi-static cycles using a mix of force control and displacement control. Only estimates of the yield base shear forces and displacements were available prior to testing and, typically, there is greater confidence in the predicted values for yield base shear than yield displacement. Therefore, cycles up to yield were performed using force control, then once the yield displacement had been identified experimentally, the subsequent cycles were done using displacement control.

5.2.1   Estimation of Yield Force and Displacement

For the purpose of estimating the yield base shears and yield displacements prior to testing, strip models of each specimen were developed for pushover analyses using SAP2000 (with actual material properties from the coupon tests discussed in Section 4), and assuming simple beam-to-column connections. For expediency, in practice, the strips are often modeled as spanning from

the center lines of the beams and columns. However, in this case, because of the scale of the specimens and the relatively large depths of the beams and columns, this would have led to strip lengths that were longer in the models than in the actual test specimens, resulting in an over-prediction of the yield displacements. To correct this, actual strip lengths were used to calculate displacements as described in Appendix A.

Experimentally obtained bare frame test results were then superimposed with the predicted pushover curves of the strip models for specimens C1 and F2 to obtain a prediction of the system behavior. This was necessary because the SAP2000 models used simple beam-to-column connections, whereas the actual connections were partial moment connections. Prior to testing specimen F1 no bare frame test results were available, therefore, they could not be included. The resulting pushover curves predicted for the three test specimens are shown in figure 5-1, to a maximum displacement of 25 mm. Further details of the procedure used to obtain the predicted pushover curves are given in Appendix A.

5.2.2   ATC Loading Protocol

Quasi-static cyclic testing was carried out in accordance with the ATC 24 loading protocol (ATC, 1992). This document specifies that specimens should be subjected to three cycles at each displacement step up to three times the yield displacement, after which only two cycles are necessary. The first displacement step should be 1/3 of the yield displacement, the second should be 2/3 of the yield displacement, the third should be the yield displacement (δ_y), and every step after should be increasing multiples of the yield displacement ($2\delta_y$, $3\delta_y$, etc.). This is shown graphically in figure 5-2.

5.2.3   Cyclic Displacement Histories

Since the yield forces and displacements, as described in Section 5.2.1, are estimated from numerical simulation, there is slight variation in what was observed and used during the experimental testing. Therefore, the actual displacement histories used for each specimen are given in tables 5-1, 5-2, and 5-3, and the hysteretic force versus drift loops obtained during the testing of specimens C1 and F2 are shown in figures 5-3, 5-4. In the history for specimen C1 there is a fourth displacement step prior to yield. This was due to specimen C1 not being as stiff

as predicted. Additionally, in the elastic range the displacement steps did not exactly equal 1/3 and 2/3 of the yield displacements for any specimen. However, there were still three cycles at each of at least two displacement steps of increasing amplitude prior to reaching the yield displacements.

TABLE 5-1 Cyclic Displacement History - Specimen F1

Displacement Step	Number of Cycles	Cumulative No. of Cycles	Displacement Δ/δ_y	Displacement (mm)	Drift (%)
1	3	3	0.25	1.3	0.07
2	3	6	0.4	2.0	0.11
3	1	7	1	5.1	0.25

TABLE 5-2 Cyclic Displacement History - Specimen C1

Displacement Step	Number of Cycles	Cumulative No. of Cycles	Displacement Δ/δ_y	Displacement (mm)	Drift (%)
1	3	3	0.17	1.4	0.08
2	3	6	0.42	3.4	0.19
3	3	9	0.70	5.7	0.31
4	3	12	1	8.1	0.44
5	3	15	2	16.5	0.90
6	3	18	3	25.0	1.38
7	1.5	19.5	4	33.5	1.83

TABLE 5-3 Cyclic Displacement History - Specimen C1

Displacement Step	Number of Cycles	Cumulative No. of Cycles	Displacement Δ/δ$_y$	Displacement (mm)	Drift (%)
1	3	3	0.25	1.3	0.07
2	3	6	0.64	3.4	0.19
3	3	9	1	5.3	0.29
4	3	12	2	10.7	0.58
5	3	15	3	16.5	0.90
6	2	17	4	22.1	1.21
7	2	19	5	28.0	1.53
8	2	21	6	33.3	1.82
9	2	23	7	39.0	2.13
10	2	25	8	44.6	2.44
11	2	27	10	56.2	3.07
12	4	31	12	67.0	3.65

5.3   Experimental Observations

This section describes, in detail, the experimental testing and observations of the three light-gauge steel plate shear wall specimens. Observations made regarding the performance of the specimens during regions of both linear and nonlinear behavior will be given. It should be noted that the displacements referred to in this section are relative displacements, i.e. the difference between Temposonics T1W and T5 of figures 4-29 and 4-31.

5.3.1   Specimen F1

During the first three cycles of loading (1.3 mm, 0.07% drift), specimen F1 exhibited completely linear behavior. At the onset of Cycle 1, audible buckling of the infill was observed (and continued for all cycles), and pinging sounds were heard coming from the epoxy connections. During the first half of Cycle 2, a crack in the epoxy near the top of the south column was observed and is shown in figure 5-5 (the 2 indicates the extent of the crack at this point which

was approximately 3"). No additional cracking in the epoxy was evident for the remaining cycles at this first displacement step.

During the first half of Cycle 4 several pinging sounds were heard, including a loud one at 1.5 mm of displacement. A new crack in the epoxy was noted at the upper beam on the north end of the frame and is shown in figure 5-6. Visible buckling of the infill was observed during all three of the cycles at 2.0 mm displacement (0.11% drift) as shown in figure 5-7.

In the first half of Cycle 7 loud snapping from the epoxy was heard. At the peak displacement (-4.6 mm, 0.25% drift) of this cycle, some minimal whitewash flaking was observed in the corners of the infill plate. During the second half of Cycle 7, the epoxy which connected the infill plate to the boundary frame failed across the entire length of the top beam connection while the specimen still exhibited mostly linear behavior. This concluded the testing of specimen F1.

After the infill had been removed from the frame a complete inspection of the epoxy left on the intermediate WT's and infill plate was performed. It was noted that complete epoxy coverage was not achieved, and large areas in which there was no epoxy on the WT's were visible, as shown by the circled regions in figure 5-8. This could be partially attributed to the epoxy being applied to the infill plate only, and not directly to the WT's. Qualitatively, this hypothesis was verified by the successful testing of specimen C1, in which epoxy was applied to both the infill plate and intermediate angles.

5.3.2   Specimen C1

To aid in the description of the observations made during the testing of specimen C1, figure 5-9 will be referred to frequently in this section. The lines marked 1, 2 and 3 in figure 5-9 are the lines along which severe local buckling was observed. Photos of the progression of the local buckling along these lines throughout the testing will be shown. Also shown in figure 5-9 are annotations that will be used to describe the approximate locations, cycle numbers, and type of additional damage to the infill, including infill fractures and epoxy cracks.

Specimen C1 exhibited linear behavior during the first three cycles, although its stiffness was less than predicted. Some popping noises were observed during the three cycles at the first displacement step (1.4 mm, 0.08% drift) but they seemed to have no effect on the specimen's behavior. During the three cycles at the second displacement step (3.4 mm, 0.19% drift) additional small pops were heard but the specimen was still exhibiting linear behavior. Local buckling began to occur during Cycle 7 and by the end of Cycle 9 had progressed to what is shown in figures 5-10, 5-11, and 5-12, for lines 1, 2, and 3 respectively. The specimen was still behaving linearly at this third displacement step (5.7 mm, 0.31% drift) with no stiffness degradation in the positive direction (note that tension field action only occurred in the positive displacement direction for specimen C1 due to the orientation of the corrugated profile of the infill).

Based on the extrapolation of the shape of the force-displacement hysteresis curve obtained at a displacement of 8.1 mm (0.44% drift) and load of 494 kN (reached during Cycle 10), and visually using an equal energy approach, this displacement was determined to be the experimentally obtained yield point. During the subsequent cycles at this displacement step, the local buckling observed previously along lines 1 and 2, grew to what is shown in figures 5-13 and 5-14, respectively. Residual buckles were visible at zero displacement during the three cycles at the yield displacement (8.1 mm) indicating that the infill had, in fact, yielded and elongated inelastically. Figure 5-15 shows an area of epoxy cracking found at the end of the three cycles at the yield displacement. There were 4 such cracks noticed at this point in the test (denoted E11 in figure 5-9), all in locations where the larger section of the corrugation was epoxied. Additionally, the epoxy cracks were all along the bottom beam (at the north and south corners respectively, and 300 and 900 mm south of the centerline of the wall). Figure 5-16 shows a failed pop-rivet at the end of Cycle 12, there were two such rivet failures at the end of the $\pm 1\delta_y$ cycles. There was no change in the maximum base shear obtained during the three cycles at $\pm 1\delta_y$, indicating that the infill was still in good condition. It should be noted that whitewash flaking (which is usually an indication of yielding) did not occur, probably because the infill panel was galvanized which may have created a better bond with the whitewash then that normally achieved with regular steel surfaces.

During the first excursion to $\pm 2\delta_y$ (16.5 mm, 0.9% drift) a loud pop from the epoxy was heard at a displacement of 15.2 mm but no immediate change in stiffness occurred. Subsequent cycles at this displacement step increased the amount of local buckling along lines 1 and 2 of figure 5-9, to that shown in figures 5-17, and 5-18. Figures 5-19 and 5-20 show more global views of the north and south halves of the infill panel, respectively, at $-2\delta_y$ during Cycle 15. The epoxy crack in figure 5-15 is shown again in figure 5-21 during Cycle 13 and is notably larger. At this point there were two additional epoxy cracks (denoted E13 in figure 5-9), again in locations where the larger section of the corrugation was epoxied to the bottom beam, 750 mm north and 600 mm south of the specimen's centerline. Figure 5-22 shows additional failed pop-rivets adjacent to the one shown previously in figure 5-16. Due to the loss of additional rivets in this region the two sections of infill are now visibly separating. At the end of Cycle 15 there was a total of 12 pop-rivets that had failed and there were two small fractures (not visible in pictures) in the infill plate at two of the failed rivet locations. The maximum base was 625 kN and occurred at $+2\delta_y$ of Cycle 13 (the first cycle at $\pm 2\delta_y$). Some strength degradation occurred during the three cycles at $\pm 2\delta_y$ and by Cycle 15 the maximum base shear was 580 kN, corresponding to a 7% drop from Cycle 13.

Following the three cycles at $\pm 2\delta_y$, specimen C1 was subjected to three cycles at $\pm 3\delta_y$ (25.0 mm, 1.38% drift). After the first excursion in the positive direction several fractures in the infill plate were noticed (denoted F1 in figure 5-9). These fractures were on the smaller sections of the corrugations along line 2 of figure 5-9, where repeated local buckling had occurred. These are shown in figures 5-23 and 5-24. Additional damage in this first excursion to $+3\delta_y$ included a large epoxy crack in the upper north corner of the specimen, which is shown in figure 5-25. This was the first epoxy crack connecting a smaller section of corrugation. Local buckling along lines 1, 2 and 3 during the first excursion to $-3\delta_y$, is shown in figures 5-26 (line 1) and 5-27 (lines 2 and 3). The maximum base shear in Cycle 16 was 600 kN (96% of the maximum). Cycles 17 and 18 caused the fractures in the infill from Cycle 16 to grow only slightly. However, they did cause some new fractures, as indicated in figure 5-9 (denoted F2). An example is shown in figure 5-28. Additionally, several more pop-rivets were lost during Cycles 16-18 and additional fractures in the infill plate near the failed pop-rivet locations were noticed. By the end of Cycle

18 the fractures in the infill plate had caused the strength of the wall to drop to 480 kN, or 77% of the maximum.

During the first excursion to $+4\delta_y$ (33.5 mm, 1.83% drift) the existing fractures in the infill propagated substantially. Figures 5-29, 5-30, and 5-31 show the fractures in the infill along lines 1, 2, and 3 respectively. The second excursion to $+4\delta_y$ caused these fractures to again propagate substantially, which in turn, caused the resistance of the wall to degrade to 294 kN or 47% of the maximum base shear achieved, thus the test was terminated at this point.

5.3.3   Specimen F2

Specimen F2 exhibited linear behavior during the first 6 cycles of testing. At a displacement of 5.3 mm (0.29% drift) and load of 365 kN during the first half of Cycle 7 some nonlinear behavior was observed. Based on visual extrapolation of the force-displacement curve this was deemed to be the yield point for this specimen. In the cycles prior to this there had been no audible buckling sounds from the infill and the magnitude of the buckling waves along the infill plate were small. During Cycles 7, 8, and 9, however, the audible buckling sounds (which is the tension field alternating in orientation during reversed cycling) began and the magnitude of the buckling waves grew to what is shown in figure 5-32. No strength degradation was observed during these three cycles at $\pm1\delta_y$ and the maximum base shear was 365 kN.

During the three cycles (10, 11, and 12) at $\pm2\delta_y$ (10.7 mm, 0.58% drift) the buckling sounds grew louder and the magnitude of the buckling waves on the infill plate grew larger as well (figure 5-33). In Cycle 12, a fracture in the infill plate at the upper north corner was observed and is shown in figure 5-34. The fracture was along the weld of the infill to the intermediate WT and started at the end of the fillet weld (an area of stress concentration). After further inspection, the other three corners of the infill plate were found to have similar fractures at the ends of the welds. All fractures were less than 13 mm in length and did not effect the capacity of the wall. During each cycle at $\pm2\delta_y$ the maximum base shear was approximately 458 kN.

The specimen was then subjected to three cycles at $\pm3\delta_y$ (16.5mm, 0.90% drift). Again the noise of the tension field reorienting itself grew louder compared to the previous displacement step.

84

The magnitude of the buckling waves during Cycle 15 are shown in figure 5-35, and it can be seen that more waves appeared over the plate than in the previous displacement step. Additionally, from the square grid painted over the whitewash on the infill it is apparent that the buckling waves, and hence the tension field, are oriented at approximately 45° from vertical. This agrees with the orientation angle calculated using (2-4. Large residual buckles remained at the zero base shear point during the cycles at $\pm 3\delta_y$ as shown in figure 5-36. This indicated that the plate had undergone significant plastic elongation. The fractures in the corners of the infill plate grew only slightly during the cycles at $\pm 3\delta_y$ and none were longer than 19 mm. Figure 5-37 shows the fractures in the lower south corner being opened up when displacement was applied to the north ($+3\delta_y$). Additionally, plastic folds (kinks) were beginning to form at the corners of the infill plate. Figures 5-38 and 5-39 show the folds forming from the upper north and south corners, respectively. The fold in the upper south corner was formed when displacement was applied to the south (to $-3\delta_y$), and vice-versa. No strength degradation was observed during the cycles at $\pm 3\delta_y$ and the maximum base shear was 494 kN.

Only 2 cycles were performed at $\pm 4\delta_y$ (22.1 mm, 1.21% drift) and every subsequent displacement step, in accordance with ATC 24 (ATC, 1992). Figure 5-40 shows the magnitude of infill buckling during this stage and it is again apparent that the tension field is oriented at approximately 45° from vertical. The fractures in the corners of the infill grew slightly again and were all less than 25 mm. Figure 5-41 shows the same fracture as figure 5-34. Additionally, the plastic folds forming from the corners became more pronounced during the cycles at $\pm 4\delta_y$ as shown in figures 5-42 and 5-43, which show the fold in the lower south corner from the west and east sides of the wall, respectively. Again there was no degradation of strength during these two cycles and the maximum base shear was 520 kN.

Figure 5-44 shows the buckling of the infill plate during Cycle 18 at $+5\delta_y$ (28.0mm, 1.53% drift). Figures 5-45 and 5-46 show the fractures in the lower south corner of the infill plate at this stage. The former shows the fracture at $-5\delta_y$ and the latter shows it at $+5\delta_y$. All fractures were less than 50 mm long at this point. Figure 5-47 shows the plastic fold in the lower north corner of the infill at $-5\delta_y$ and figure 5-48 shows the plastic fold in the upper north corner of the infill at $+5\delta_y$.

Still no degradation in the strength of the wall was observed and the maximum base shear was 555 kN.

At $\pm6\delta_y$ (33.3 mm, 1.82% drift) there were eight distinct buckling waves in the infill panel as shown in figure 5-49 and they still appear to be oriented at 45° from vertical. At zero base shear the residual buckling was dramatic and is shown in figure 5-50. By the end of the two cycles at this displacement step the fractures in the corners of the infill plate had grown to a maximum of 75 mm. Figures 5-51 and 5-52 show the fractures in the lower south and lower north corners of the infill at $+6\delta_y$ and $-6\delta_y$ of Cycle 21 respectively. In addition to the fractures in the corners of the infill plate, a small fracture on a plastic fold line approximately 125 mm away from the lower south corner was observed and is shown in figure 5-53. The maximum base shear observed during the $\pm6\delta_y$ cycles was 587 kN and there was no strength degradation.

During the two cycles at $\pm7\delta_y$ (39.0 mm, 2.13% drift) the fractures in the corners of the infill continued to propagate. Figures 5-54 and 5-55 show the fractures in the lower north and upper south corners respectively. The buckling wave pattern was similar to what was observed at $\pm6\delta_y$ in-so-far as there were again eight distinct waves oriented at 45° from vertical. No change in the fracture of figure 5-53 was observed. There was a 20 kN drop (from 623 kN to 603 kN) in the base shear between the first and second cycles at $\pm7\delta_y$.

The buckling of the infill panel at $\pm8\delta_y$ (44.6 mm, 2.44% drift) is shown in figure 5-56 from which it is apparent that there are now 9 distinct waves (the newest having formed at this displacement step) oriented at 45° from vertical. Propagation of the fractures at the corners of the infill plate continued and are shown in figures 5-57 and 5-58 for the lower south and north corners respectively. The former is during the first excursion to $+8\delta_y$ and the latter is during the first excursion to $-8\delta_y$. The maximum base shear during the cycles at $\pm8\delta_y$ was 625 kN and there was a 20 kN drop between the first and second cycles.

Due the ductile behavior of the specimen it was decided that the increment of each displacement step should be increased to $2\delta_y$ following Cycle 25 (the second cycle at $8\delta_y$). At $\pm10\delta_y$ (56.2 mm, 3.07% drift) the fractures in the corners continued to propagate, examples of which are

shown figures 5-59 and 5-60 for the lower south and upper north corners at $+10\delta_y$ of Cycle 26, respectively. Figure 5-61 is a blow up of the fracture in figure 5-60 and shows how it is beginning to propagate toward the center of the infill plate. Figure 5-62 shows the fracture at the lower north corner of the infill, which at this point is approximately 150 mm long. Maximum base shears of 660 kN and 625 kN were observed for the first and second cycles at $\pm10\delta_y$, respectively.

Figure 5-63 shows the buckling of the infill plate at the final displacement step, $\pm12\delta_y$ (67.0 mm, 3.65% drift). The specimen was subjected to 4 cycles at this displacement because the hydraulic actuator had reached its maximum stroke capacity. During these 4 cycles the fractures in the corners of the infill plate propagated substantially. Figures 5-64, 5-65, 5-66, and 5-67 show the lower north, upper north, upper south, and lower south corners of the infill plate, respectively. Most of the fractures at the end of the test were between 380 and 460 mm long. During the first cycle at $\pm12\delta_y$ the maximum base shear was 645 kN while during the fourth cycle it was down to 503 kN. During the final cycle, fractures averaging 35 mm in length were observed in the angles of the web-angle beam-to-column connections.

5.4   Bare Frame Testing

To quantify the contribution of the boundary frames to the global system behavior, the two boundary frames were tested alone after the infills were removed. The first boundary frame (BF1), was used in specimens F1 and F2, and the second boundary frame (BF2), was used in specimen C1.

5.4.1   Boundary Frame 1 (BF1)

Following the testing of specimen F1, BF1 was tested to determine it's hysteretic behavior. The frame was subjected to 3 cycles at 38 mm of displacement or 7 times the maximum displacement of specimen F1. There were no major problems during this testing and the results will be discussed and used in Section 6. BF1 was not retested following the testing of specimen F2 because the web-angle connections fractured during that latter test. In Section 6, data from the testing of BF1 to 38 mm will be extrapolated, using a calibrated hysteretic model, to the displacements obtained during the testing of specimen F2.

87

5.4.2   Boundary Frame 2 (BF2)

BF2 was tested after the removal of the infill plate of specimen C1. To assure that enough data would be available to accurately model BF2 (which would also give added confidence in the accuracy of modeling BF1), the frame was subjected to the same displacement history as specimen C1 except that only two cycles were performed at each displacement step.

5.5   Summary

Three light-gauge steel plate shear wall specimens were tested under quasi-static loading. Specimen F1 performed poorly and suffered a premature failure of the epoxy connection between the infill plate and intermediate WT mounted on the upper beam. The failure occurred prior to the specimen reaching any nonlinear behavior and significant hysteretic energy dissipation.

Specimen C1 was successfully tested to a maximum displacement of 40.6 mm ($4\delta_y$, 2.2% drift) and maximum base shear of 625 kN (occurring at $2\delta_y$). Failure of the specimen was from fractures of the infill plate at locations of repeated local buckling, which developed as a result of the corrugated profile of the infill plate.

Specimen F2 was successfully tested to 82.6 mm of displacement ($12\delta_y$, 4.5% drift). The maximum base shear was 660 kN and occurred at $10\delta_y$. Failure of the specimen was due to large fractures at the corners of the infill plate that propagated along the fillet welds that connected the infill plate to the intermediate WTs. Although the infill plate could still carry some load in spite of its extensive damage, testing stopped when the angles of the beam-to-column connections of the boundary frame suffered large fractures at frame drifts of $12\delta_y$.
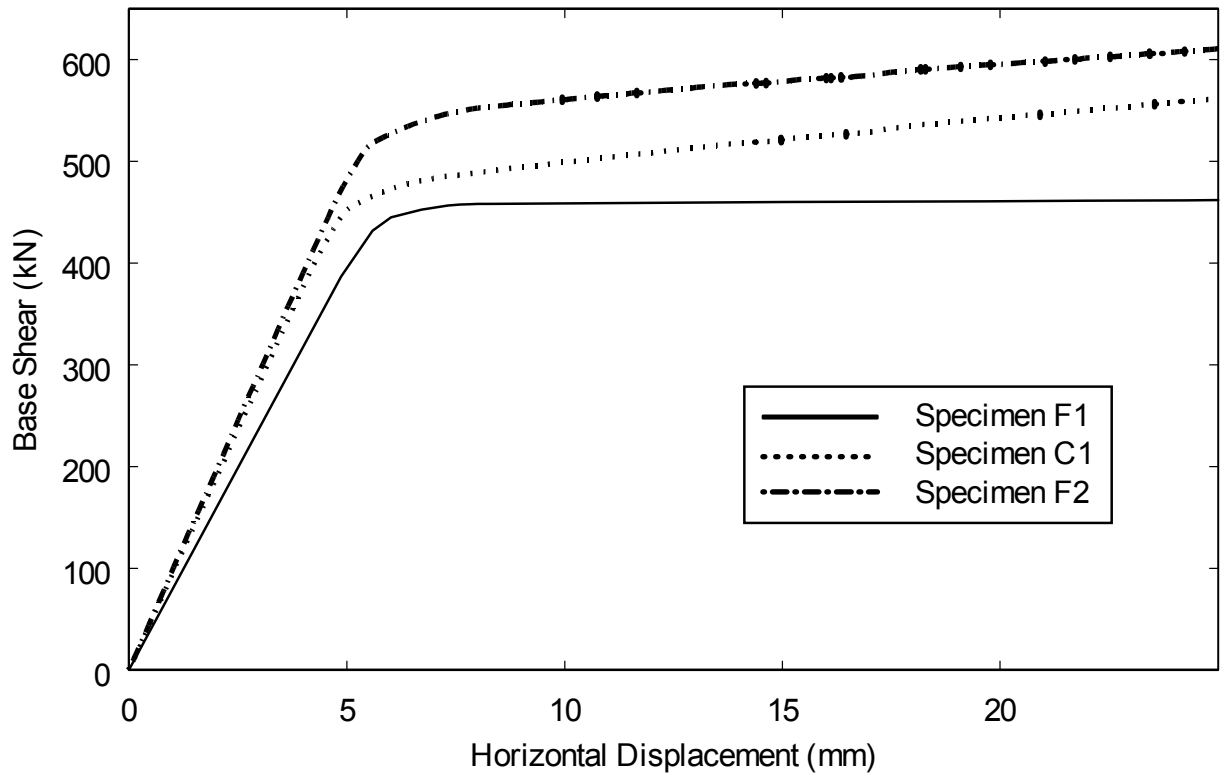
FIGURE 5-1 Predicted Pushover Curves
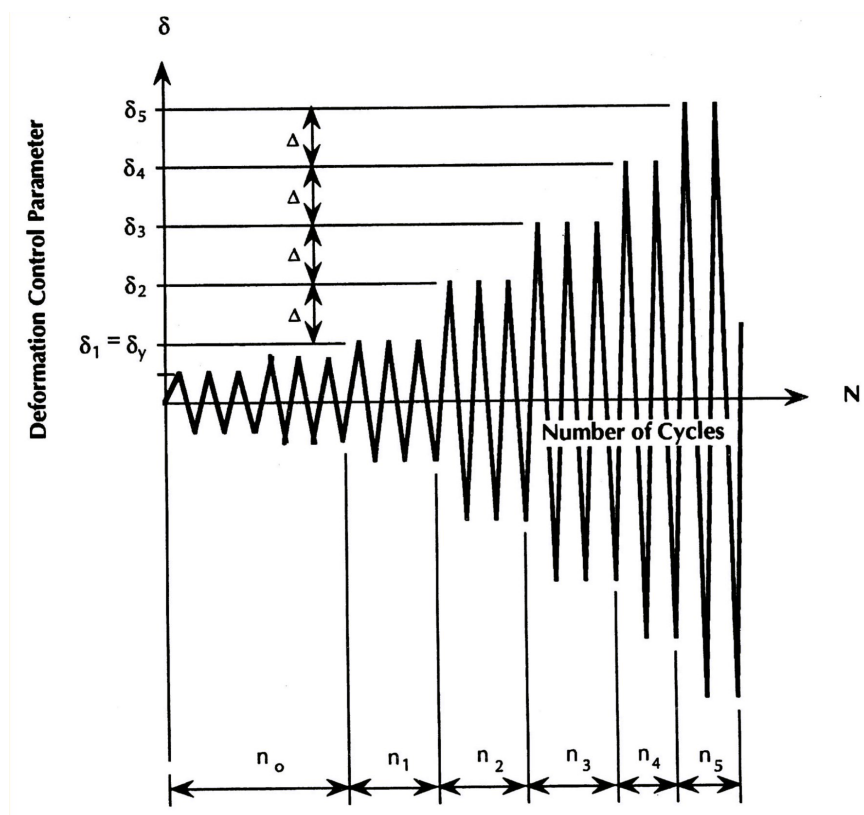
FIGURE 5-2 ATC Loading Protocol (ATC, 1992)

89
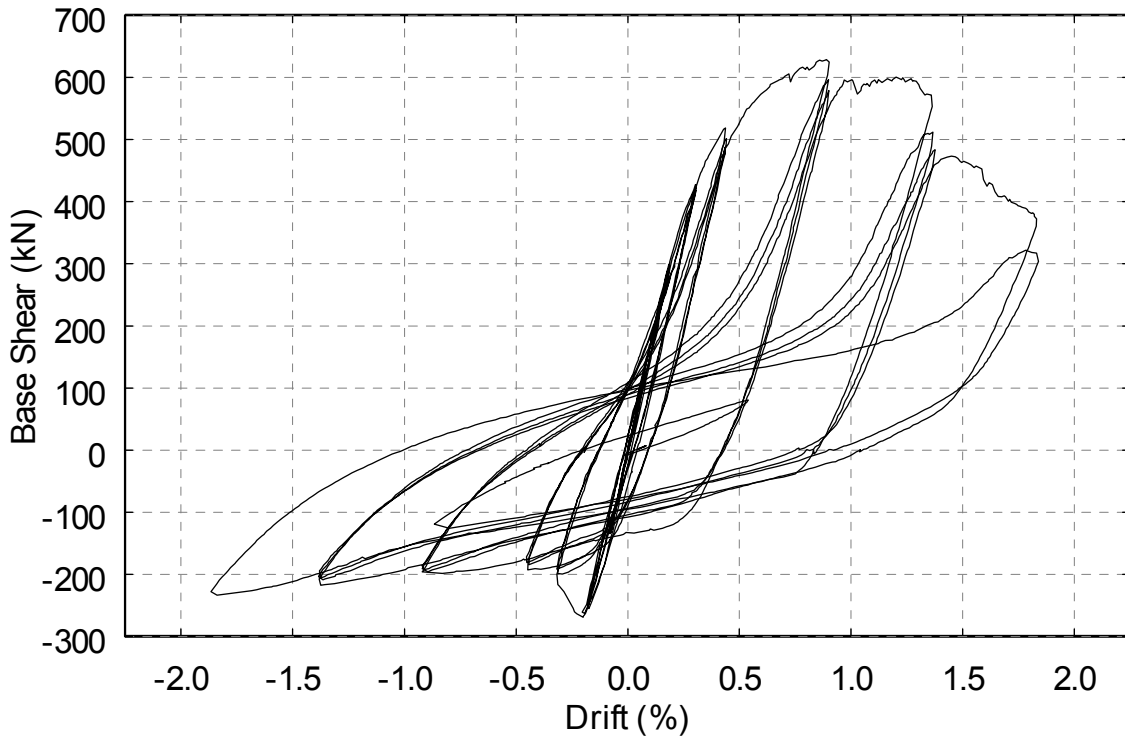
FIGURE 5-3 Hysteresis for Specimen C1
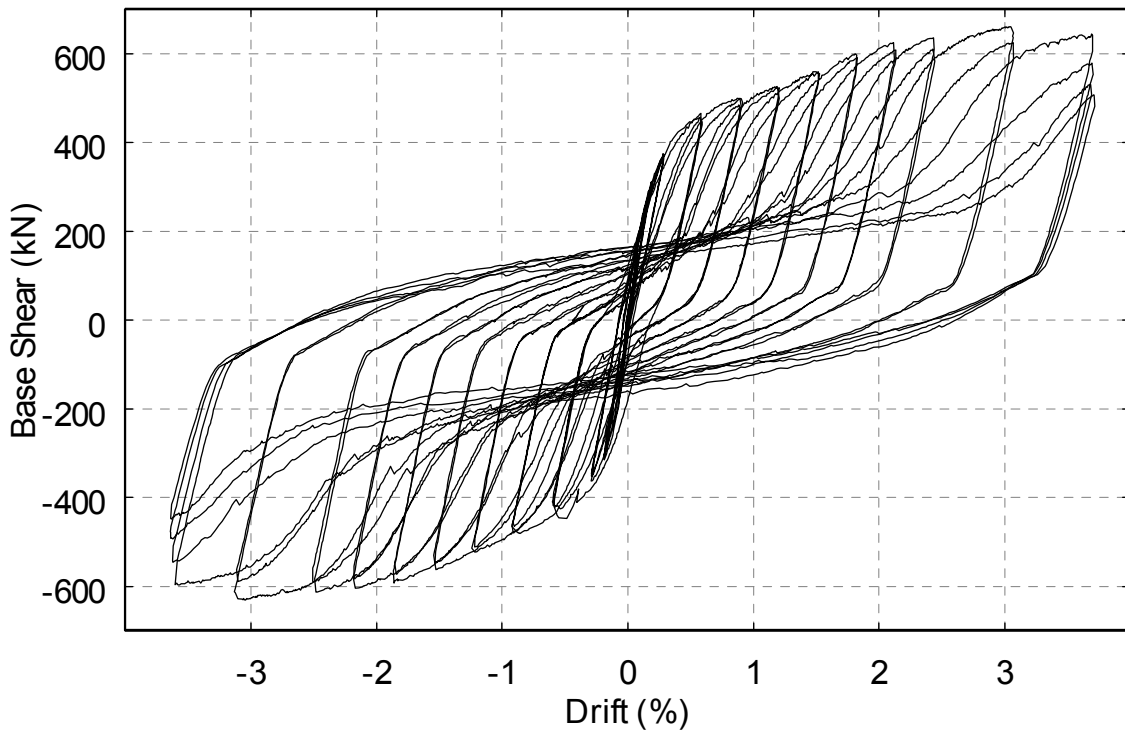
FIGURE 5-4 Hysteresis for Specimen F2

90

FIGURE 5-5 Epoxy Crack - Top of South Column
(Specimen F1, Cycle 2, +0.25δ_y)

FIGURE 5-6 Epoxy Crack - North End of Top Beam
(Specimen F1, Cycle 4, +0.4δ_y)
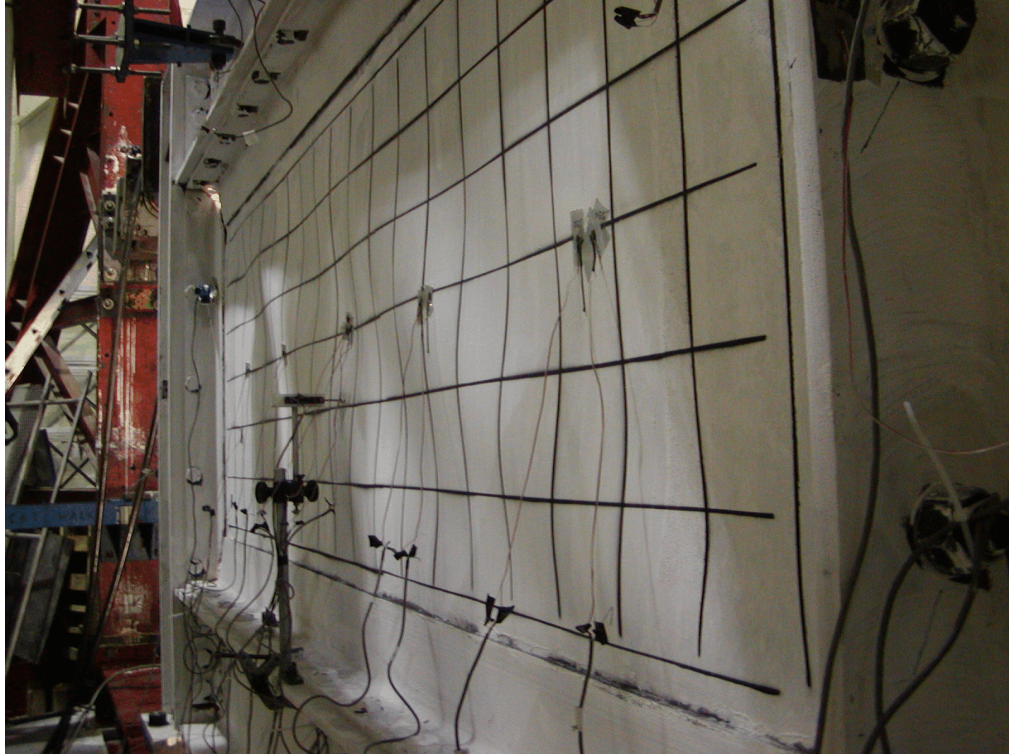
FIGURE 5-7 Infill Buckling (Specimen F1, Cycle 4, $-0.4\delta_y$)
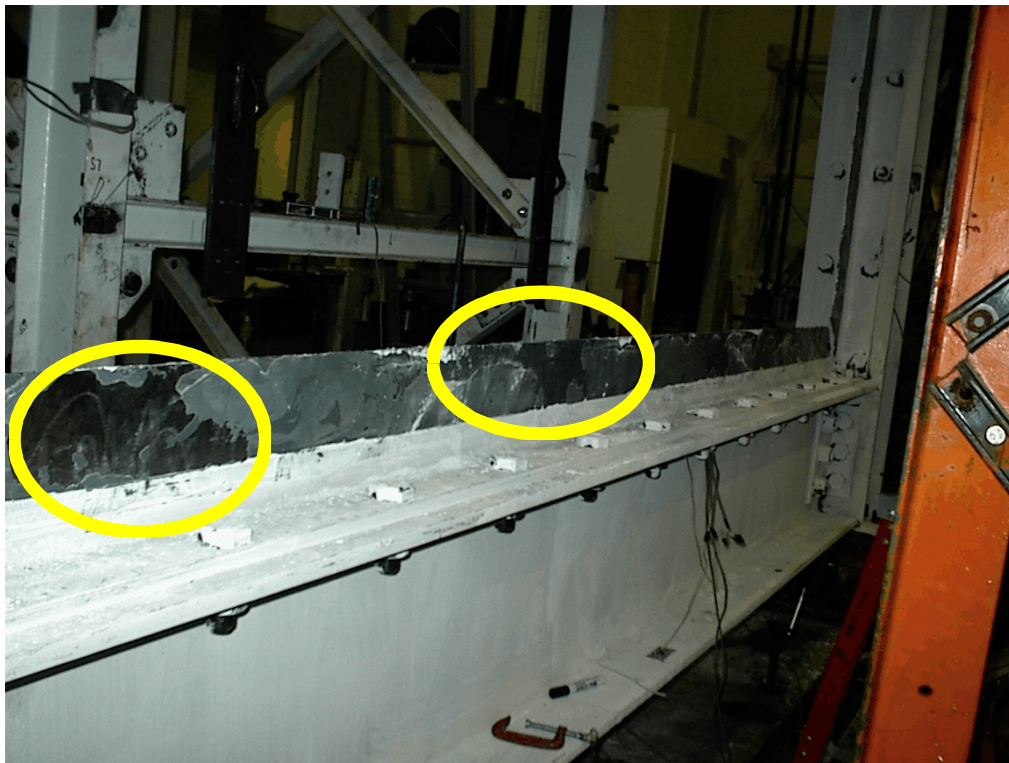
FIGURE 5-8 Poor Epoxy Coverage (Specimen F1)
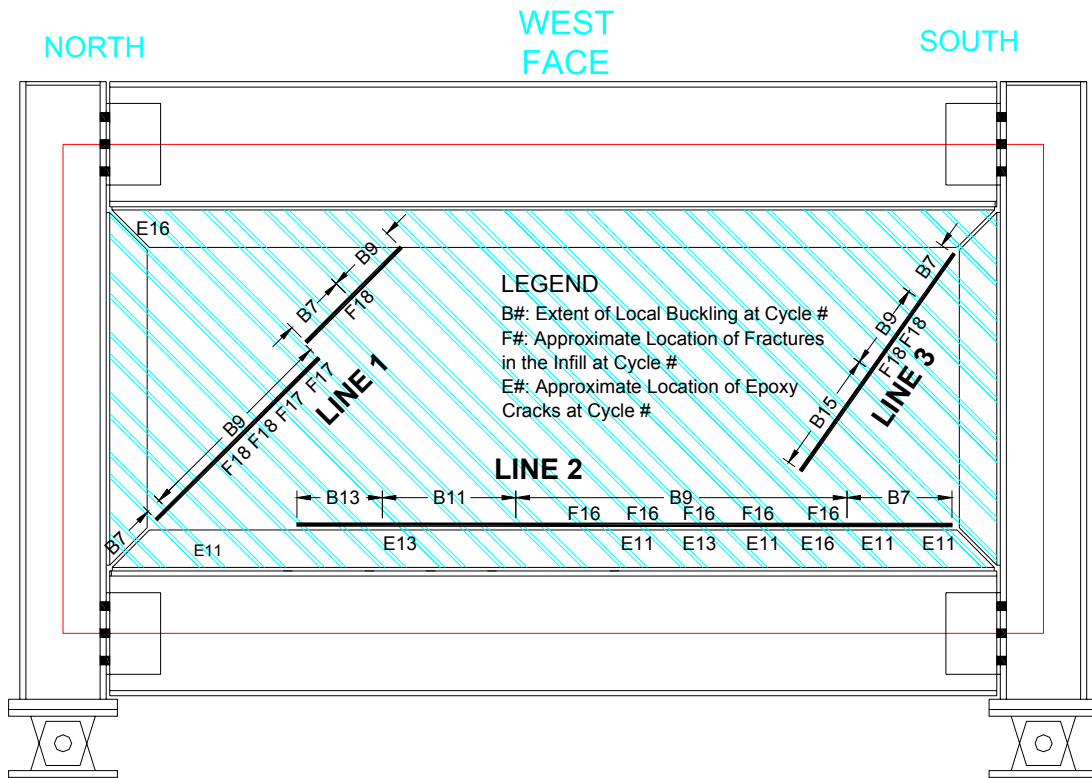
FIGURE 5-9 Schematic of Local Buckling and Damage for Specimen C1

**FIGURE 5-10 Local Buckling Along Line 1
(Specimen C1, Cycle 9, -0.7δ_y)**

FIGURE 5-11 Local Buckling Along Line 2
(Specimen C1, Cycle 9, -0.7δ_y)

FIGURE 5-12 Local Buckling Along Line 3
(Specimen C1, Cycle 9, -0.7δ_y)

FIGURE 5-13 Local Buckling Along Line 1
(Specimen C1, Cycle 11, -1δ_y)

FIGURE 5-14 Local Buckling Along Line 2
(Specimen C1, Cycle 11, -1δ_y)

FIGURE 5-15 Epoxy Crack Along Bottom Beam
(Specimen C1, Cycle 12, -1δ_y)
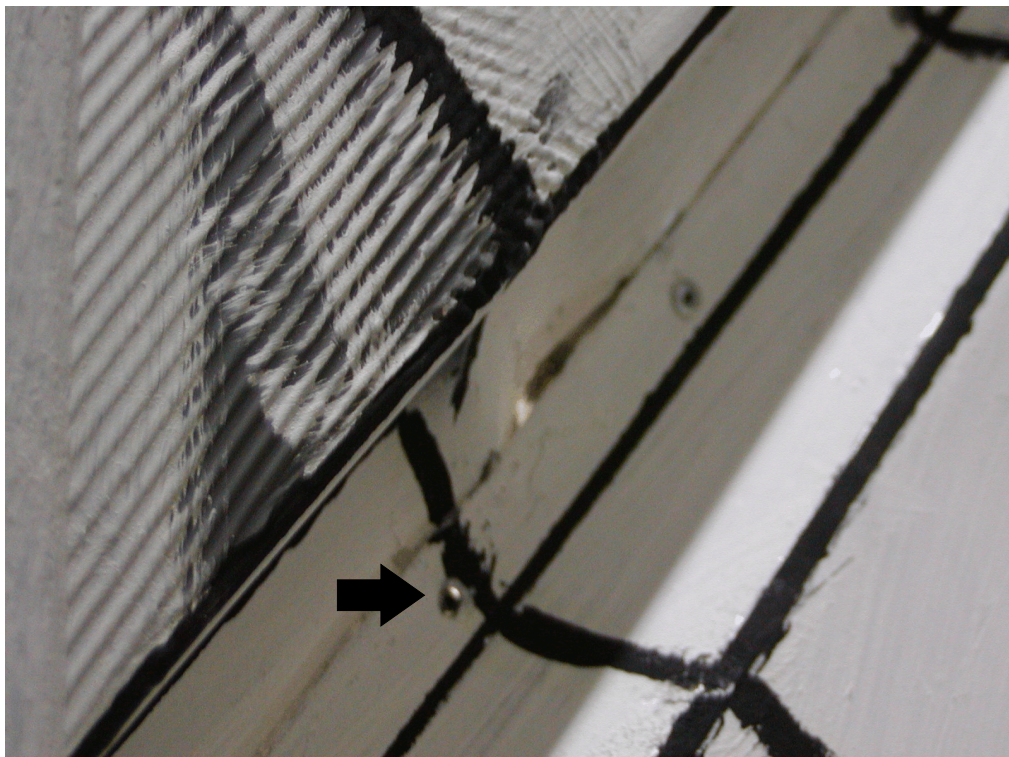
FIGURE 5-16 Failed Pop-rivet (Specimen C1, Cycle 12, +1δ_y)

FIGURE 5-17 Local Buckling Along Line 1
(Specimen C1, Cycle 13, -2δ_y)
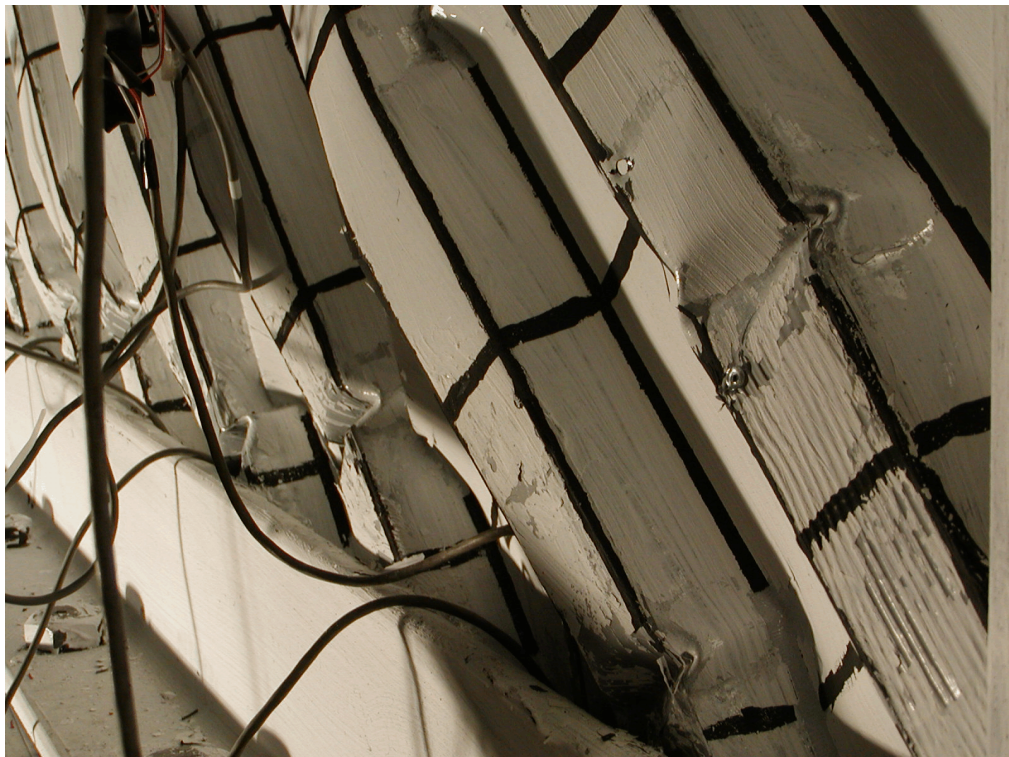
FIGURE 5-18 Local Buckling Along Line 2
(Specimen C1, Cycle 13, -2δ_y)

FIGURE 5-19 North Section (Specimen C1, Cycle 15, -2δ$_y$)

FIGURE 5-20 South Section (Specimen C1, Cycle 15, -2δ$_y$)

FIGURE 5-21 Epoxy Crack Along Bottom Beam
(Specimen C1, Cycle 13, -2δ_y)

FIGURE 5-22 Failed Pop-rivets (Specimen C1, Cycle 13, -2δ_y)

FIGURE 5-23 Fractures Along Line 2 (Specimen C1, Cycle 16, +3δ$_y$)

FIGURE 5-24 Fractures Along Line 2 (Specimen C1, Cycle 16, +3δ$_y$)

FIGURE 5-25 Epoxy Crack in Upper North Corner
(Specimen C1, Cycle 16, +3δ_y)
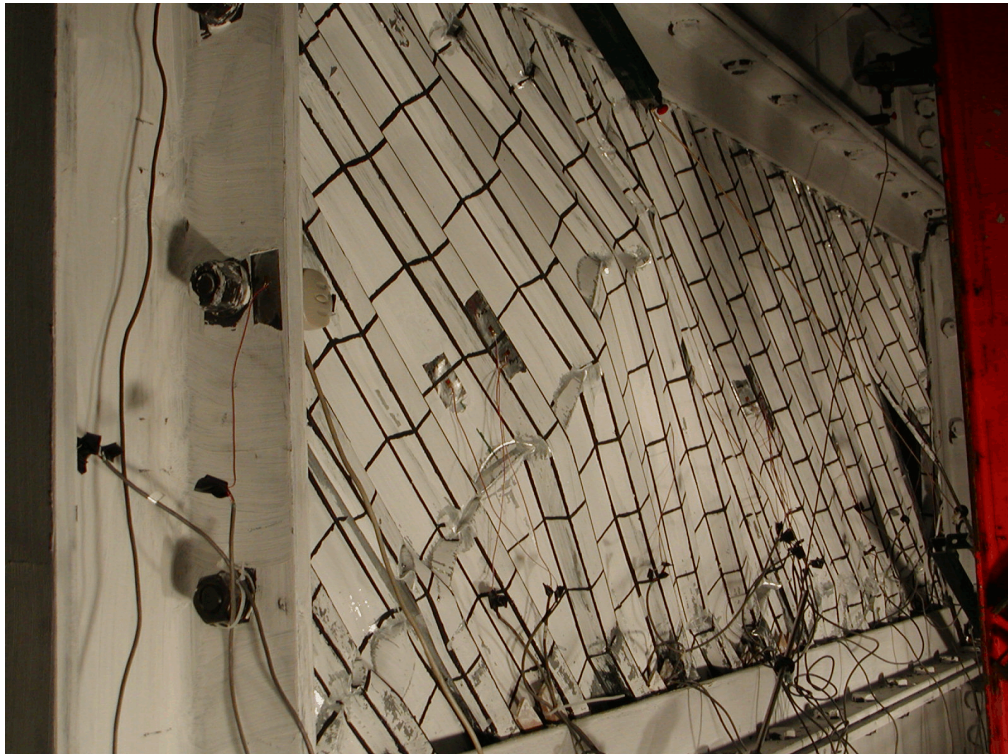
FIGURE 5-26 Local Buckling Along Line 1
(Specimen C1, Cycle 16, -3δ_y)

FIGURE 5-27 Local Buckling Along Lines 2 and 3
(Specimen C1, Cycle 16, -3δ$_y$)

FIGURE 5-28 Fracture Along Line 1 (Specimen C1, Cycle 18, +3δ$_y$)

FIGURE 5-29 Fractures Along Line 1 (Specimen C1, Cycle 19, +4δ$_y$)

FIGURE 5-30 Fractures Along Line 2 (Specimen C1, Cycle 19, +4δ$_y$)

FIGURE 5-31 Fractures Along Line 3 (Specimen C1, Cycle 19, +4δ$_y$)

FIGURE 5-32 Infill Buckling (Specimen F2, Cycle 9, -1δ$_y$)

FIGURE 5-33 Infill Buckling (Specimen F2, Cycle 12, $+2\delta_y$)
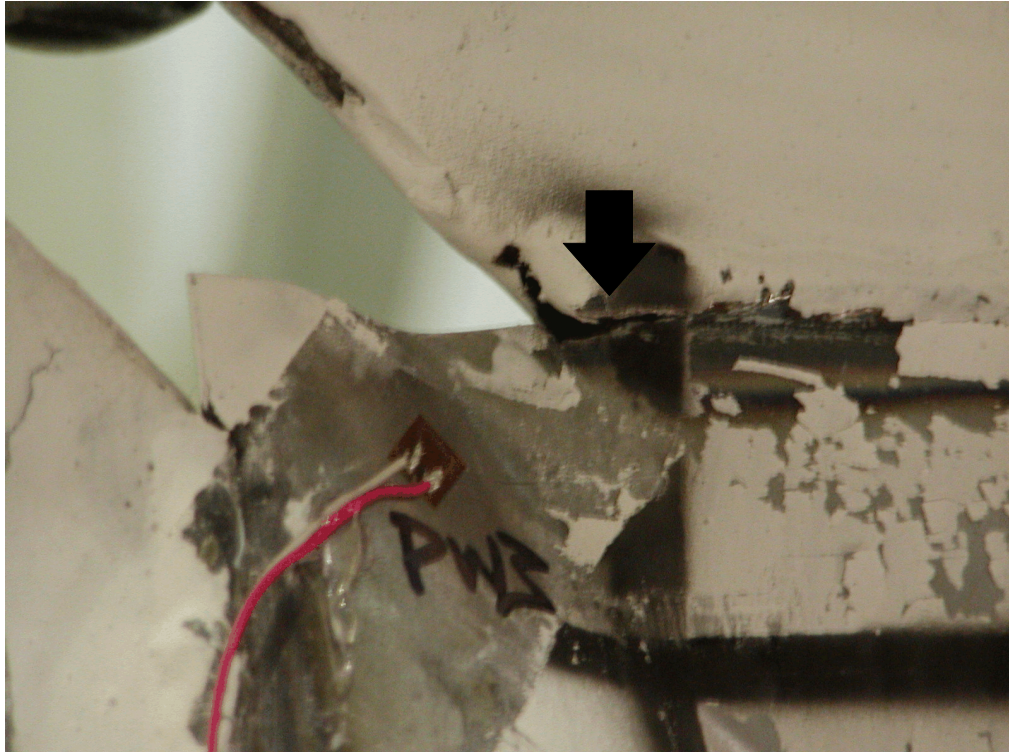
FIGURE 5-34 Infill Fracture in Upper North Corner
(Specimen F2, Cycle 12, $+2\delta_y$)

FIGURE 5-35 Infill Buckling (Specimen F2, Cycle 15, -3δ_y)

**FIGURE 5-36 Residual Buckling at Zero Load
(Specimen F2, Cycle 15)**

FIGURE 5-37 Infill Fracture in Lower South Corner
(Specimen F2, Cycle 15, $+3\delta_y$)
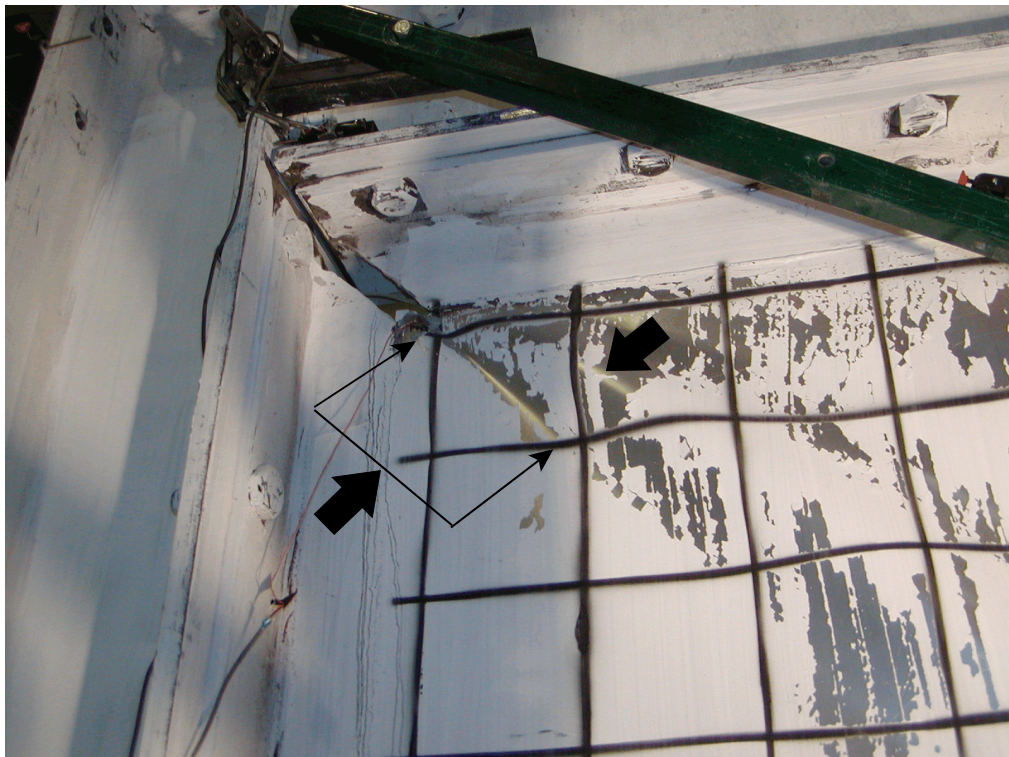
FIGURE 5-38 Plastic Fold in Upper North Corner
(Specimen F2, Cycle 15, $+3\delta_y$)

FIGURE 5-39 Plastic Fold in Upper South Corner
(Specimen F2, Cycle 15, -3δ$_y$)
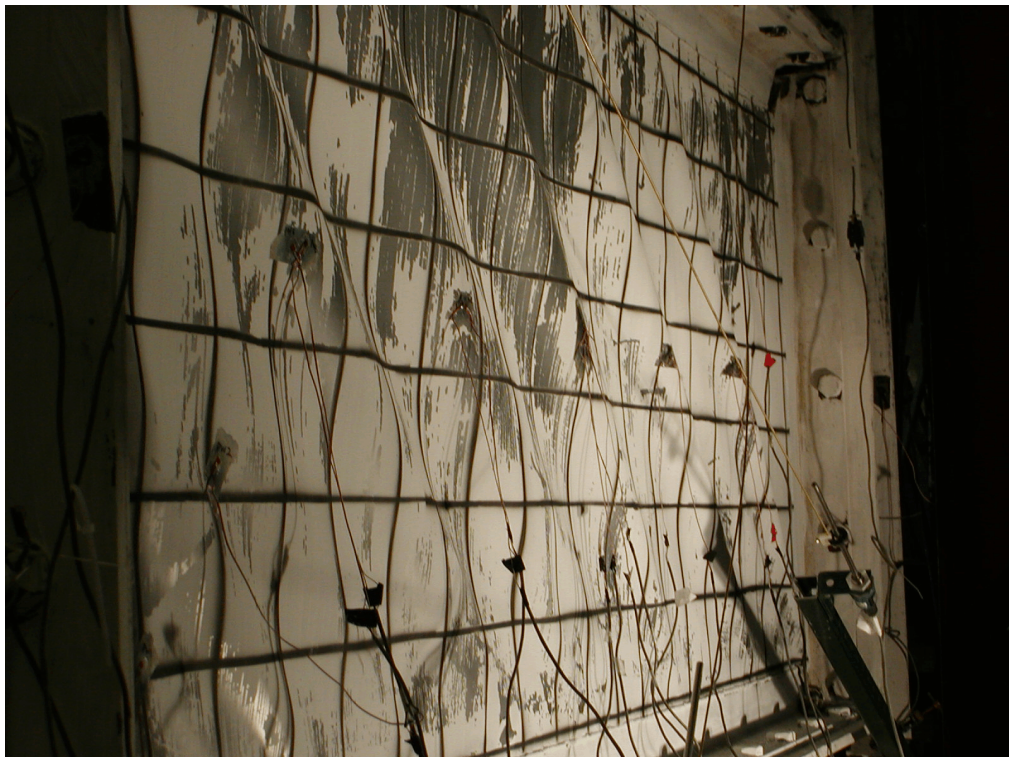
FIGURE 5-40 Infill Buckling (Specimen F2, Cycle 17, +4δ$_y$)

FIGURE 5-41 Infill Fracture in Upper North Corner
(Specimen F2, Cycle 17, +4δ$_y$)

FIGURE 5-42 Plastic Fold in Lower South Corner
Taken from West Side (Specimen F2, Cycle 17, +4δ$_y$)

**FIGURE 5-43 Plastic Folds in Lower South Corner
Taken From East Side (Specimen F2, Cycle 17, +4δ$_y$)**

FIGURE 5-44 Infill Buckling (Specimen F2, Cycle 18, +5δ$_y$)

FIGURE 5-45 Infill Fracture in Lower South Corner
(Specimen F2, Cycle 18, -5δ$_y$)

FIGURE 5-46 Infill Fracture in Lower South Corner
(Specimen F2, Cycle 19, +5δ$_y$)

FIGURE 5-47 Plastic Fold in Lower North Corner
(Specimen F2, Cycle 18, -5δ$_y$)

FIGURE 5-48 Plastic Fold in Upper North Corner
(Specimen F2, Cycle 19, +5δ$_y$)

FIGURE 5-49 Infill Buckling (Specimen F2, Cycle 20, +6δ$_y$)
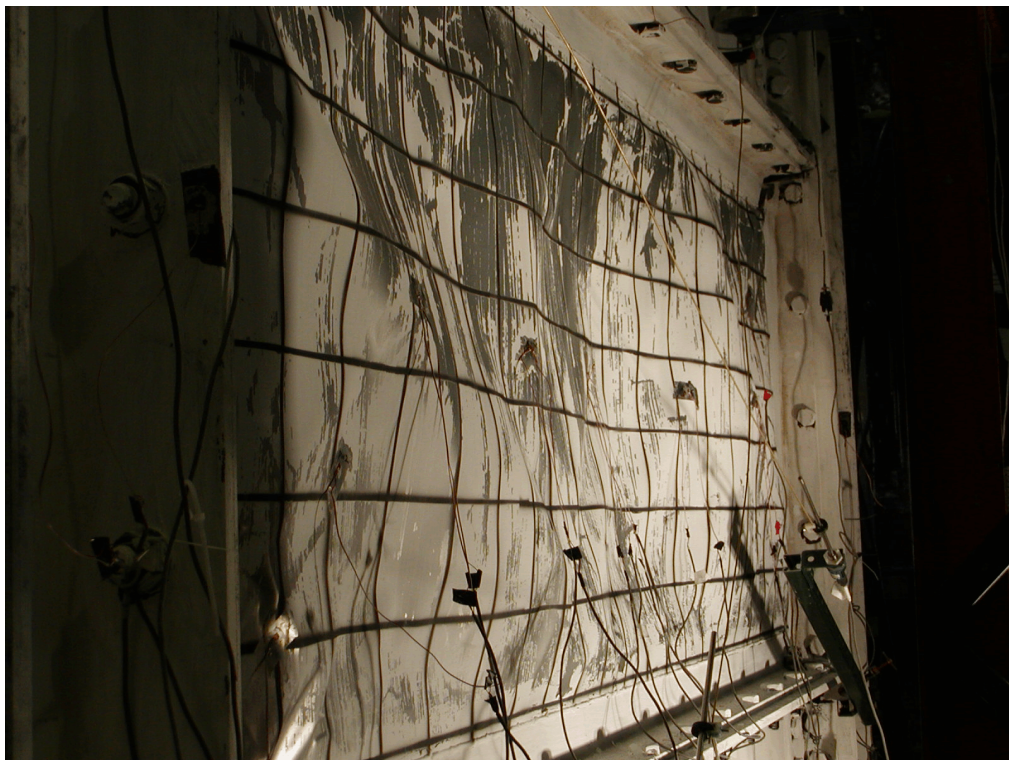
FIGURE 5-50 Residual Buckling at Zero Load
(Specimen F2, Cycle 20)

FIGURE 5-51 Infill Fracture in Lower South Corner
(Specimen F2, Cycle 21, $+6\delta_y$)
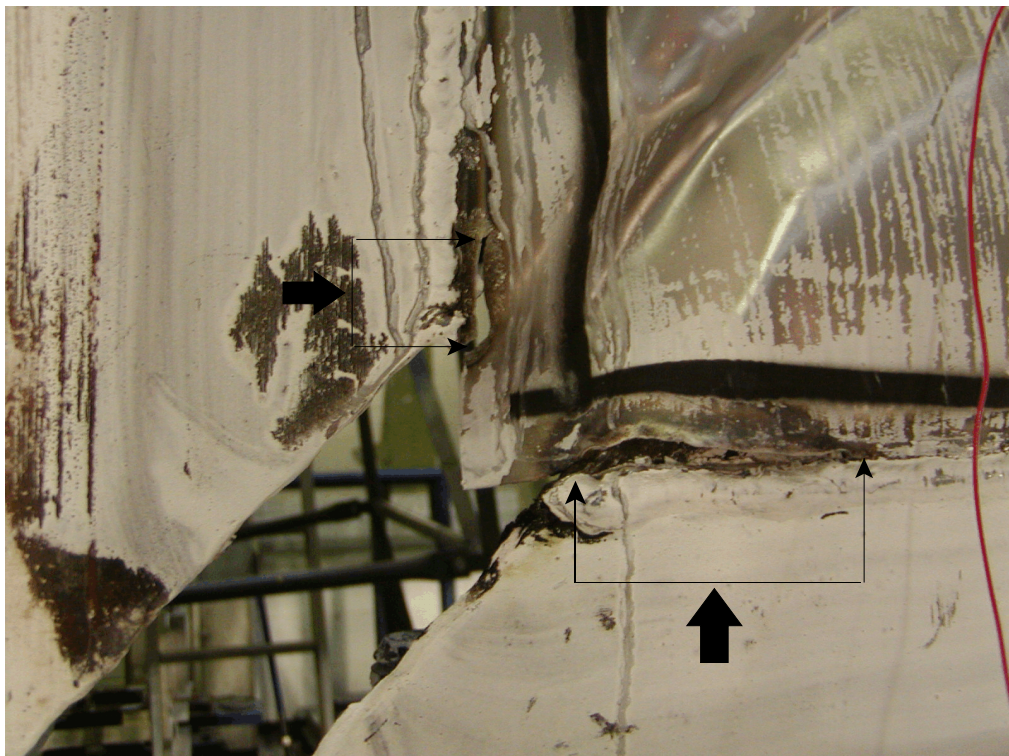
FIGURE 5-52 Infill Fracture in Lower North Corner
(Specimen F2, Cycle 21, $-6\delta_y$)

FIGURE 5-53 Infill Tear Near South Corner
(Specimen F2, Cycle 21, -6δ$_y$)

FIGURE 5-54 Infill Fracture in Lower North Corner
(Specimen F2, Cycle 23, -7δ$_y$)

FIGURE 5-55 Infill Fracture in Upper South Corner
(Specimen F2, Cycle 23, -7δ_y)
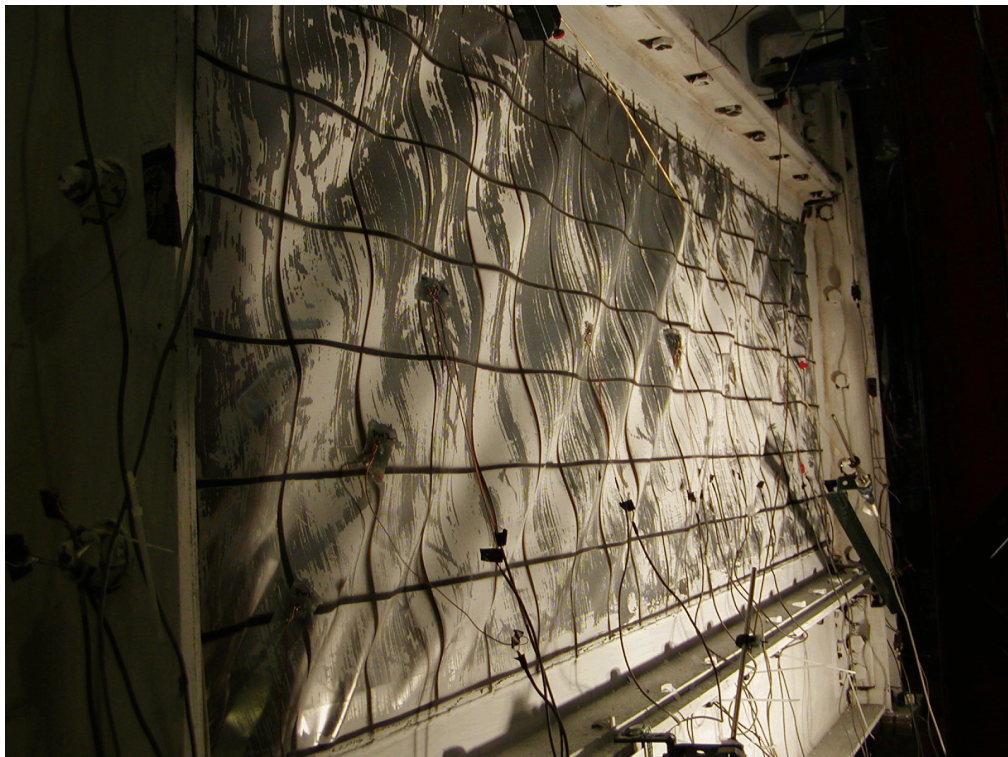
FIGURE 5-56 Infill Buckling (Specimen F2, Cycle 24, -8δ_y)

FIGURE 5-57 Infill Fracture in Lower South Corner
(Specimen F2, Cycle 24, $+8\delta_y$)
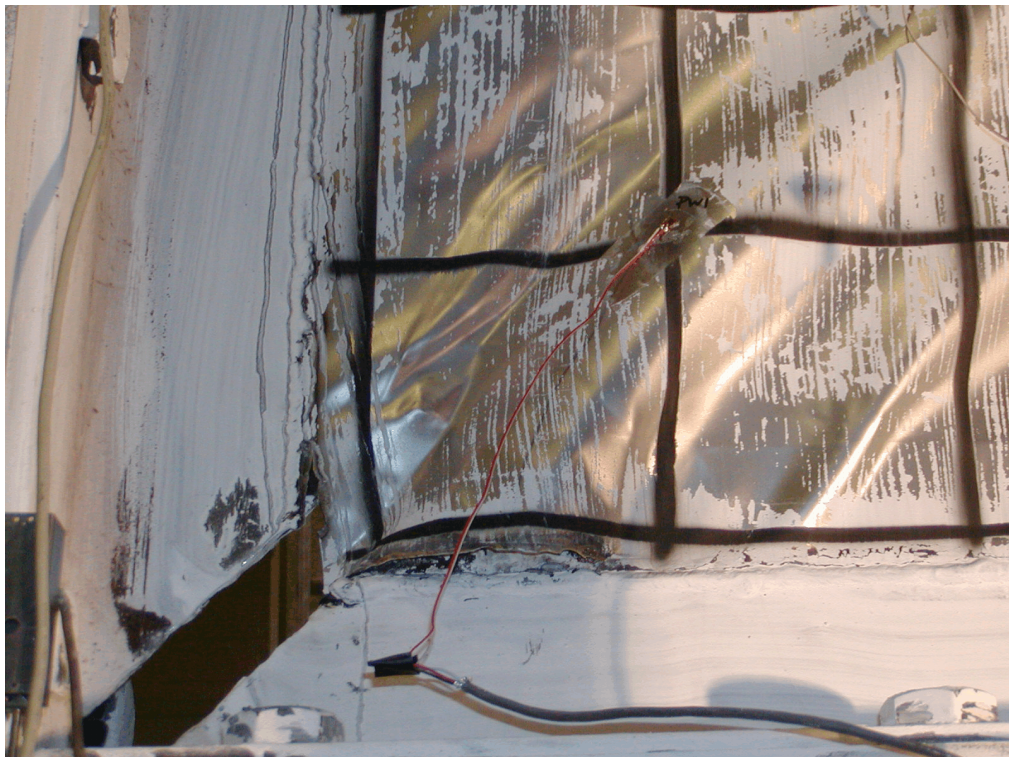
FIGURE 5-58 Infill Fracture in Lower North Corner
(Specimen F2, Cycle 24, $-8\delta_y$)

FIGURE 5-59 Infill Fracture in Lower South Corner
(Specimen F2, Cycle 26, +10δ$_y$)

FIGURE 5-60 Infill Fracture in Upper North Corner
(Specimen F2, Cycle 26, +10δ$_y$)

FIGURE 5-61 Infill Fracture in Upper North Corner Redirecting Towards Center of Infill (Specimen F2, Cycle 26, +10δ$_y$)

FIGURE 5-62 Infill Fracture in Lower North Corner (Specimen F2, Cycle 26, +10δ$_y$)

FIGURE 5-63 Infill Buckling (Specimen F2, Cycle 29, +12δ$_y$)
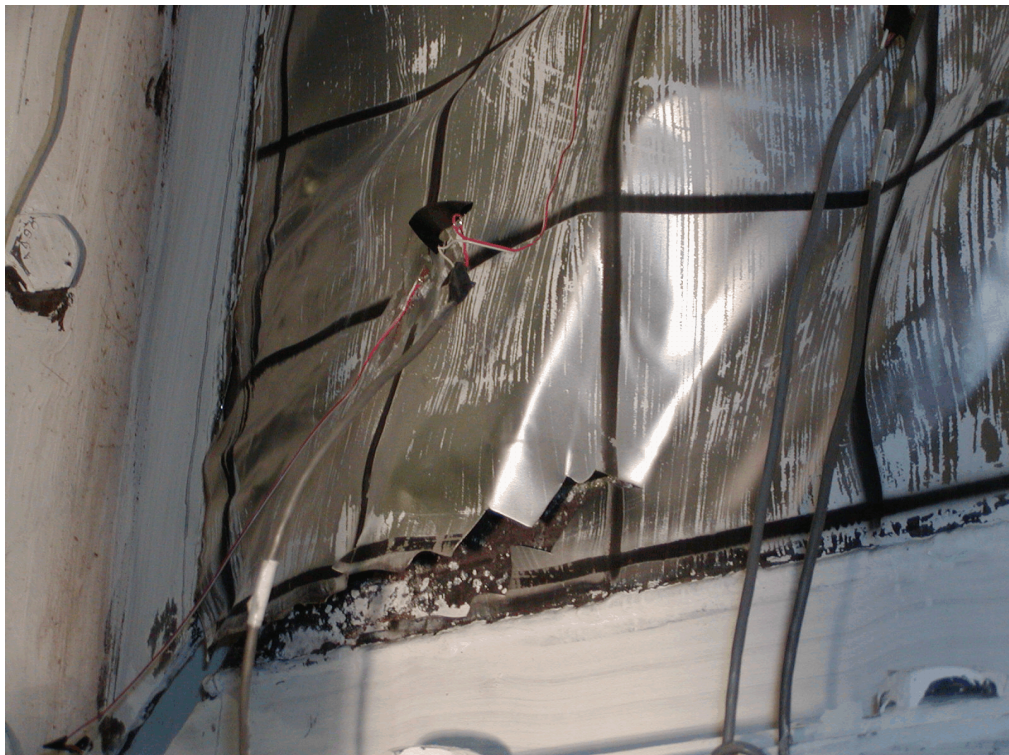
**FIGURE 5-64 Infill Fracture in Lower North Corner
(Specimen F2, Cycle 31, -12δ$_y$)**
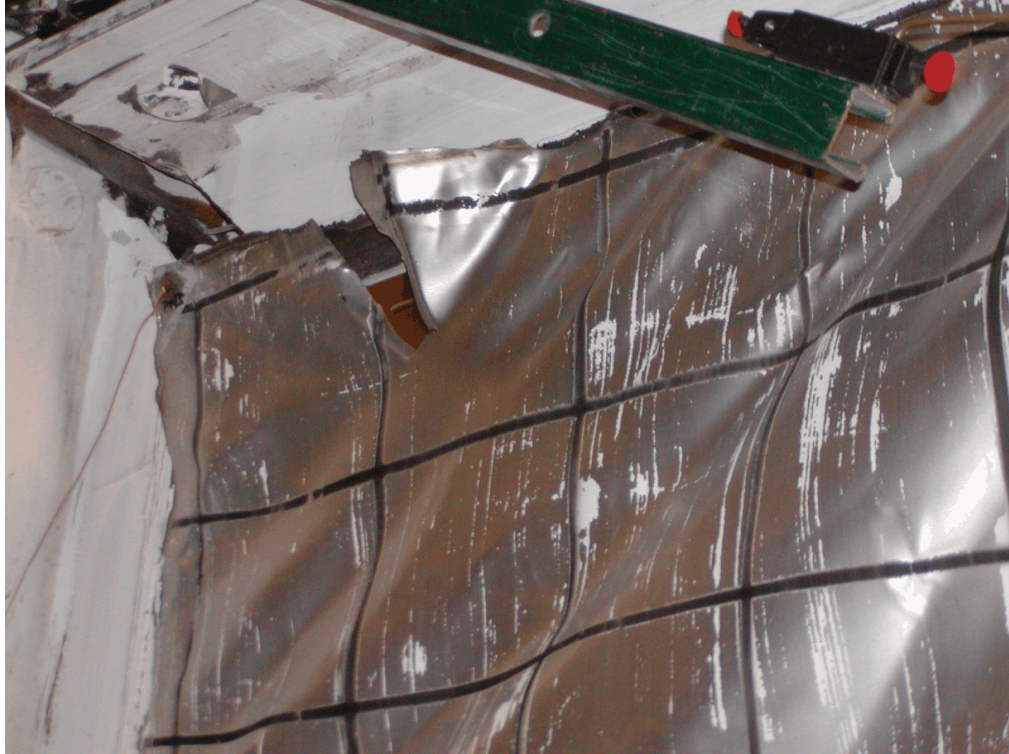
FIGURE 5-65 Infill Fracture in Upper North Corner
(Specimen F2, Cycle 31, -12δ$_y$)

FIGURE 5-66 Infill Fracture in Upper South Corner
(Specimen F2, Cycle 31, -12δ$_y$)

FIGURE 5-67 Infill Fracture in Lower South Corner
(Specimen F2, Cycle 31, -12δ$_y$)

SECTION 6

DISCUSSION AND COMPARISON OF EXPERIMENTAL RESULTS

6.1   General

This section quantitatively describes the test results for the three light-gauge steel plate shear wall specimens. First, results from testing of boundary frames 1 (BF1) and 2 (BF2), without the infills, are described and an analytical model is calibrated to fit these results. Next, the light-gauge steel plate shear walls results are presented in terms of the obtained hysteretic force-displacement loops for the systems, with and without the boundary frame contributions (deducted using the calibrated analytical models).

In all cases the force-displacement loops are presented in terms of force versus percent drift, with positive displacements (and drifts) corresponding to the top of the specimens moving north (as labeled in the figures of Sections 4 and 5). Percent drift is measured as the difference between the horizontal displacements at the middle of the top and bottom beams of the specimen (as measured by Temposonics T1W and T5 shown in figure 4-29, respectively) divided by the difference in height between these two points (1829 mm) and multiplied by 100. These hysteretic results are then compared to the predicted pushover curves described in Section 5.2.1 and Appendix A. Additionally, several properties of the systems are extracted from the data, namely, initial stiffnesses, yield base shears and displacements, cumulative energy dissipation, and displacement ductility. Furthermore, the orientation and magnitude of the principal stresses and strains in the infill during linear and nonlinear of loading portions is examined and the variation of the strain magnitude and energy dissipation across the infills is investigated.

6.2　Bare Frame Test Results and Analytical Modeling

In order to estimate the contribution of the boundary frames to the experimentally obtained hysteretic behavior of the entire system, it was necessary to carry out bare frame tests (i.e. tests of the boundary frames alone without the infills). By calibrating an analytical model to those results, it becomes possible to separate, to some extent, the boundary frame contribution from the overall system behavior. The analytical model chosen is a bounding surface model with internal variables originally formulated by Dafalias and Popov (1976) and adapted by Cook (1983) and Goto *et al*. (1991) to capture the nonlinear behavior of semi-rigid beam-to-column connections (i.e. the only yielding elements in the boundary frames). This particular model enables the force to be predicted at given displacements, enabling the boundary frame's contribution to the base shear to be estimated at the displacements recorded during the testing of the infilled specimens. A summary of the model and how it is applied is given in Chen *et al*. (1996) and is briefly reviewed here.
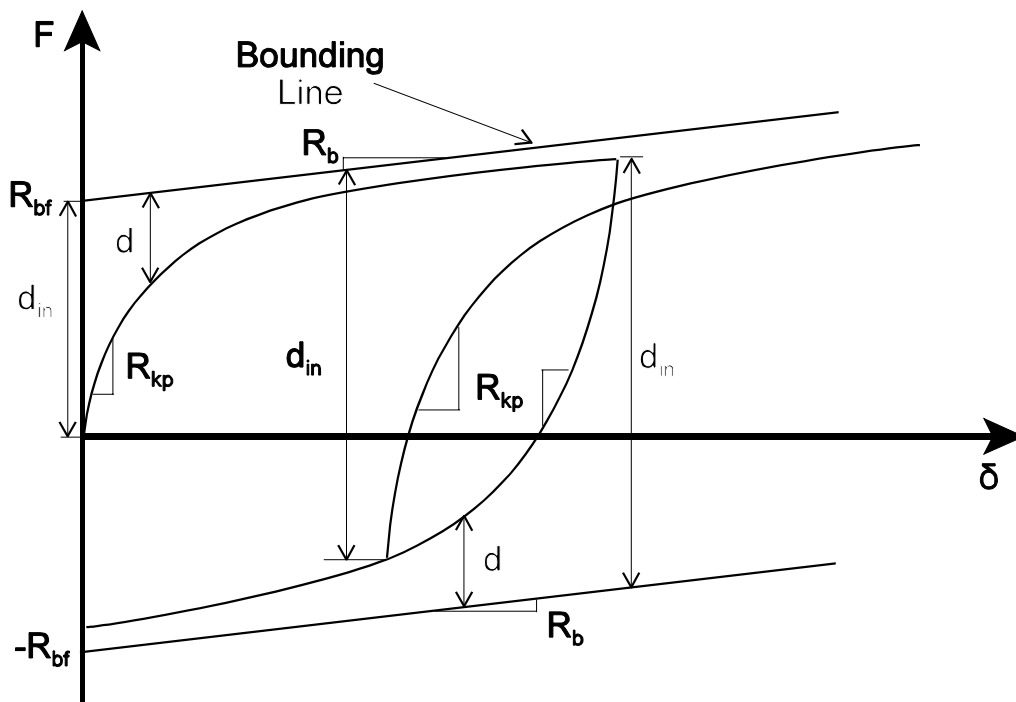
FIGURE 6-1 Bounding Surface Model with Internal Variables (Adapted from Chen *et al.,* 1996)

The bounding surface model with internal variables is defined in incremental form as either a moment-rotation or a force-displacement relationship and is shown schematically in figure 6-1. Since it is to be calibrated and used with hysteretic force-displacement curves it takes the form:

$$\Delta F = R_{kt} \, \Delta \delta \qquad (6\text{-}1)$$

where ΔF is the incremental base shear, R_{kt} is the tangent stiffness at the current displacement, and $\Delta \delta$ is the incremental displacement. The tangent stiffness at the current displacement is expressed as:

$$R_{kt} = \frac{R_{ki} R_{kp}}{R_{ki} + R_{kp}} \qquad (6\text{-}2)$$

where R_{ki} is the initial stiffness of the system and R_{kp} is the tangent plastic stiffness at a given displacement and is calculated as:

$$R_{kp} = R_b + h \left(\frac{d}{d_{in} - d} \right) \qquad (6\text{-}3)$$

where R_b is the slope of the bounding lines with force intercept R_{bf} and is calibrated to asymptotically match the largest displacement excursions in the observed results, h is a hardening parameter (used to fit the model to the experimental data), d is the distance from the current force to the corresponding bound in the direction of current loading, and d_{in} is the value of d at the initiation of loading or at every load reversal. This model is designed to provide curves that asymptotically approach specified bound lines.

It was found necessary to modify this model slightly in order to capture changes in the initial stiffness of each cycle in which the peak displacement was larger than initial yield displacement. A linear change in initial stiffness with respect to the maximum displacement of a cycle was defined as follows:

$$R_{ki} = R_{kii} \, a \left(\frac{\delta_{max}}{\delta_v} + b \right) \qquad (6\text{-}4)$$

where R_{kii} is the initial stiffness prior to any displacement reaching the yield displacement, a and b are parameters used fit the experimental data, δ_y is the initial yield displacement of the boundary frame, and δ_{max} is the maximum displacement reached during the next cycle of loading. Additionally, a limit of 2.5 times the initial stiffness (R_{kii}) was placed on R_{ki}.

Figures 6-2 and 6-3 show the experimentally obtained hystereses and the results of the application of the bounding surface model with internal variables described above, for BF1 and BF2, respectively. The values for the parameters used in each model are presented in table 6-1, along with the percent error in cumulative energy dissipated (found by numerically integrating both the experimental and modeled data). Note that in both cases the error is less than 10%. The model was implemented in MatLab (MathWorks, 1999) and the programming code is shown in Appendix B.
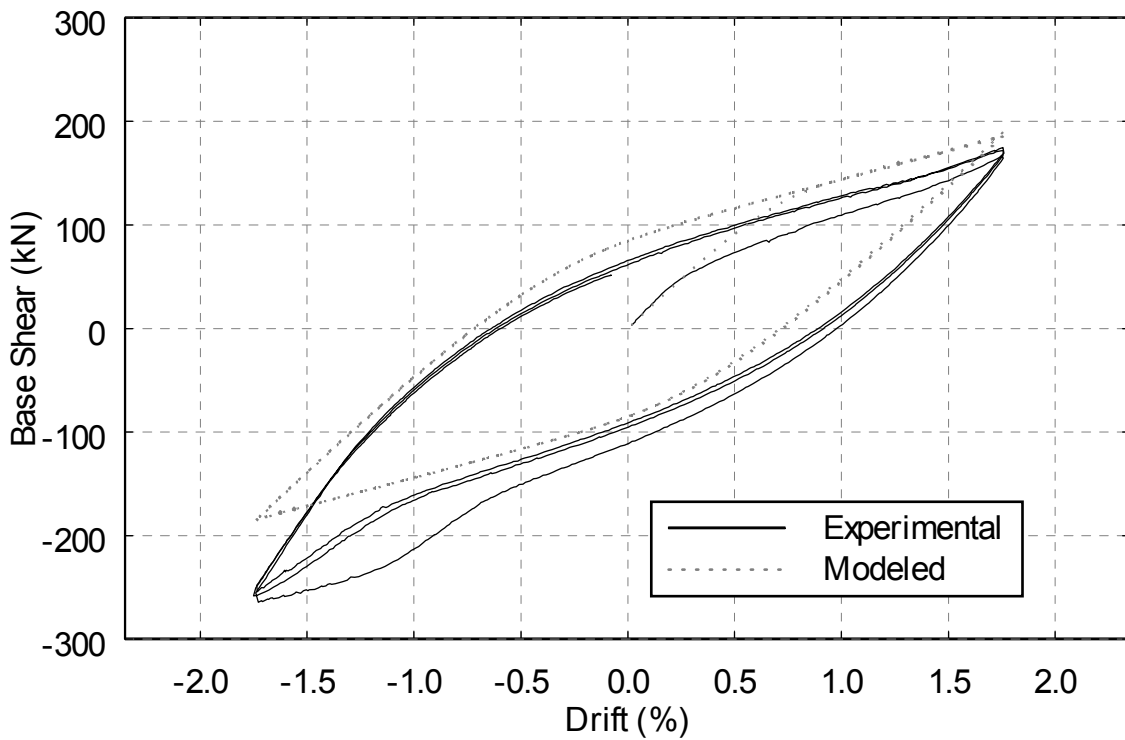
FIGURE 6-2 BF1 Hystereses
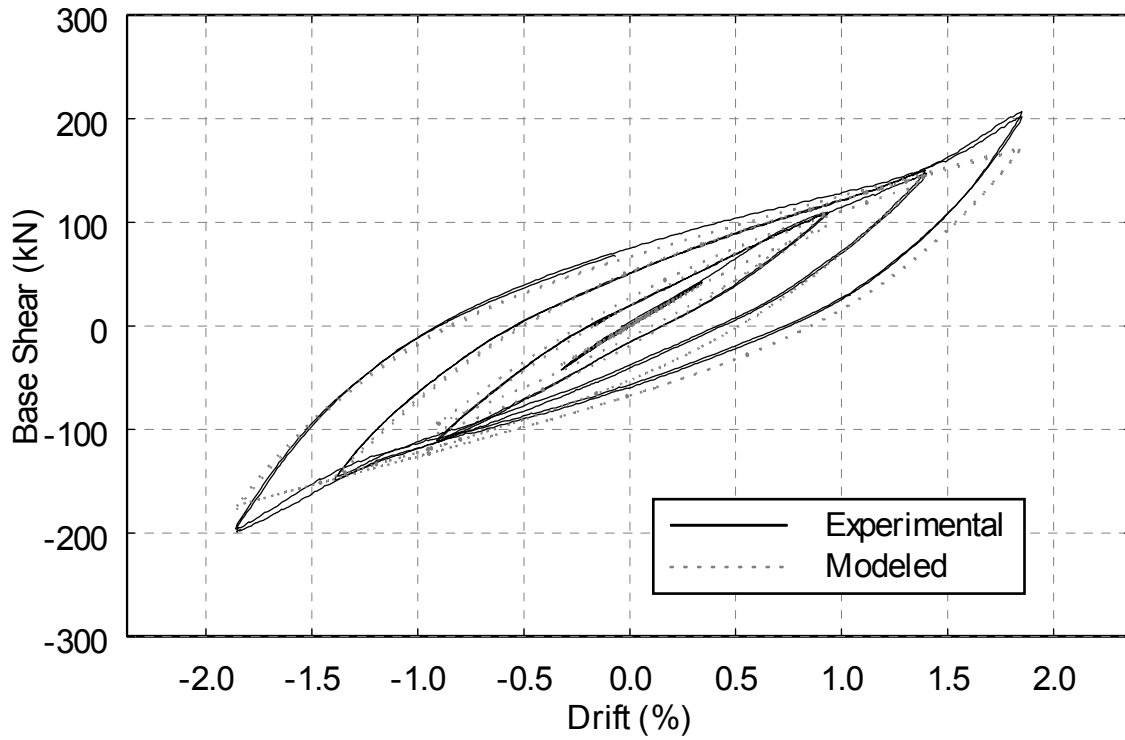
FIGURE 6-3 BF2 Hystereses

TABLE 6-1 Bounding Surface Model Parameters

Boundary Frame	R_{bf} (kN)	R_b (kN/mm)	h	R_{ki} (kN/mm)	δ_y (mm)	a	b	Error in Energy Dissipated (%)
BF1	90	3	100	10.64	13.5	0.67	0.42	9.71
BF2	75	3	25	14.46	13.5	0.67	0.42	-3.76

6.3 Experimental Results - Specimen F1

As described in Section 5, specimen F1 suffered failure of the epoxy connection between the infill and boundary frame, adjacent to the top beam. Figure 6-4 shows the force-drift loops for the entire system, and figure 6-5 shows the loops after subtracting the contribution of the boundary frame (BF1) using the model described in Section 6.2. It is apparent from the figure that there was no significant energy dissipation during the testing of specimen F1 as there is no appreciable hysteretic area. The small hysteresis like area that is visible following the first and only excursion past -0.2% drift was due to the epoxy softening and load relaxation that developed when the test was paused for visual inspection at the peak negative displacement. Upon reloading, the specimen failed at 0.17% positive drift, or 3.1 mm.
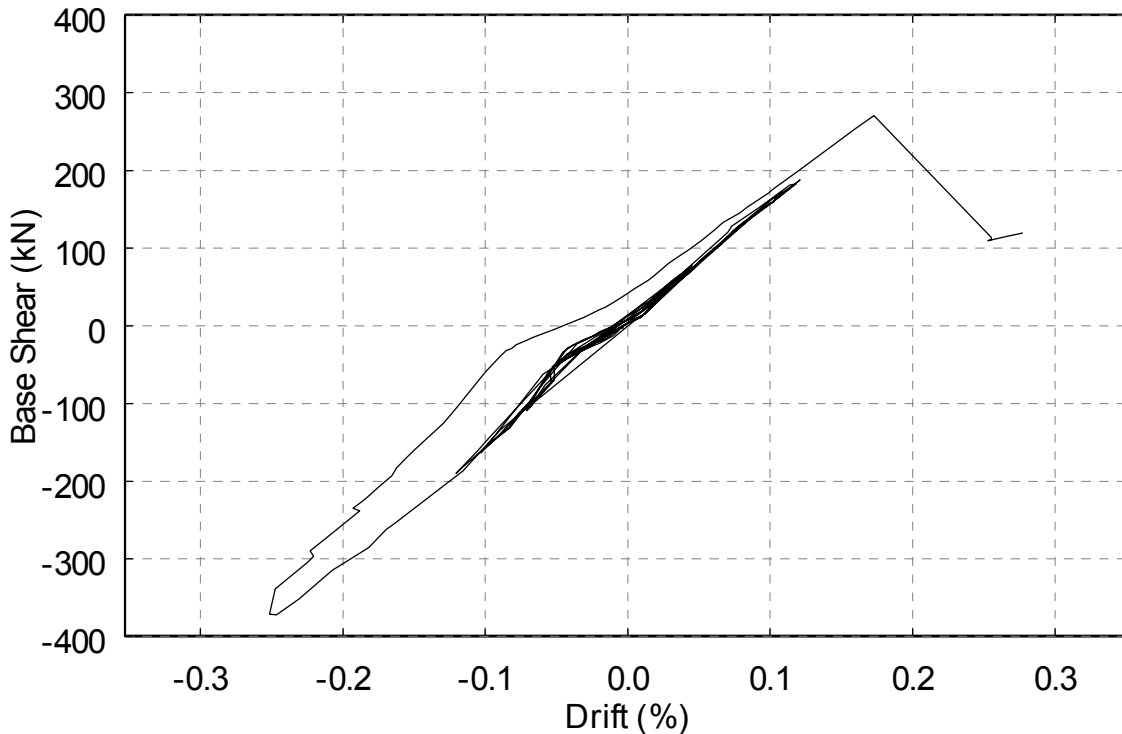
FIGURE 6-4 Specimen F1 Hysteresis (Boundary Frame and Infill)

In table 6-2 the yield displacement, yield base shear, and maximum drift are given as those corresponding to the largest negative peak. Despite the premature failure of specimen F1, this test revealed the substantial increase in stiffness provided by the light-gauge steel plate infill when compared to results obtained for the boundary frame alone. From table 6-2, the initial

stiffness of the entire system was 84 kN/mm and the initial stiffness of the infill alone was 73 kN/mm, indicating that 87% of the system's initial stiffness was provided by the infill.

TABLE 6-2 Hysteretic Properties of Test Specimens

Spec.	Total Initial Stiffness (kN/mm)	Initial Stiffness w/o BF (kN/mm)	Yield Base Shear (kN)	Yield Displacement (mm)	Maximum Drift (%)	μ	Total Energy (kN·m)	Energy- Infill Only (kN·m)
F1	84	73	372	4.6	0.25	1	NA	NA
C1	93	86	518	8	1.4	3	73	50
F2	106	96	364	5.3	3.7	12	444	212
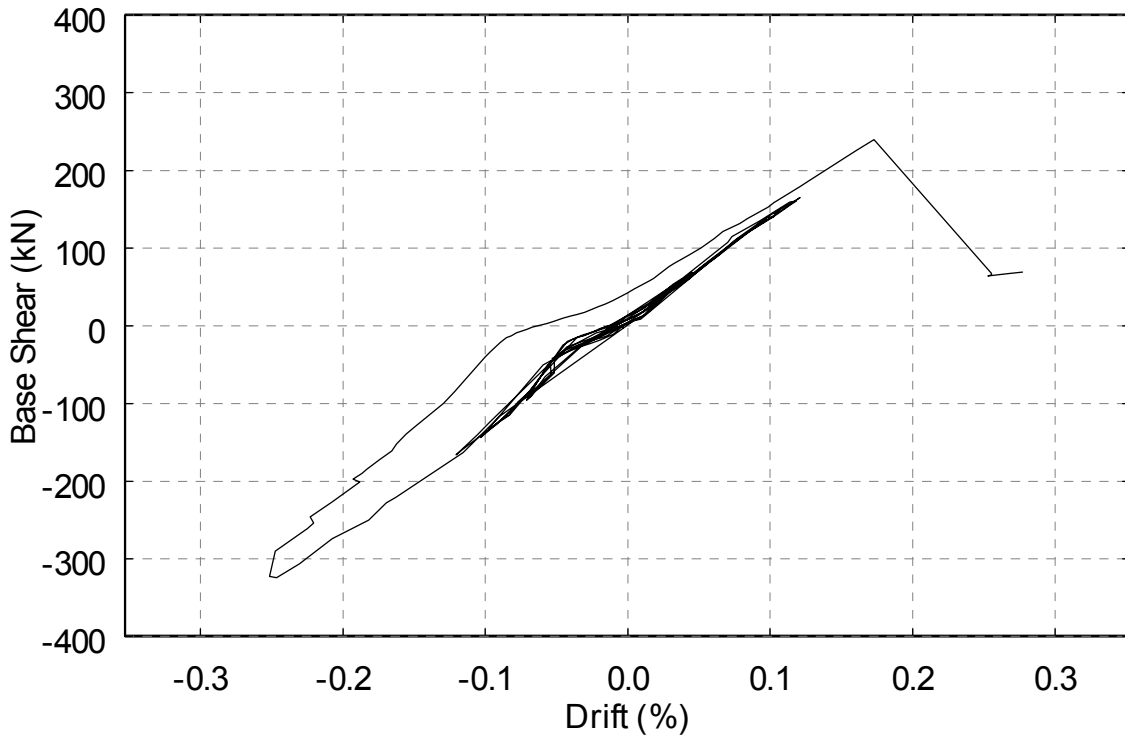
FIGURE 6-5 Specimen F1 Hysteresis (Infill Only)

Figure 6-6 shows the elastic stiffness, obtained from analysis of the strip model for this specimen, on top of the hysteretic loops for the entire system. The predicted stiffness seems to match the experimental data reasonably well, which verifies the applicability of the strip model for representing steel plate shear walls in the linear behavior range. Table 6-3 lists the magnitudes of the tensile principal strains and stresses, and their orientation with respect to vertical (α) for two different drift levels, as calculated from the strain gauges at the center of the infill. The large difference in orientation between the first and second drift levels might be attributed to the fact that part of the epoxy was failing, which could locally change the flow of stresses in the infill. The predicted orientation of the principal stresses in the infill was 45° as calculated from (2-4).

Table 6-4 gives the values of maximum axial force, P_{max}, and moment, M_{max}, as calculated from the strain gauges at the middle of the beams and columns, normalized by the axial yield force ($P_y = A_g F_y$, where A_g is the gross area of the member under consideration and F_y is the yield stress taken to be 345 MPa) and yield moment ($M_y = S F_y$, where S is the elastic section modulus of the member under consideration) respectively. It is evident that the beams and columns indeed remained elastic at these expected locations of maximum moments along the beams and columns (assuming that the moments due to frame action considering the semi-rigid beam-to-column connections are negligible). Recall from Section 4 that these frame members were designed for the maximum force output of the hydraulic actuator with a safety factor of 2.0. Furthermore, the dominating failure mechanism was prying action of the flanges of the beams and columns in the WT connection to the boundary frame (see figure 4-7). The AISC LRFD (AISC, 1998) procedure in part 11 of *The Manual of Steel Construction* was used to check prying action and the parameter α (which controls the degree of prying action allowed) in that procedure was set to zero to insure that no prying action would occur. This resulted in large boundary frame members, which explains the fact that the combined stresses did not exceed 6% in this case. Based on the results in table 6-4 these requirements could be relaxed in the future.
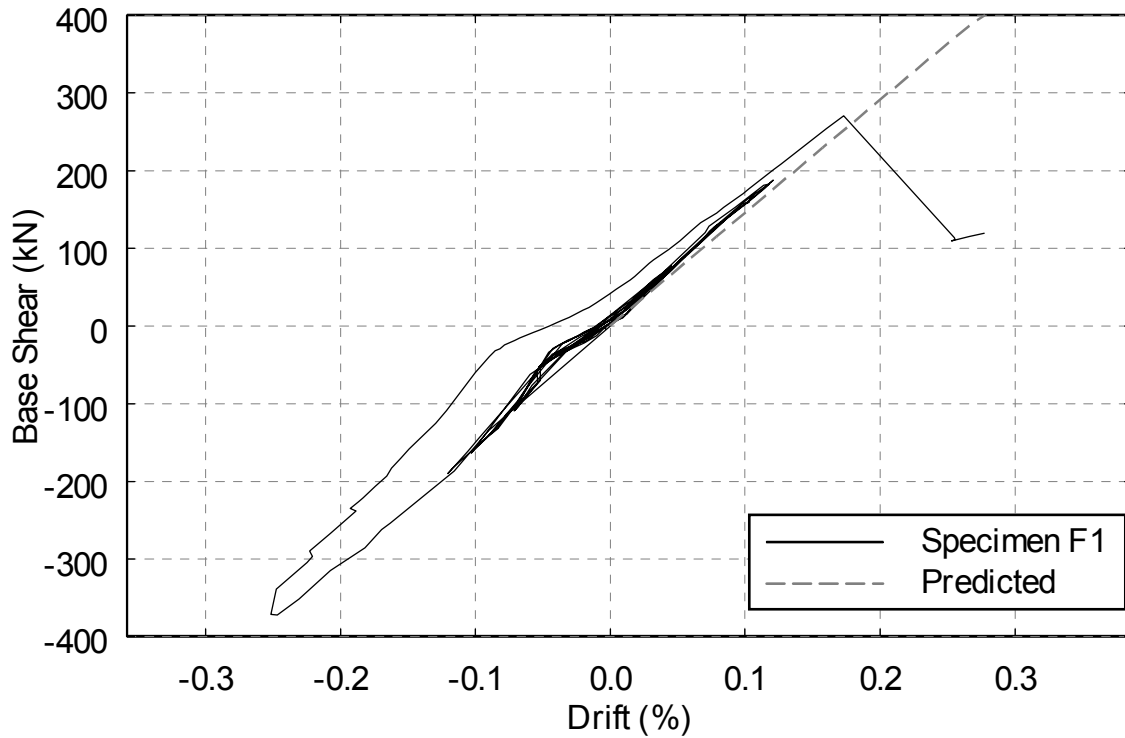
FIGURE 6-6 Experimental Hysteresis and Predicted Pushover Curve - Specimen F1

TABLE 6-3 Principle Directions, Strains and Stresses for Test Specimens

Specimen	Drift (%)	α (∘)[1]	Principle Strain (mm/mm)	Principle Stress (MPa)
F1	0.06	48	0.00025	50.6
	-0.07	-51	0.00031	61.6
	0.12	62	0.00063	126.0
	-0.12	-46	0.00059	117.0
C1	0.08	61	0.00042	82.8
	0.19	60	0.00097	193.0
	0.31	55	0.00148	296.0
F2	0.07	46	0.00033	66.8
	-0.07	-49	0.00040	79.6
	0.18	56	0.00100	204.0
	-0.18	-54	0.00111	222.0

TABLE 6-4 Normalized Maximum Beam and Column Actions

Specimen	Beam P_{max}/P_y (%)	Beam M_{max}/M_y (%)	Column P_{max}/P_y (%)	Column M_{max}/M_y (%)
F1	2.3	3.1	1.4	0.8
C1	11.6	15.6	7.8	5.9
F2	6.5	7.0	2.6	3.5

6.4 Experimental Results - Specimen C1

Figure 6-7 shows the force-drift hysteresis curves for specimen C1 and BF2 (modeled as per the procedure described in Section 6.2). As expected, the hysteresis for specimen C1 is one-sided because tension field action only occurred when the corrugations were in tension. The rapid degradation in strength observed following the cycles at $3\delta_y$ (1.4% drift) was due the severe local buckling that developed during negative loading, as described in Section 5. Figure 6-8 shows the hysteresis after the subtraction of the boundary frame contribution. This illustrates the substantial hysteretic energy dissipated by the infill alone, both in tension, and to some degree during the early cycles, in compression. Although pinching in the curves is evident, the infill contributed significantly to the energy dissipation capability of the system. Table 6-2 shows that more than 67% of the total energy dissipated during the test was dissipated by the infill versus 33% for the boundary frame. Furthermore, a displacement ductility ratio (μ), (defined as the maximum displacement over the yield displacement) of three was achieved as the strength of the system was 91% of the maximum strength achieved, of which approximately 74% was taken by the infill and 26% by the boundary frame. At a ductility ratio of two the specimen achieved its maximum strength of 633 kN of which approximately 80% was the contribution of the infill and 20% the contribution of the boundary frame. Also apparent from the data in table 6-2, the contribution of the infill to the initial stiffness of the specimen was over 90%.
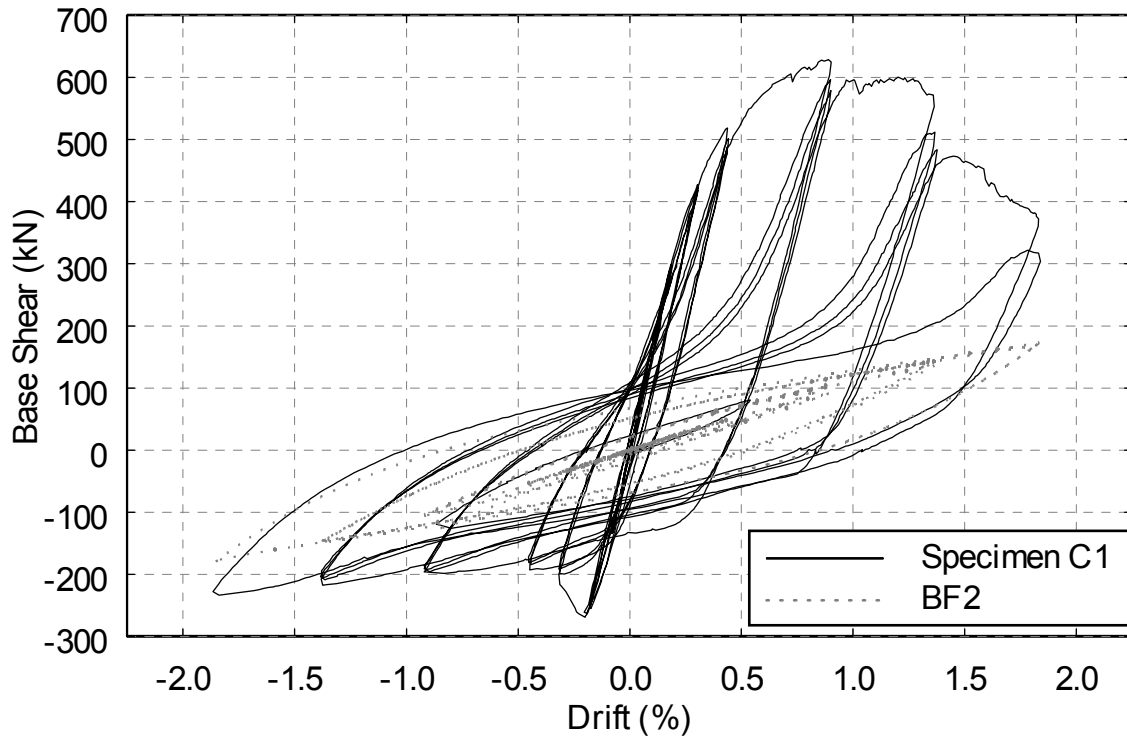
FIGURE 6-7 Specimen C1 and Modeled BF2 Hystereses
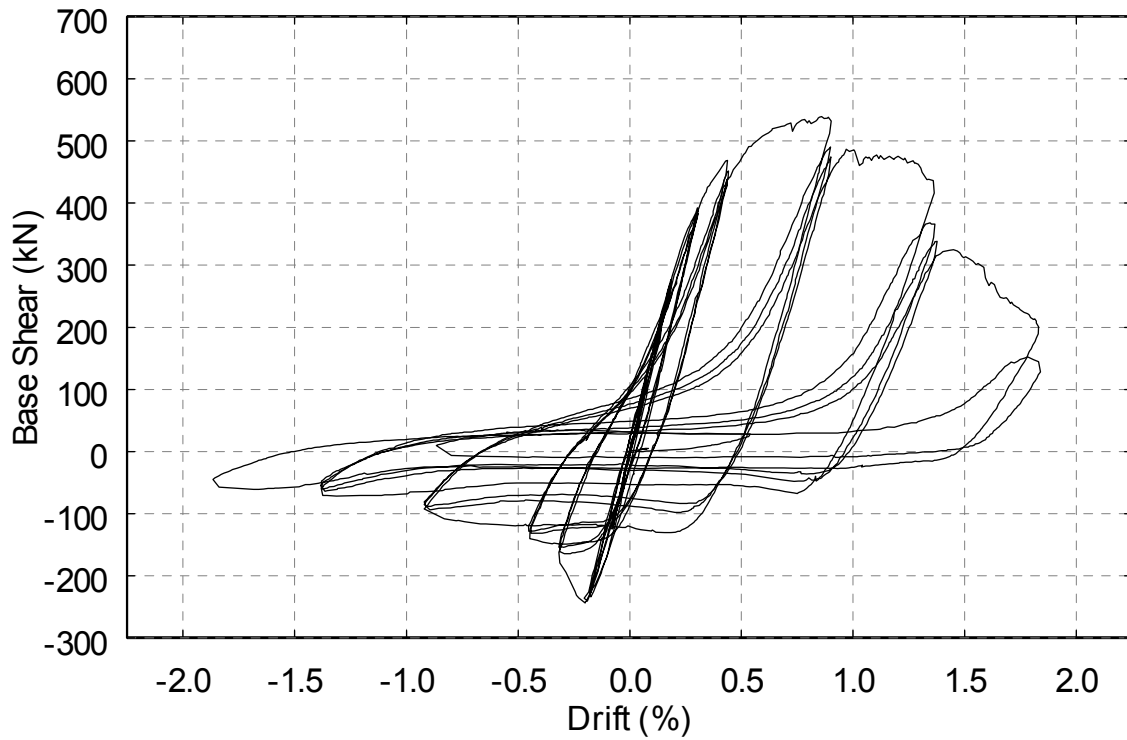
FIGURE 6-8 Specimen C1 Hysteresis (Infill Only)

Figure 6-9 shows the hysteresis loops for specimen C1 with the predicted pushover curve, calculated as described in Appendix A, superimposed. The initial stiffness agrees reasonably well while the yield base shear is approximately 15% over-predicted and the ultimate base shear is about 5% over-predicted. This could possibly be caused by the epoxy in the infill-to-boundary frame connection failing in an unquantifiable manner.
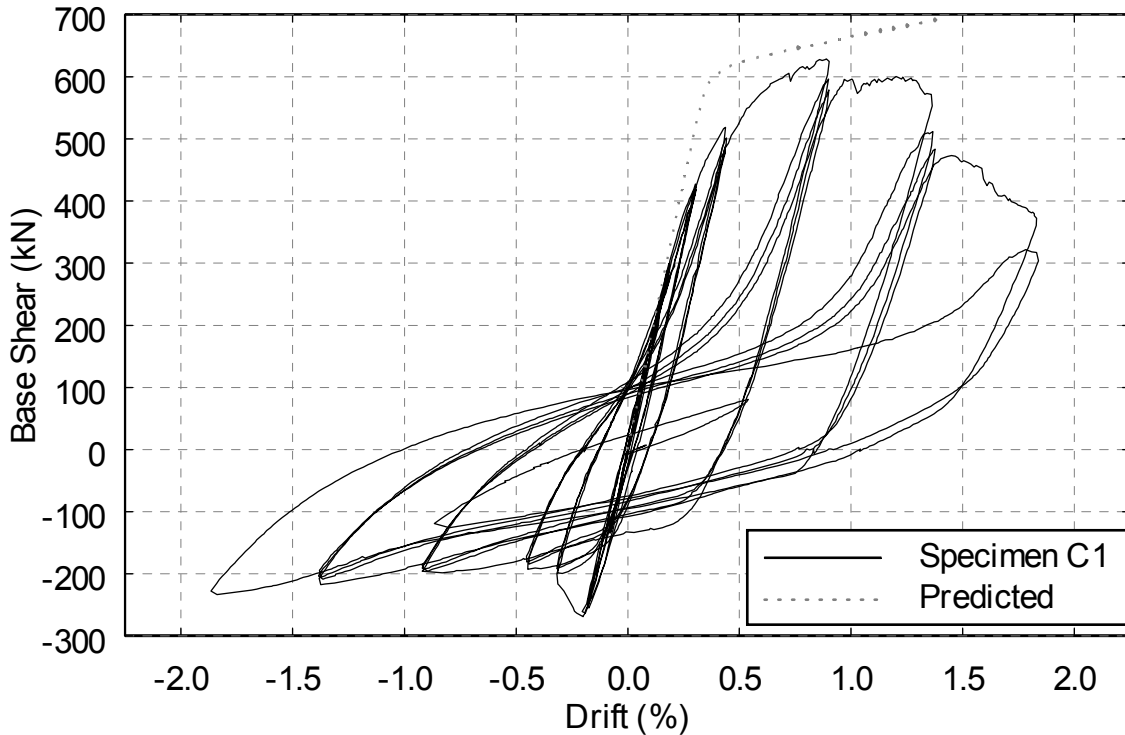
FIGURE 6-9 Experimental Hysteresis and Predicted Pushover Curve -

Specimen C1

Figure 6-10 shows the variation in strain measurements across the infill of specimen C1 to a drift of just under 0.75%, after which several gauges began to fail (for example, PW14 failed at 0.5% drift, PW11 failed at 0.85% drift, and PW4 failed at 1.0% drift). The data in this plot is from the strain gauges shown in figure 4-31, which are located on large and small sections of corrugations (the data plotted on the upper half of figure 6-10 are from gauges on the larger sections of the corrugations and the data plotted on the lower half of the figure are from gauges on the smaller sections of corrugations) orientated at 45° from horizontal. There does not seem to be an appreciable variation in strain across the infill with the exception of gauges PW13 and PW16, which were mounted on sections of corrugation in which the epoxy connection between the infill

134

and boundary frame failed causing the strains at these locations to be considerably less than at other locations. Additionally, there is not a significant variation in strain when comparing the gauges attached to larger corrugations with the gauges attached to smaller corrugations. The strain histories are easily explained with the aid of the schematic in figure 6-11. Segment 1 of this figure (i to j) indicates elastic cycles prior to local buckling and the first excursion to a positive drift level that, upon load reversal, will cause local buckling (j to k). Segment 2 (k to l) indicates the first occurrence of local buckling of the corrugation for which the gauge is attached as loading in the negative direction is carried out. Segment 3 (l to j) shows the beginning of reloading in the positive direction which simply removes the local buckling without increasing the strain and segment 4 (j to k to m) shows the next increase in strain as tension begins to reform in the corrugation. Figure 6-12 shows the base shear versus the strain in the same gauges as those shown in figure 6-10. From figures 6-10 and 6-12, it is apparent that as long the epoxy was effective in transferring load from the infill to the boundary frame, the energy dissipation was relatively uniform over the entire infill. Similar figures showing the data from gauges mounted on the east side of specimen C1 (as shown in figure 4-32) are given in Appendix C.

From the data obtained from the strain gauges at the center of the infill (PW7, PW8, PW9, PE7, PE8, and PE9 in figures 4-31 and 4-32) the first principal strains, first principal stresses, and their orientation with respect to vertical (α), were calculated and are shown in table 6-3 for the cycles prior to yielding of the infill. At the three elastic drift levels reached, the orientation was substantially different than the 45° calculated using (2-4). The possible error in the experimental results due to affixing the gauges to the plate is approximately 10% and it is also possible that epoxy failure in certain locations could have contributed to the difference between the predicted and experimental orientations. However, as described above, the predicted pushover curve for the specimen (which is based primarily on the strip model with α calculated by (2-4)) matched reasonably with experimental results. This could be attributed to the fact that the behavior of the strip model is not sensitive to changes in α between the range of 45° and 50°, and for thinner plates that range may be even wider (Driver, et al. 1997 and Rezai, 1999).
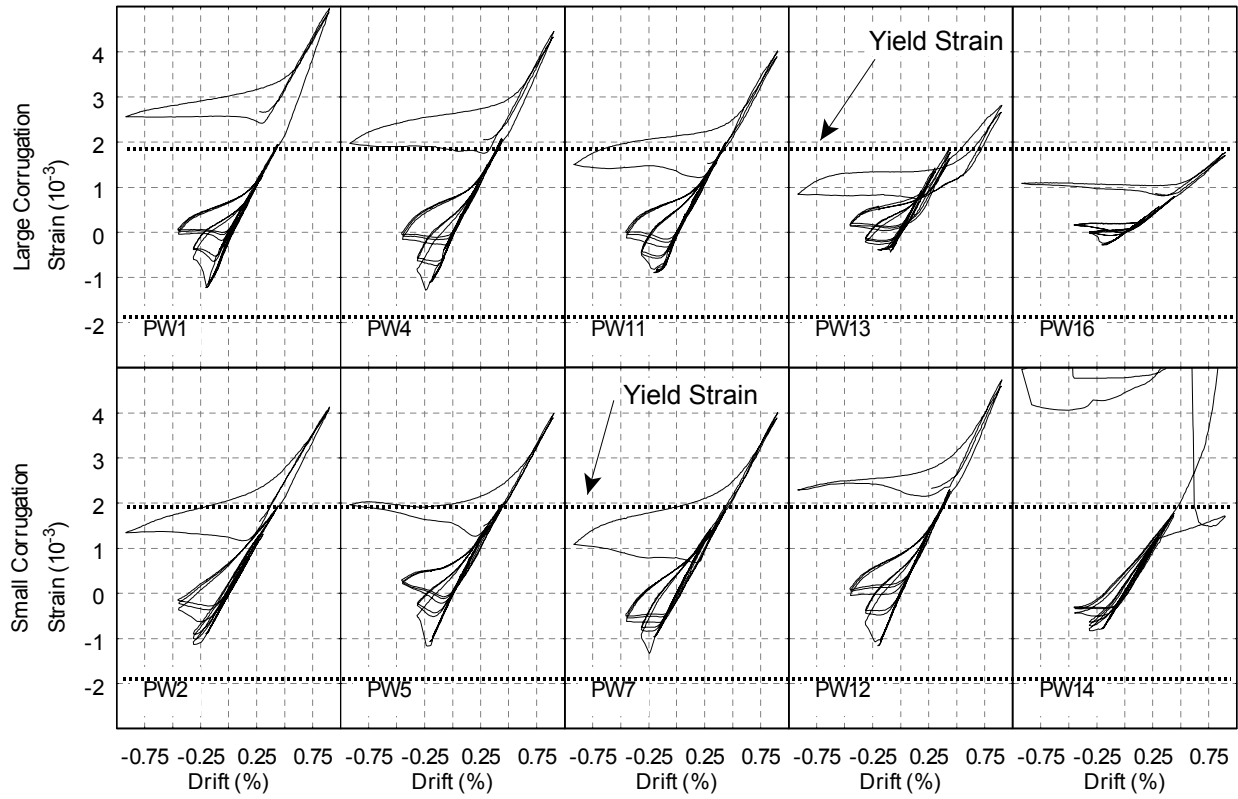
FIGURE 6-10 Variation of Strain Across Infill

Specimen C1 - Data Truncated at Cycle 14 ($2\delta_y$)
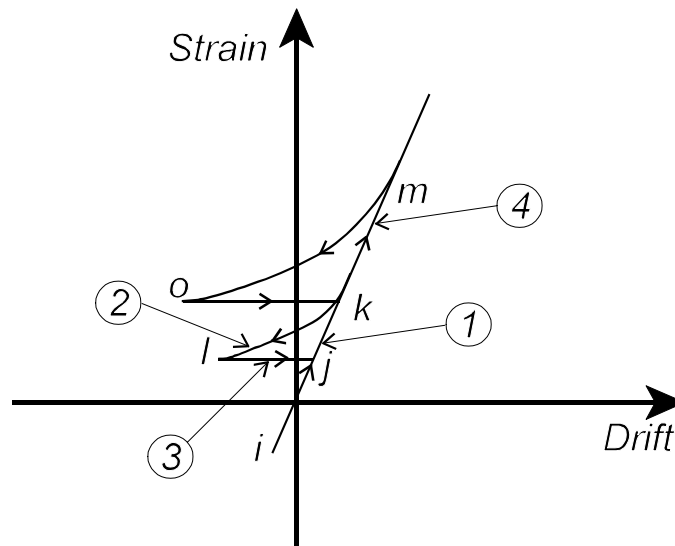
FIGURE 6-11 Schematic of Strain Histories

From table 6-4 it is again evident that the beams and columns remained well within the elastic range of behavior during the testing of specimen C1. This indicates that the goal of minimizing the demand on the boundary frame members was realized, which was also the goal of the prototype seismic retrofit designs for the MCEER Demonstration Hospital.
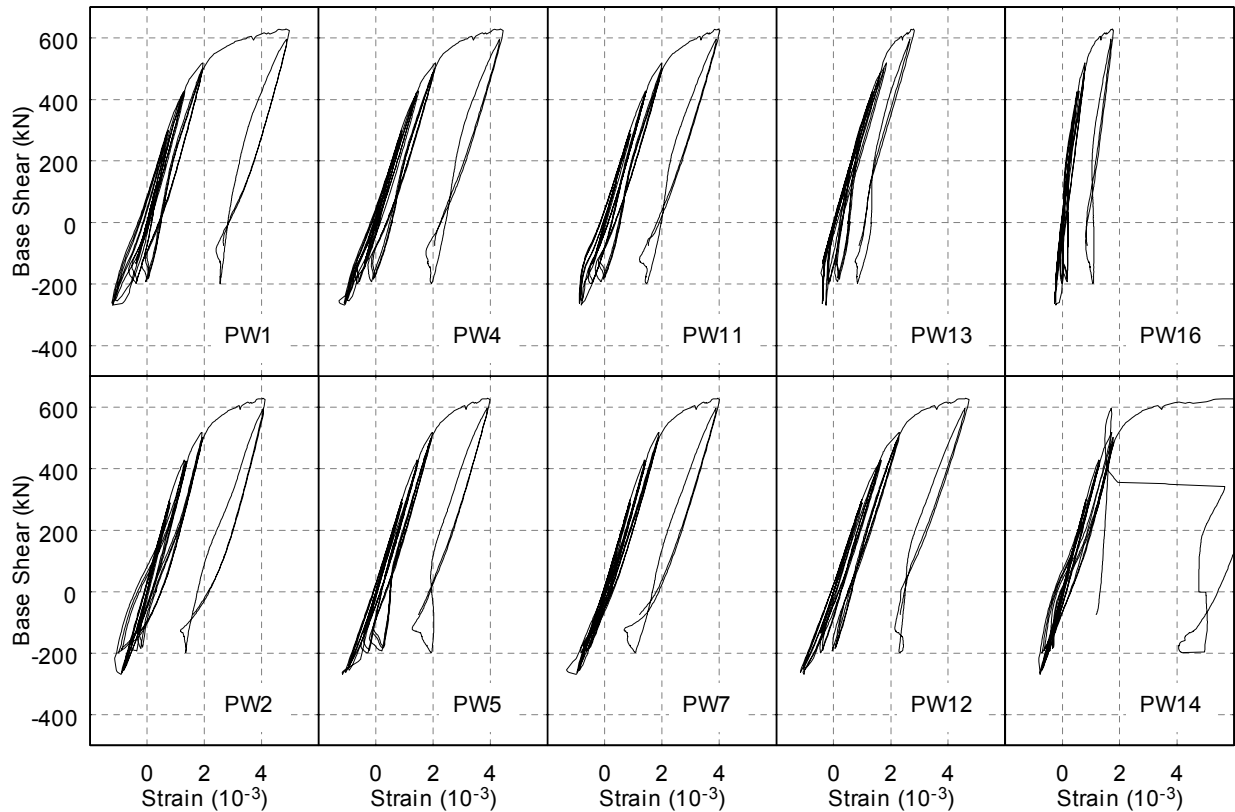
FIGURE 6-12 Base Shear Versus Strain Across Infill

Specimen C1 - Data Truncated at Cycle 14 ($2\delta_y$)

6.5   Experimental Results - Specimen F2

The hysteresis for specimen F2 is shown in figure 6-13 superimposed with the hysteresis of BF1 modeled as described in Section 6.2. The behavior of specimen F2 was ductile and stable up to large drift levels, although significant pinching is apparent in the hysteretic loops. The modeled BF1 hysteresis fits within the loops for specimen F2, but seems to somewhat underestimate the contribution of the bare frame. Nonetheless, figure 6-14 is generated to show an estimate of the hysteresis of the infill alone, i.e., after subtracting BF1's contribution. The figure shows some erroneous results around zero base shear due to the imperfections in the boundary frame model.
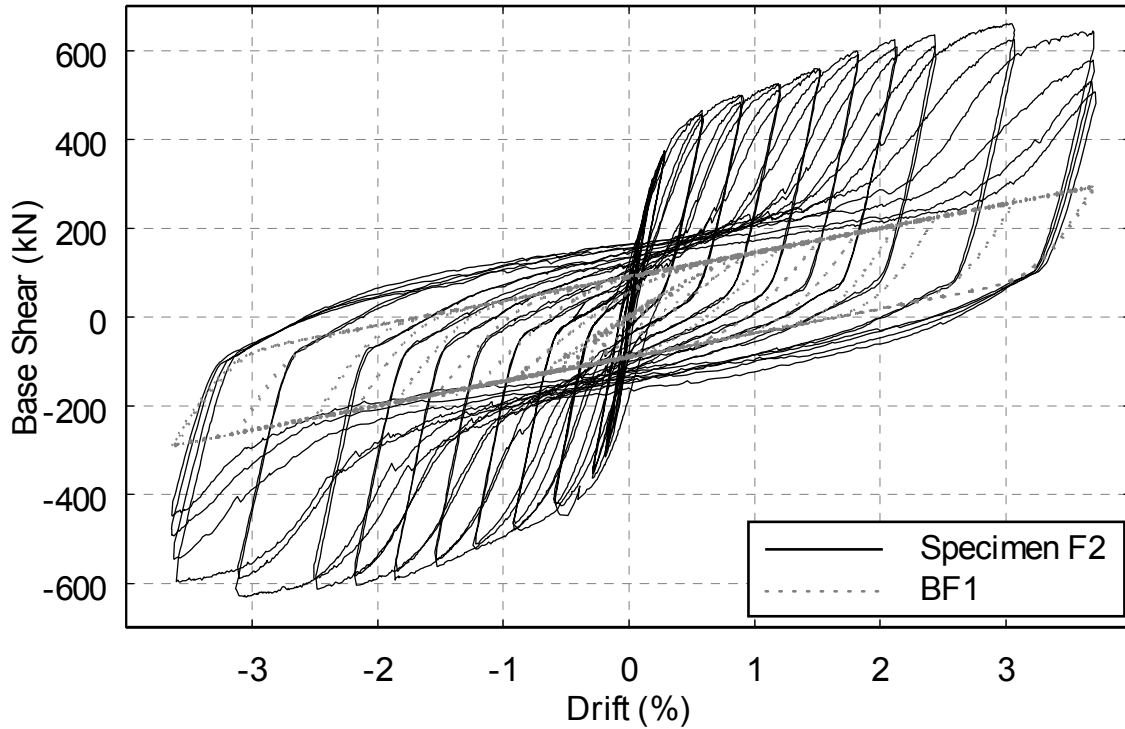
FIGURE 6-13 Specimen F2 and Modeled BF1 Hystereses
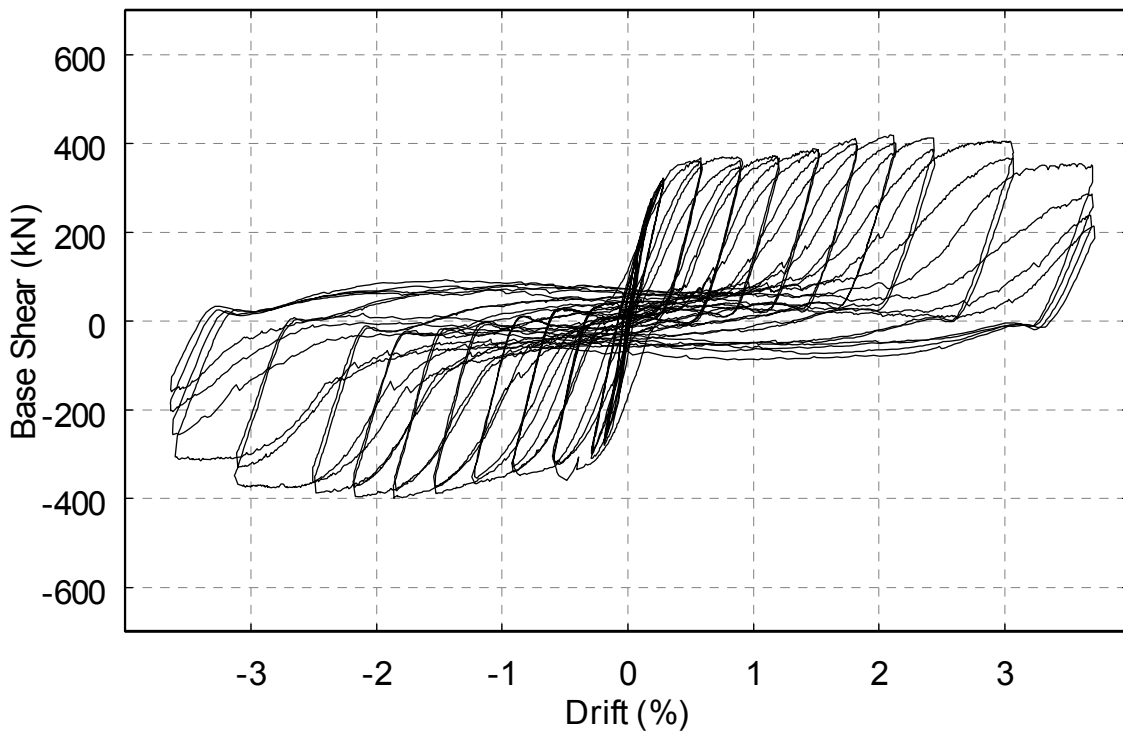
FIGURE 6-14 Specimen F2 Hysteresis (Infill Only)

138

However, the results of figure 6-14 resemble that for the behavior braces with large slenderness, i.e. with near zero stiffness following unloading in a given cycle until the tension field develops in the other direction (Bruneau *et al.* 1997).

Table 6-2 shows that 90% of the initial stiffness of the system is due to the contribution of the infill. The system reached a displacement ductility of 12, which is large for any type of wall system. This corresponded to a maximum drift of 3.7%, which typically exceeds what would be practically expected during a seismic event for such a stiff structural system. Also of interest in table 6-2 is the substantial amount of energy dissipated by the infill. It should be noted that during the final three cycles at 3.7% drift, the boundary frame contributed more to the total cumulative energy dissipation than the infill. This is because the frame still provides full hysteretic loops at large drifts while the infill suffers fractures in the corners and progressively dissipates less energy at each large drift cycle. This is illustrated in figure 6-15 where it can be seen that for earlier cycles more energy is dissipated by the infill while at a large number of cycles (and displacement of $8\delta_y$) the boundary frame catches up.
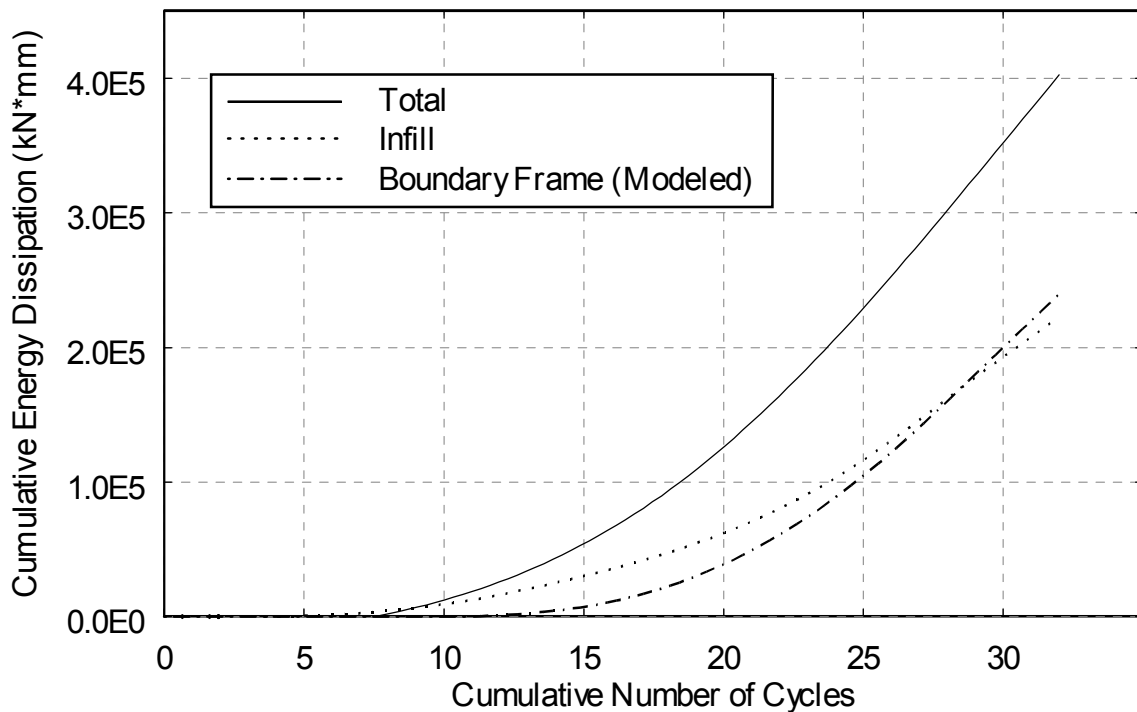
FIGURE 6-15 Cumulative Energy Dissipation By Component - Specimen F2

139

Figure 6-16 shows the predicted pushover curve (as described in Appendix A) superimposed on the hysteresis curves of specimen F2. Reasonable agreement (considering the simplicity of the strip model) with respect to initial stiffness, secondary stiffness, and yield base shear is evident although the ultimate base shear is somewhat under-predicted. These results show the adequacy of the strip model for serving as a simple representation of light-gauge steel plate shear walls. As table 6-3 reveals the orientation of the principal stresses at the center of the infill during elastic cycles is different than the 45° calculated via (2-4). However, from the figures of Section 5, which show the buckling of the infill, it is visible from square grid painted on the infill that the buckling lines are forming at approximately 45° at drifts larger than yield, which indicates that the tension field is indeed forming at that angle. The orientations reported in table 6-3 contain an error of up to 10% that stems from the placement of the strain gauges.
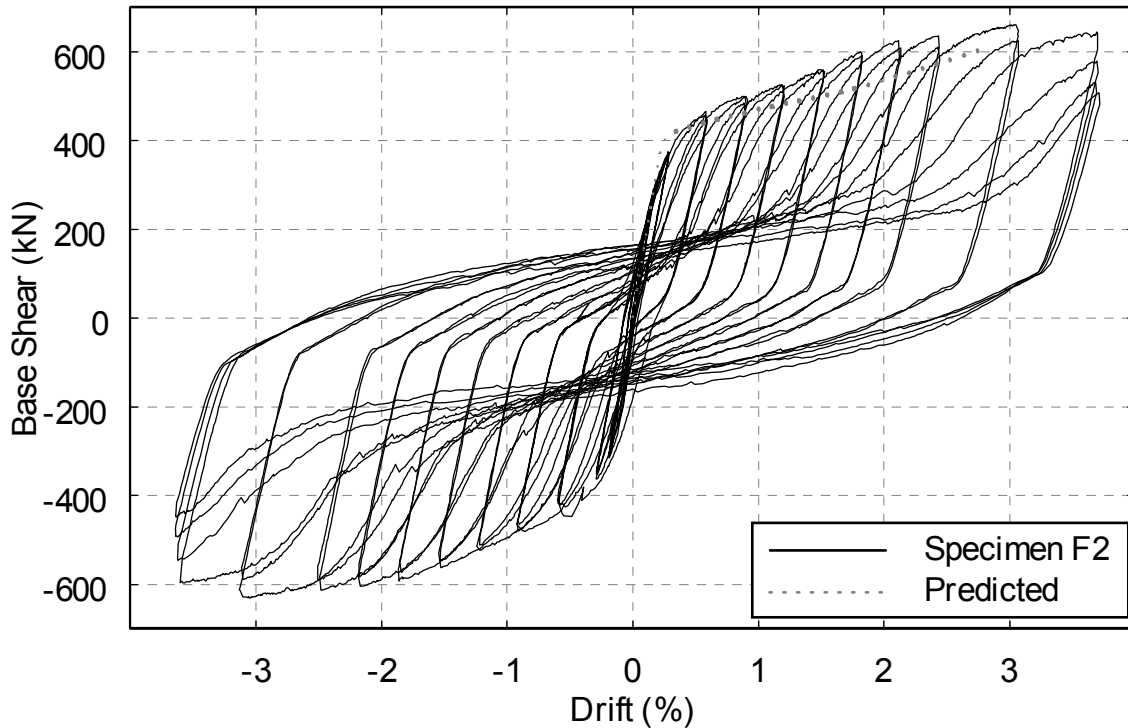
FIGURE 6-16 Experimental Hysteresis and Predicted Pushover Curve

Specimen F2

Figures 6-17 and 6-18 show the strain distribution across the infill in a manner similar to figures 6-10 and 6-12 for specimen C1. Figure 4- 29 shows the locations of the strain gauges that produced this data; the gauges at the top of figures 6-17 and 6-18 are oriented to record tension strain when the specimen is loaded toward the positive direction (north) and the gauges at the

bottom are oriented to do the same when the specimen is loaded toward the negative direction (south). All gauges are oriented at 45° from the horizontal. The same type of behavior as that explained previously with figure 6-11 is evident, with the exception that segment 2 is caused by the buckling of the entire infill as shown in the photos of Section 5, as opposed to the local buckling of corrugations as for specimen C1. This is the mechanism which produces the pinched hysteretic behavior that both specimens C1 and F2 displayed. It is also evident that the strain is fairly uniform across the infill indicating that the entire plate participated in dissipating energy. Data from gauges mounted on the east side of specimen F2 is given in Appendix C.
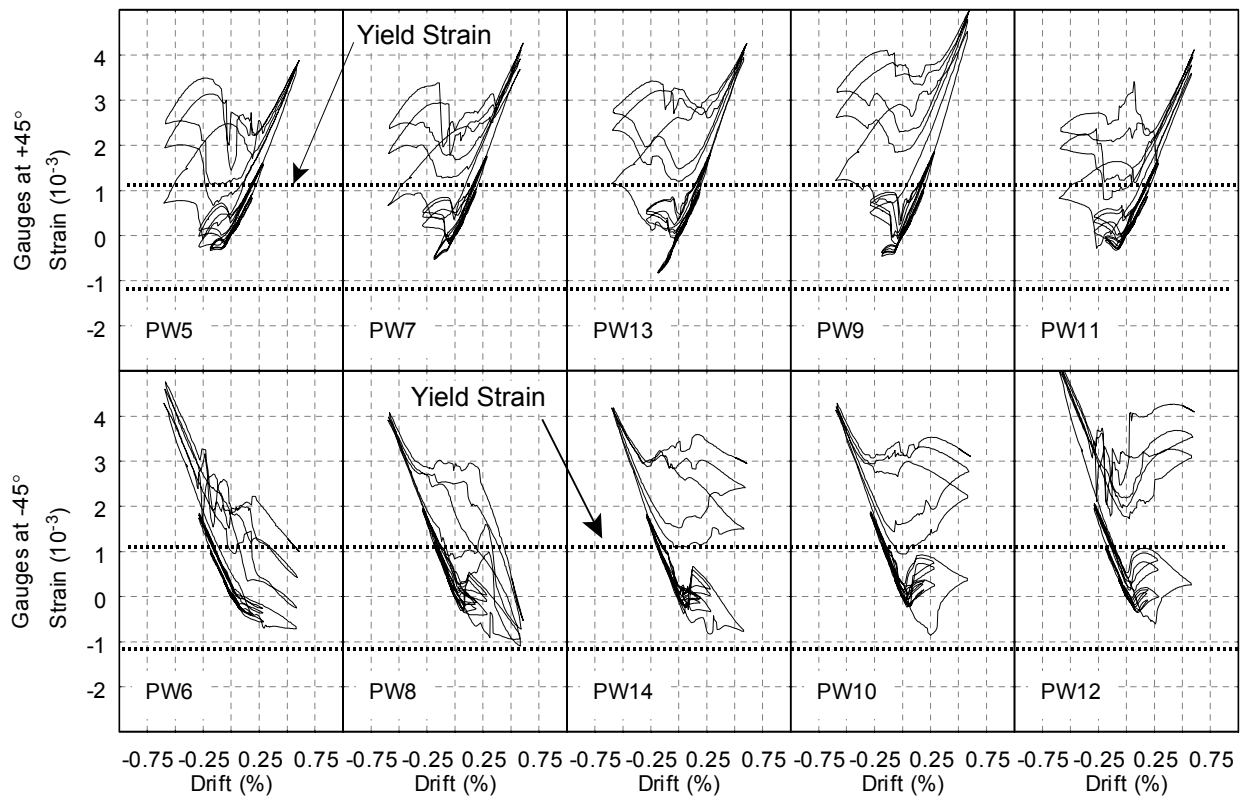
FIGURE 6-17 Variation of Strain Across Infill

Specimen F2 - Data Truncated at Cycle 12 ($2\delta_y$)
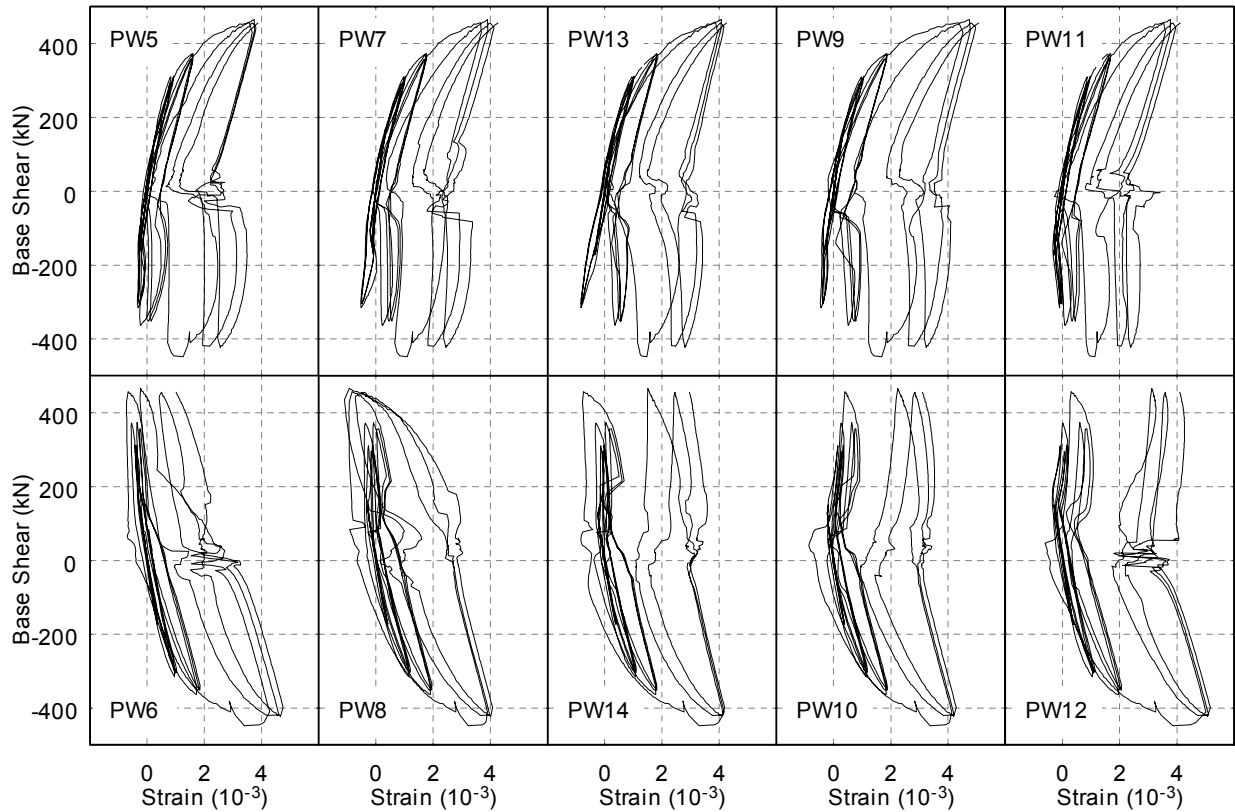
FIGURE 6-18 Base Shear Versus Strain Across Infill

Specimen F2 - Data Truncated at Cycle 12 ($2\delta_y$)

6.6   Summary

Despite its premature failure, specimen F1 provided some insight into the adequacy of the strip model for predicting the initial stiffness of light-gauge steel plate shear walls. It also demonstrated the difficulty in obtaining reliable epoxied connections for the selected design scheme.

Specimen C1 performed well and dissipated significant hysteretic energy while providing stable, albeit pinched, hysteretic behavior up to a displacement ductility of 3. The adequacy of the strip model to predict initial stiffness and ultimate strength was observed when compared to the experimental results for specimen C1. The strain across the infill was found to vary insignificantly across the width of the wall, meaning that the entire infill was active in dissipating energy and that yielding of the infill occurred simultaneously at all instrumented locations. Additionally, in this case, an epoxy connection proved adequate to connect the corrugated infill

142

to the boundary frame, allowing the specimen to reach its ultimate failure by fracture of the infill at locations of repeated local buckling.

By far the most desirable behavior was achieved by specimen F2, as evidenced by the significant hysteretic energy dissipated and the large displacement ductility reached. The adequacy of the strip model was again observed. Examination of data from the strain gauges mounted on the infill showed that the entire plate contributed to the energy dissipation and that yielding over the entire plate occurred simultaneously. In addition to the superior hysteretic behavior of F2, compared to C1, it is also the simplest to construct of the specimens considered.

In all three tests, the initial stiffness of the system was found to be largely due to the infills. Additionally, the beams and columns of the boundary frame remained, as designed, well within the limits of elastic behavior.

SECTION 7

CONCLUSIONS

7.1 General

In this study, plastic analysis has been used to develop a design procedure for steel plate shear walls allowed to buckle in shear and form a diagonal tension field to resist lateral loads. Using the strip model, presented in CAN/CSA-S16-01, as the mathematical representation for several steel plate shear wall configurations, fundamental plastic collapse mechanisms have been derived. The proposed design procedure was formulated from the simplest of configurations and shown to be conservative for the more complex ones. Additionally, in some cases, the design procedure which currently appears in CAN/CSA-S16-01 was found to result in unconservative designs. It is recommended that either the design procedure proposed in this report be used, or that modifications to the current procedure, as presented in Section 3, be made to avoid the possibility of unconservative designs.

Three light-gauge steel plate shear wall specimens were then designed and tested using quasi-static loading. Two of the specimens utilized flat infill plates, one with an epoxy connection to the boundary frame and one with a welded connection, while the third was designed with a corrugated infill plate and also utilized an epoxy connection to the boundary frame. Specimen design was based on prototype light-gauge steel plate shear walls, which themselves were designed to be seismic retrofit options for the MCEER Demonstration Hospital. Two of the three specimens were shown to achieve the goals of increasing the stiffness, energy dissipation capability, and ductility of the existing framing, while providing movability of the infills through the use of intermediate bolted connections. Additionally, it was shown that the infills were effective in limiting strength demands on the boundary framing as they remained well within the elastic range of behavior during testing.

145

From the experimental results it was shown that the entire infill of the light-gauge steel plate shear wall specimens participated in dissipating energy. Though the hysteretic curves of the specimens were pinched, they were stable and provided significant energy dissipation in the cases of the specimens with the corrugated infill and the flat infill in which the welded connection was used. Furthermore, the adequacy of the strip model in predicting the monotonic behavior of light-gauge steel plate shear walls into the nonlinear range was found to be acceptable through comparison with the experimental results.

The ultimate failure mode of the specimen which utilized a corrugated infill was found to be fracture of the infill at locations of repeated local buckling and an industrial strength epoxy was found to be an adequate material to connect the infill to the boundary frame in this case. For the specimen using the flat infill and an epoxy connection to the boundary frame, failure occurred in the epoxy prior to yielding of the infill. The specimen utilizing a flat infill and a welded connection to the boundary frame was significantly more ductile than the other two and failure was the result of fractures in the infill adjacent to the fillet weld used to connect the infill to the boundary frame. Despite these fractures near the welded connection, which appeared in the early stages of the test, this specimen did not suffer a significant loss of strength until 12 times the yield displacement.

7.2 Recommendations for Further Research

Other means of limiting the demands induced on existing framing by seismic retrofit schemes utilizing steel plate shear walls are possible. The use of low yield stress steels, and infills that do not occupy the entire bay are two possibly viable options. Additionally, different infill connection alternatives should be explored with the use of light-gauge steel plate shear walls.

The adequacy of the strip model in predicting the behavior of steel plate shear walls that have aspect ratios (L/h) of less than unity remains a subject that warrants investigation. Furthermore, experimental studies on multistory steel plate shear walls that could develop soft-story failure mechanisms should be performed, and their results compared to the plastic analysis results for those types of walls presented in this study.

SECTION 8

REFERENCES

ACI (1995), *Building Code Requirements for Structural Concrete and Commentary*, American Concrete Institute, Detroit, MI.

AISC (1998), *Manual of Steel Construction - Load and Resistance Factor Design*, American Institute of Steel Construction, Washington, D.C.

ASTM (1997), "Standard Specification for Commercial Steel Sheet, Carbon, Cold-Rolled", A 366/A 336M-97, American Society for Testing and Materials, Philadelphia, PA.

ASTM (1998), "Standard Specification for Steel Sheet, Zinc-Coated (Galvanized) Zinc-Iron Alloy-Coated (Galvannealed) by the Hot-Dip Process", A 653/A 653M-98, American Society for Testing and Materials, Philadelphia, PA.

ATC (1992), *Guidelines for Seismic Testing of Components of Steel Structures*, Applied Technology Council, Report 24.

Basler, K., (1961), "Strength of Plate Girders in Shear", *Journal of the Structural Division*, ASCE, Vol. 87, No. 7, pp. 150-180.

Bruneau, M.,Uang, C.M., and Whittaker, A. (1997), *Ductile Design of Steel Structures*, McGraw-Hill, Inc., New York, NY.

Caccese, V., Elgaaly, M., and Chen, R., (1993), "Experimental Study of Thin Steel-Plate Shear Walls Under Cyclic Load", *Journal of Structural Engineering*, ASCE, Vol. 119, No. 2, Feb. 1993, pp. 573-587.

Chen, W.F., Goto, Y., and Liew, J.Y.R, (1996), *Stability Design of Semi-Rigid Frames*, John Wiley & Sons, Inc., New York, NY.

Cook, N.E., (1983), "Strength of Flexibly-Connected Steel Frames Under Load-Histories," Ph.D. Dissertation, University of Colorado-Boulder, Boulder, CO.

CSA, (1978), "Steel Structures for Buildings - Limit States Design", CAN/CSA S16.1-M78, Canadian Standards Association, Willowdale, Ontario, Canada.

CSA, (1994), "Limit States Design of Steel Structures", CAN/CSA S16.1-94, Canadian Standards Association, Willowdale, Ontario, Canada.

CSA, (2001), "Limit States Design of Steel Structures", CAN/CSA S16-01, Canadian Standards Association, Willowdale, Ontario, Canada.

CSI, (1997), "SAP2000 Reference Manual", Computers and Structures, Inc., Berkeley, CA.

Dafalias, Y.F., and Popov, E.P., (1976), "Plastic Internal Variables Formalism of Cyclic Plasticity", *Journal of Applied Mechanics*, ASCE, Vol. 43, pp. 645-651.

Driver, R.G., Kulak, G.L., Kennedy, D.J.L., and Elwi, A.E. (1997), "Seismic Behavior of Steel Plate Shear Walls", Structural Engineering Report No. 215, Department of Civil Engineering, University of Alberta, Edmonton, Alberta, Canada.

Elgaaly, M., Caccese, V., and Du, C. (1993), "Postbuckling Behavior of Steel-Plate Shear Walls Under Cyclic Loads", *Journal of Structural Engineering*, ASCE, Vol. 119, No. 2, Feb. 1993, pp. 588-605.

FEMA (1997), *FEMA 302 NEHRP Recommended Provisions for Seismic Regulations for New Buildings and Other Structures, Part-1-Provisions*, Building Seismic Safety Council for the Federal Emergency Management Agency, Washington, D.C.

FEMA (2001), *FEMA 369 NEHRP Recommended Provisions for Seismic Regulations for New Buildings and Other Structures, Part-1-Provisions*, Building Seismic Safety Council for the Federal Emergency Management Agency, Washington, D.C.

FEMA (2001), *FEMA 369 NEHRP Recommended Provisions for Seismic Regulations for New Buildings and Other Structures, Part-2-Commentary*, Building Seismic Safety Council for the Federal Emergency Management Agency, Washington, D.C.

Goto, Y., Suzuki, S., and Chen, W.F., (1991), "Analysis of Critical Behavior of Semi-Rigid Frames With or Without Load Histories in Connections", *International Journal of Solids and Structures*, Vol. 27, No. 4, pp 467-483.

Kennedy, D.J.L., Kulak, G.L., and Driver, R.G. (1994), Discussion of "Postbuckling Behavior of Steel-Plate Shear Walls Under Cyclic Loads" by Elgaaly, M., Caccese, V., and Du, C., *Journal of Structural Engineering*, ASCE, Vol. 120, No. 7, pp. 2250-2251.

Kuhn, P., Peterson, J.P. and Levin, L.R. (1952), *A Summary of Diagonal Tension, Part 1 - Methods of Analysis*, Technical Note 2661, National Advisory Committee for Aeronautics, Langley Aeronautical Laboratory, Langley Field, Va.

Kulak, G.L., Kennedy, D.J.L., and Driver, R.G., (1994), Discussion of "Experimental Study of Thin Steel-Plate Shear Walls Under Cyclic Loads" by Elgaaly, M., Caccese, V., and Du, C., *Journal of Structural Engineering*, ASCE, Vol. 120, No. 10, pp. 3072-3073.

Lubell, A.S., Prion, H.G.L., Ventura, C.E., and Rezai, M. (2000), "Unstiffened Steel Plate Shear Wall Performance Under Cyclic Loading", *Journal of Structural Engineering*, ASCE, Vol. 126, No.4, April 2000, pp. 453-460.

MathWorks (1999), "MatLab Function Reference", The MathWorks, Inc., Natick, MA.

Mimura, H., and Akiyama, H. (1977), "Load-Deflection Relationship of Earthquake-Resistant Steel Shear Walls with a Developed Diagonal Tension Field", *Transactions of the Architectural Institute of Japan*, Vol. 260, October, pp. 109-114. (In Japanese)

Mo, Y.L., and Perng, S.F. (2000), "Seismic Performance of Framed Shearwalls Made of Corrugated Steel", Proceedings of the Sixth ASCCS International Conference on Steel-Concrete Composite Structures, Los Angeles, Ca, March 22-24, 2000, pp.1057-1064.

Rezia, M., (1999), "Seismic Behavior of Steel Plate Shear Walls by Shake Table Testing", Ph.D. Dissertation, University of British Columbia, Vancouver, British Columbia, Canada.

Schumacher, A., Grondin, G.Y., and Kulak, G.L., "Connection of Infill Panels in Steel Plate Shear Walls", *Canadian Journal of Civil Engineering*, Vol. 26, No. 5, pp. 549-563.

Thorburn, L.J., Kulak, G.L., and Montgomery, C.J. (1983), "Analysis of Steel Plate Shear Walls", Structural Engineering Report No. 107, Department of Civil Engineering, Universtiy of Alberta, Edmonton, Alberta, Canada.

Timler, P.A. and Kulak, G.L. (1983), "Experimental Study of Steel Plate Shear Walls", Structural Engineering Report No. 114, Department of Civil Engineering, University of Alberta, Edmonton, Alberta, Canada.

Timler, P.A. (1998), "Design Procedures Development, Analytical Verification, and Cost Evaluation of Steel Plate Shear Wall Structures", Earthquake Engineering. Research Facility Technical Report No. 98-01, Department of Civil Engineering, University of British Columbia, Vancouver, British Columbia, Canada.

Tromposch, E.W., and Kulak, G.L. (1987), "Cyclic and Static Behaviour of Thin Panel Steel Plate Shear Walls", Structural Engineering Report No. 145, Department of Civil Engineering, University of Alberta, Edmonton, Alberta, Canada

Wagner, H., (1931), "Flat Sheet Metal Girders with Very Thin Metal Webs. Part I-General Theories and Assumptions", National Advisory Committee for Aeronautics, Technical Memo., No. 604.

Xue, M., and Lu, L.-W. (1994), "Interaction of Infilled Steel Shear Wall Planels With Surrounding Frame Members", Proceedings of the Structural Stability Research Council Annual Technical Session, Bethlehem, Pa, pp. 339-354

Yang, T.Y., and Whittiker, A. (2002), "MCEER Demonstration Hospitals - Mathematical Models and Preliminary Results", Technical Report, Multidisciplinary Center for Earthquake Engineering Research, University at Buffalo, Buffalo, NY.

APPENDIX A

PREDICTION OF PUSHOVER CURVES

A.1 General

This appendix explains how the predicted monotonic pushover curves presented in Section 5 and compared against the experimental results in Section 6 were obtained.

A.2 SAP2000 Strip Models

An example of the SAP2000 strip models used in the prediction of ultimate strength is shown in figure A-1. Strip properties including yield stress (F_y), width (w), and thickness (t) used in the models for each specimen are given in table A-1. All strips had simple connections at each end and were assigned elastic-plastic axial plastic hinge properties with 1.0% strain hardening (based on the results of coupon tests reported in Section 4). The beam and column elements were modeled using standard, elastic beam elements and were assigned section properties equal to that of W18x86 beams and W12x96 columns. Simple beam-to-column connections were used in the SAP2000 models and the contribution of the actual semi-rigid beam-to-column connections of the specimens were incorporated using the results of bare frame testing as described in Section A.4. Displacement controlled pushover analyses were carried out for each model to 25 mm displacement at the control node identified in figure A-1. The resulting yield base shear was verified by checking it against that calculated using (4-1) for specimen C1 and (3-7) for specimen F2.

TABLE A-1 Strip Properties Used in SAP2000 Pushover Analyses

Specimen	Fy (MPa)	w (mm)	t (mm)
C1	325	256	0.71
F2	221	193	0.91

151
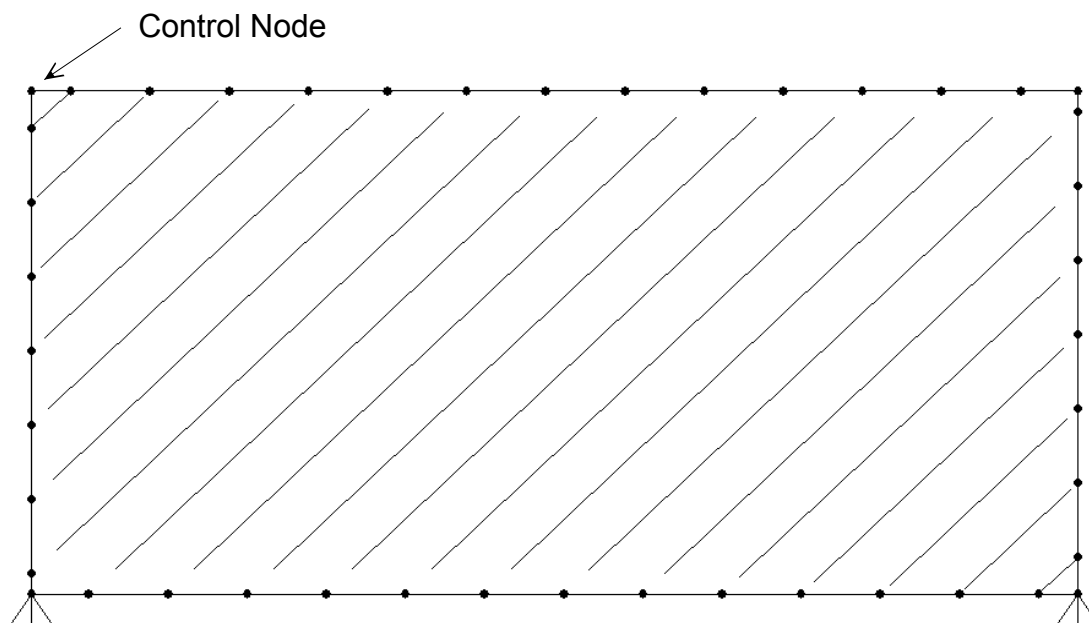
FIGURE A-1 Strip Model Used for Pushover Analysis in Sap2000

A.3 Strip Length Correction

In this case, due to the scale of the specimens and depth of the boundary frame members, the yield displacements from the SAP2000 pushover analyses were less then expected. Therefore, displacements less than or equal to the yield displacement were multiplied by the ratio of actual strip length in the constructed specimen to the strip length modeled in SAP2000. The difference between the SAP2000 yield displacement and the SAP2000 yield displacement multiplied by the strip length ratio was subtracted from all displacements greater than yield.

A.4 Bare Frame Superposition

In order to incorporate the contribution of the bare frame (recall the SAP2000 model used simple beam-to-column connections) into the prediction of the specimens behavior the results of bare frame testing of BF1 were used. However, the displacements recorded in the bare frame testing of BF1 were not the same values as those resulting from the SAP2000 analyses. Therefore, a simple linear interpolation routine was written in MatLab to find the boundary frame base shear (from the test data of BF1) at the displacements from the adjusted pushover analyses. These base shears were then simply added to the base shears from the adjusted pushover analyses. Figures A-2 and A-3 show the unadjusted SAP2000 pushover curves, the adjusted SAP2000

152

pushover curves, the final pushover curves after addition of the boundary frame data, and the results of (4-1) and (3-7), for specimens C1 and F2 respectively.
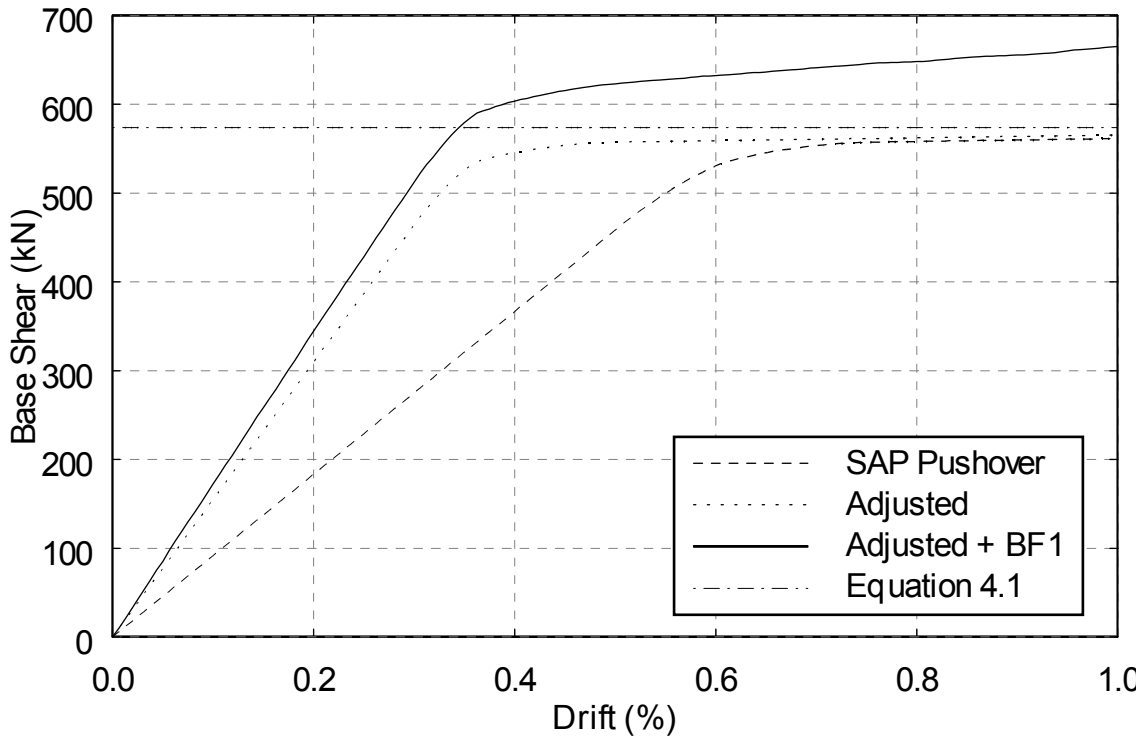
FIGURE A-2 Predicted Pushover Curves for Specimen C1
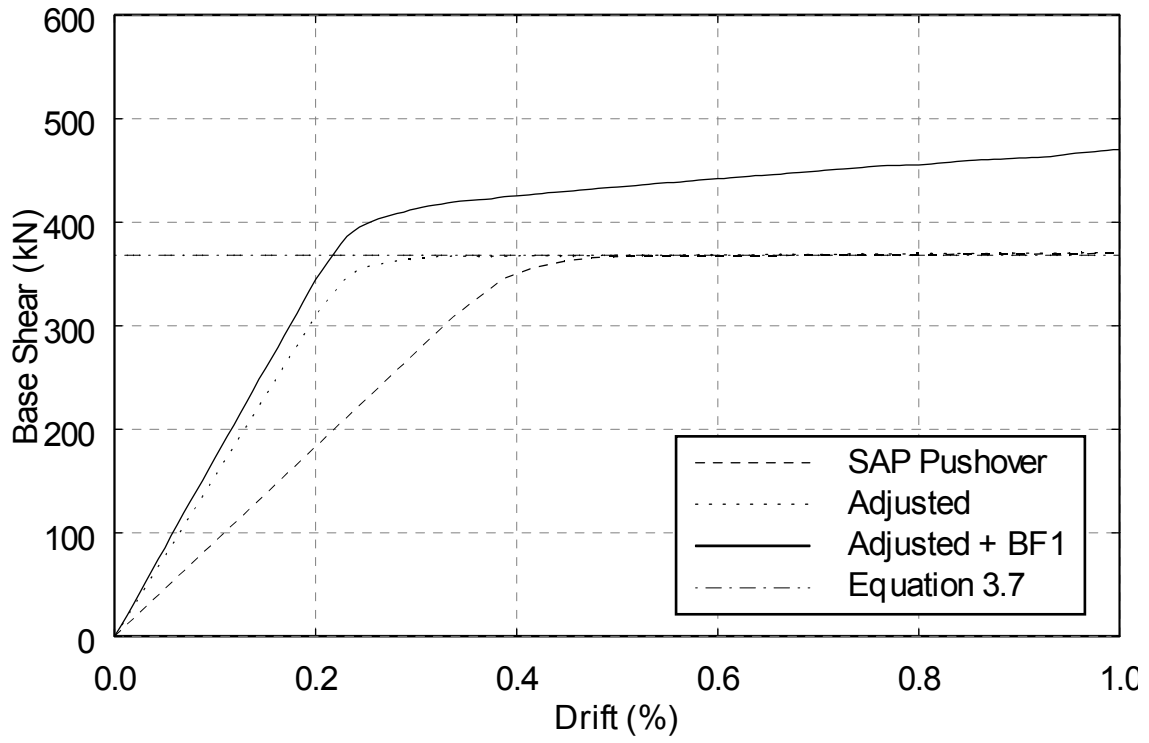
FIGURE A-3 Predicted Pushover Curves for Specimen F2

APPENDIX B

BOUNDING SURFACE MODEL APPLICATION

Shown in this appendix is the function written in MatLab to employ the bounding surface model with internal variables (Defalias and Popov, 1976) described in Section 6. MatLab is an object orientated programming language in which functions can be written to perform certain tasks and then be called inside a routine which was written to preform a larger task. The routine passes data to the function, which processes it, and then returns output data to the routine. This particular function, named defalpopovBF2, is passed the vectors DRel, Dmax, and loc, which are the relative displacements recorded during testing of the specimen, the maximum displacements of the specimen at each cycle (both positive and negative), and the locations of the maximum displacements within the relative displacement vector. It returns FDP1, which is a vector of the modeled boundary frame forces for each relative displacement in DRel. The parameters needed for the application of the bounding surface model were shown in table 6-1 are defined at the top of the function. A different function was used for each boundary frame, although the only difference between them was the model parameters of table 6-1. What follows is the function for the modeling of BF2.

```matlab
function[FDP1]=defalpopovBF2(DRel,Dmax,loc)
%%Defalias-Popov Bounding Surface Model With Internal Variables%%
%%Bound Line%%
Dinc=[-80:.01:80]';
Rbpos=75;
Rbneg=-75;
Rbslope=3.0;
RbnegLine=Rbneg+(Rbslope*Dinc);
RbposLine=Rbpos+(Rbslope*Dinc);
h=25;
Rki=6.9;
Rkii=6.9;
Dyield=13.5;
a=.666;
b=.418;;
%%Loop Cycles%%
numpeaks=size(Dmax);
numpeaks=numpeaks(1);
FDP1=zeros(size(DRel));

for k=1:numpeaks-1
    if k>1&abs(Dmax(k-1))>Dyield
        Rki=Rkii*(a*(abs(Dmax(k))/Dyield)+b);
        if Rki>(2.5*Rkii)
            Rki=2.5*Rkii;
        else
        end

    else
    end
    if Dmax(k+1)<0|k+1==numpeaks
        r=find(Dinc<=(Dmax(k)+.005)&Dinc>=(Dmax(k)-.005));
        delin=RbnegLine(r)-FDP1(loc(k));
        for i=loc(k):loc(k+1)
            p=find(Dinc<=(DRel(i)+.005)&Dinc>=(DRel(i)-.005));
            if i==1
                del=RbnegLine(p)-0;
                Rkp=Rbslope+(h*(del/(delin-del)));
                Rkt=Rki*Rkp/(Rki+Rkp);
                FDP1(i)=0+(Rkt*(DRel(i)-0));
            else
```

156

```
            del=RbnegLine(p)-FDP1(i-1);
            Rkp=Rbslope+(h*(del/(delin-del)));
            Rkt=Rki*Rkp/(Rki+Rkp);
            FDP1(i)=FDP1(i-1)+(Rkt*(DRel(i)-DRel(i-1)));
        end
    end
else
    r=find(Dinc<=(Dmax(k)+.005)&Dinc>=(Dmax(k)-.005));
    delin=RbposLine(r)-FDP1(loc(k));
    for i=loc(k):loc(k+1)
        p=find(Dinc<=(DRel(i)+.005)&Dinc>=(DRel(i)-.005));
        if i==1
            del=RbposLine(p)-0;
            Rkp=Rbslope+(h*(del/(delin-del)));
            Rkt=Rki*Rkp/(Rki+Rkp);
            FDP1(i)=0+(Rkt*(DRel(i)-0));
        else
            del=RbposLine(p)-FDP1(i-1);
            Rkp=Rbslope+(h*(del/(delin-del)));
            Rkt=Rki*Rkp/(Rki+Rkp);
            FDP1(i)=FDP1(i-1)+(Rkt*(DRel(i)-DRel(i-1)));
        end
    end
end
end
return
```

APPENDIX C

ADDITIONAL STRAIN GAUGE DATA

This appendix contains plots of the strain gauge data for the gauges mounted on the East faces of specimens C1 and F2. Figures 4-30 and 4-32 show the locations of the gauges for specimens F2 and C1 respectively. The data is presented in the same manner as the data for the gauges on the west side of the infills, which was shown in Section 6.
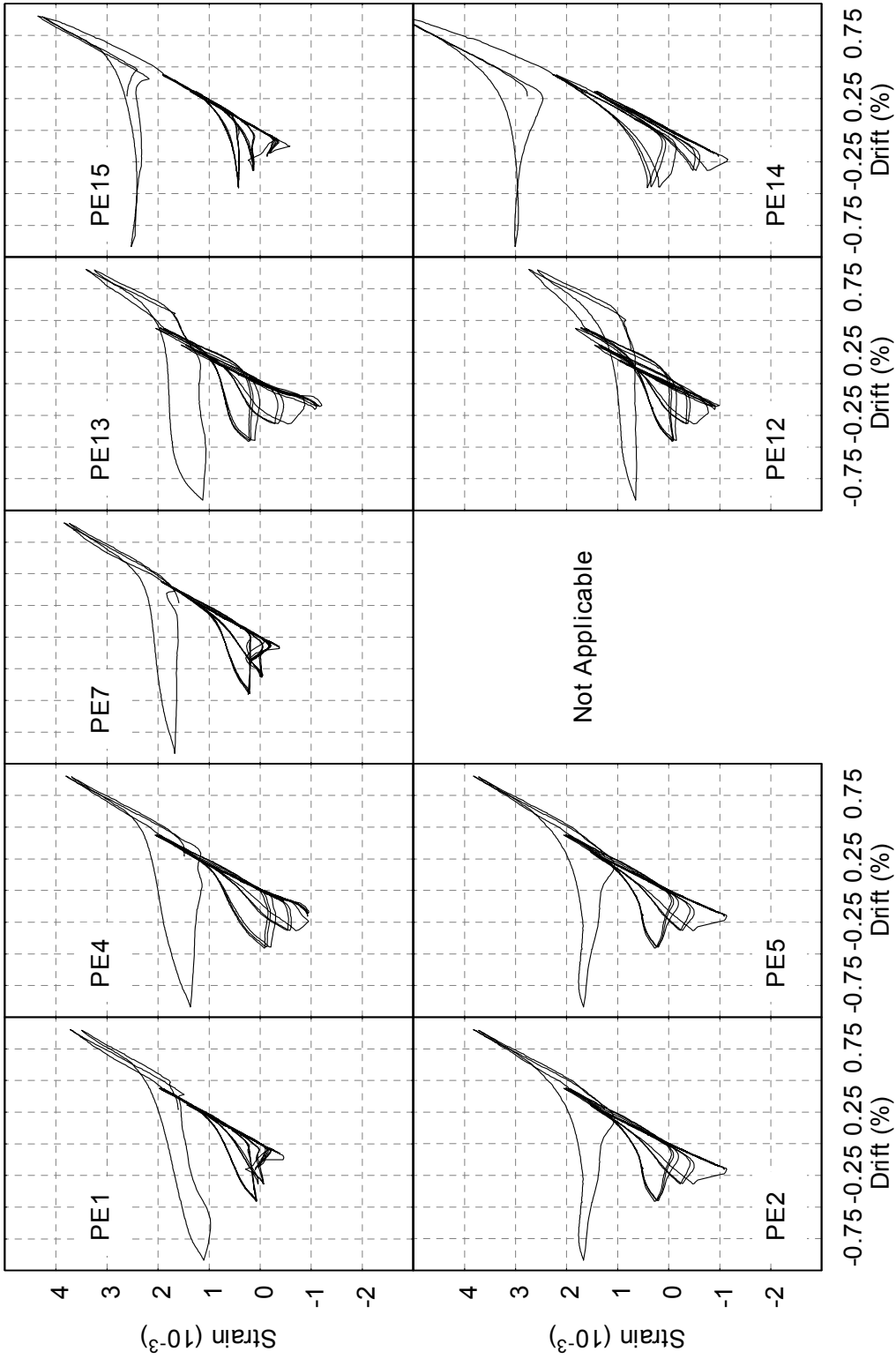
FIGURE C-1 Variation of Strain Across Infill - Specimen C1 - Data Truncated at Cycle 14 ($2\delta_y$) - East Face

FIGURE C-2 Base Shear Versus Strain Across Infill - Specimen C1 - Data Truncated at Cycle 14 ($2\delta_y$) - East Face

161

FIGURE C-3 Variation of Strain Across Infill - Specimen F2 - Data Truncated at Cycle 12 (2δ_y) - East Face

FIGURE C-4 Base Shear Versus Strain Across Infill - Specimen F2 - Data Truncated at Cycle 12 ($2\delta_y$) - East Face

163